SPH Simulation of Fluid-Structure Interaction Problems with Application to Hovercraft

Qing Yang

Dissertation submitted to the Faculty of the
Virginia Polytechnic Institute and State University
in partial fulfillment of the requirements for the degree of

Doctor of Philosophy
in
Aerospace Engineering

Leigh McCue, Chair
Mayuresh Patil
Christopher Roy
Danesh Tafti

December 6, 2011
Blacksburg, Virginia

Keywords: Fluid-Structure Interaction (FSI), Smoothed Particle Hydrodynamics (SPH), Finite Element Method (FEM), Hovercraft, Air Cushion Vehicle (ACV), Surface Effect Ship (SES)

SPH Simulation of Fluid-Structure Interaction Problems with Application to Hovercraft

Qing Yang

(ABSTRACT)

A Computational Fluid Dynamics (CFD) tool is developed in this thesis to solve complex fluid-structure interaction (FSI) problems. The fluid domain is based on Smoothed Particle Hydrodynamics (SPH) and the structural domain employs large-deformation Finite Element Method (FEM). Validation tests of SPH and FEM are first performed individually. A loosely-coupled SPH-FEM model is then proposed for solving FSI problems. Validation results of two benchmark FSI problems are illustrated (Antoci et al., 2007; Souto-Iglesias et al., 2008). The first test case is flow in a sloshing tank interacting with an elastic body and the second one is dam-break flow through an elastic gate. The results obtained with the SPH-FEM model show good agreement with published results and suggest that the SPH-FEM model is a viable and effective numerical tool for FSI problems.

This research is then applied to simulate a two-dimensional free-stream flow interacting with a deformable, pressurized surface, such as an ACV/SES bow seal. The dynamics of deformable surfaces such as the skirt/seal systems of the ACV/SES utilize the large-deformation FEM model. The fluid part including the air inside the chamber and water are simulated by SPH. A validation case is performed to investigate the application of SPH-FEM model in ACV/SES via comparison with experimental data (Zalek and Doctors, 2010).

The thesis provides the theory of the SPH and FEM models incorporated and the derivation of the loosely-coupled SPH-FEM model. The validation results have suggested that this SPH-FEM model can be readily applied to skirt/seal dynamics of ACV/SES interacting with free-surface flow.

Dedication

This thesis is dedicated to my parents.

Acknowledgments

First I'd like to thank my advisor, Dr. Leigh McCue, for her sincere and patient guidance and help during my PhD study. This thesis can not be done without her support and courage. She's a great advisor and friend. I believe it is a life-beneficial experience working under her leadership.

I also feel lucky to have three other outstanding professors on my committee. I gained a lot of knowledge from the two advanced CFD courses instructed by Dr. Roy and Dr. Tafti and talking with them can always enlighten me on my research. My understanding on structural dynamics is always strengthened after each meeting with Dr. Patil.

I am grateful to my host family, Amy and John Ogburn. They are very nice to me and I learned a lot about U.S. culture from them.

I'm thankful to my friends met in Blacksburg, especially Yue Yan, Wan Wu, Zhiye Zhang, Min Li, Shaobin Liu, Yu Lei, Haiyang Fu, Ouliang Chang and others. My life in Blacksburg can not be wonderful without you.

It's great honor and pleasure to work with other students of Dr. McCue, Wan Wu, Michele Cooper, Van Jones, Zhiliang Xing, Pankaj Kumar and Rob Cole.

I appreciate all the help from Rachel Hall Smith, Steve Edwards and Christine Durner in AOE department.

I would also express my gratitude to Dr. Pat Purtell and Kelly Cooper at the Office of Naval Research for their sponsorship of this research under grant numbers N000140710833, N000140810695,

N000141010398. Additional thanks to Dr. Paul Groenenboom at ESI Group Netherlands for pointing out the importance of non-linear constitutive relation, Dr. Stefano Sibilla at University of Pavia for providing Antocis thesis (Antoci, 2006), Dr. Souto-Iglesias at Technical University of Madrid for the details of the experimental data for the validation of the sloshing tank case, Dr. Zalek. at University of Michigan for providing the experimental data for the validation case of the surface effect ship.

Finally, I'd like to thank my friends distributed all over the world, my parents and other family members who cheered and supported me all along the way.

Contents

List of Figures

List of Tables

Chapter 1

Introduction

1.1 Computational Methods

The ever-increasing computer technology and the development of numerical methods have enabled numerical modeling and simulation of the real physical world once deemed impossible. Both the complexity of the model and the demand for accuracy of the numerical model has pushed forward the front line of research on numerical methods.

1.1.1 Why Choose a Lagrangian Perspective?

The first way to categorize a numerical method is based on the perspective for modeling the dynamics of the object (Liu and Liu, 2003, 2010). The equations in a CFD analysis can be in either Lagrangian, Eulerian, or combined Lagrangian-Eulerian perspective. A Lagrangian perspective means the variables of a moving object are measured in the perspective of the moving object, while in the Eulerian perspective the variables of a moving object are measured in the perspective of a static object. The Lagrangian perspective is popular in Finite Element Methods (FEM) dealing with structural dynamics and the Eulerian perspective is often used in computational fluid

dynamics. When describing the motion in a Lagrangian perspective, the substantial derivative is used without need to calculate the convective terms as in Euler description. Using the Lagrangian perspective allows for ease in tracking the time history of material positions and interfaces. But tracking the deformable boundaries and moving material interfaces are relatively more difficult in an Eulerian framework (Liu and Liu, 2003, 2010). Lagrangian methods are often more computationally efficient due to the natural bounding of the domain (Liu and Liu, 2003, 2010). However, Lagrangian methods suffer difficulties when mesh distortion is present. For meshed methods, additional computation is given to rezone the mesh or re-mesh the problem domain. Combined Lagrangian-Eulerian methods were invented to draw the merits from both perspectives by describing the variables in an intermediate coordinate system. The Arbitrary-Lagrangian-Eulerian method is well-developed numerical techniques which have been successfully applied into many fluid-structure interaction problems. Since large-deformation is expected in the analysis of the dynamics of the Air Cushion Vehicle (ACV), a Lagrangian-perspective method is therefore preferred.

1.1.2 Why Choose a Meshless Method?

Based on the elements used, the numerical methods can also be divided into mesh/grid/cell methods and meshless/meshfree/particle methods (hereinafter called meshless method). The meshed methods have dominated the numerical world for decades while the meshless methods have drawn increasing interest and attention in recent years. The history and an introduction to different meshless methods can be found in Liu and Liu (2003). The meshless methods usually do not have the mesh distortion or mesh entanglement problems of traditional meshed methods. Along the same lines, they typically require no special treatment of fluid interfaces. This reduced complexity is especially useful when applied to simulations involving large free surface deformations, for example no additional computation is needed for wave overtuning for a non-linear wave or fluid interactions with highly deformable structures as the wave impact on the skirt systems of the ACV.

1.1.3 Why Choose SPH?

As a fully Lagrangian meshless method, Smoothed Particle Hydrodynamics (SPH) has been successfully applied to various free-surface problems such as dam-break flow (Colagrossi and Landrini, 2003), breaking waves on a beach (Monaghan and Kos, 1999), wedge drop (Oger et al., 2006), flow in sloshing tank (Delorme et al., 2009; Souto-Iglesias et al., 2006), and complicated geometry such as high speed ship flow (Le Touz et al., 2008), etc. It is therefore used in this thesis as the tool for the numerical analysis of fluid dynamics. SPH has also been used to solve elastic body dynamics as demonstrated by the work by Libersky et al. (1993) and Gray et al. (2001). However, there are drawbacks inherent to SPH such as an artificial stress term required to avoid tensile instability. Additionally, boundary deficiency artifacts remain problematic where particle field variables near the boundaries lose consistency resulting from the lack of influence of the neighboring particles in a support domain truncated by the boundaries. Antoci et al. (2007) extended the use of SPH into problems involving free-surface flows interacting with a deformable structure. They solved the FSI problem with a SPH-SPH model which simulates both fluid and structural domains in SPH.

1.1.4 Why Choose a Lagrangian FEM over ALE FEM

A well-developed numerical approach for fluid interactions with deformable structures is the Arbitrary Lagrangian-Eulerian (ALE) description of the Finite Element Method. It has proven its ability to deal with large deformation multi-physical interaction problems including metal forming, explosions, etc. (Donea et al., 2004; Hirt et al., 1997; Hughes et al., 1981). ALE can address the disadvantages associated with meshed Lagrangian perspectives in that it does not require remeshing even after large mesh distortions. In addition, ALE does not suffer ambiguity in the definition of the interface associated with the Eulerian perspective (Donea et al., 2004). However, the ALE method requires more computation for mesh adaptation and regularization compared to meshless Lagrangian methods. To avoid the complexity associated with meshed Lagrangian methods for

violent flows which usually involve mesh entanglement, we chose SPH as the fluid model. In this thesis, the Finite Element Method (FEM) is used to simulate the structural domain due to its maturity as a numerical tool in the analysis of structural dynamics without additional modification of governing equations. Since the structures in the validation models involve large deformation but no mesh distortion or entanglement, the structural dynamics are described in a Lagrangian perspective FEM instead of the more computationally-expensive ALE. If future work requires simulations of structures with large distortions, then the structural model can be extended to use an ALE description.

1.1.5 Why Couple SPH and FEM?

Because of the accuracy of FEM in solving structural dynamics and the convenience of SPH in simulating free-surface fluid dynamics, a SPH-FEM model is chosen to investigate the FSI problem. The coupled SPH-FEM model was first proposed by Attaway et al. (1994) to investigate a structure-structure impact model. The SPH-FEM model has been applied to fluid-structure impact problems in the work by Vuyst et al. (2005), and free-surface flow interaction with elastic structures in the work by Groenenboom and Cartwright (2010) and Fourey et al. (2010, 2011). Their work lends validity to pursuing this line of SPH-FEM-based analysis. The most obvious difference between these models and that proposed here lies in the modeling of the contact force at the fluid-structure interface. Attaway et al. (1994) and Groenenboom and Cartwright (2010) calculated the contact force based upon an iterative master-slave scheme which is to find the best penalty force to prevent interface penetration and satisfy conservation of momentum. Fourey et al. (2010, 2011) use the dummy particles scheme to compute the pressure from the fluid side in both 2D and 3D cases. Vuyst et al. (2005) introduce a contact potential to treat the contact force as a particle-to-particle force. In this work, we utilize a Monaghan boundary condition (Monaghan, 2005; Monaghan and Kos, 1999), which is the most general boundary condition in conventional SPH for contact forces. This force transmission mechanism is convenient to implement and less computationally expensive

than either the master-slave scheme or the dummy particles. The validation results indicate that the Monaghan boundary condition can accurately determine displacements.

1.1.6 Why Select FEM Rather than SPH for the Structural Model

As mentioned above, SPH is also capable of handling structural dynamics. The work of Antoci et al. (2007) shows encouraging results, but also demonstrates a need for improvement in the simulation of elastic body dynamics by SPH. As discussed later, SPH uses an equation of state to relate pressure and density. As a result, the time step must be inversely proportion to the bulk modulus to maintain computational stability. Because the compressibility of the fluid is typically much greater than that of the structure, the time step requirement is dominated by the structural CFL condition. The resultant low CFL number for the fluid is computationally inefficient. Therefore FEM model is preferred in this analysis for structural model and the CFD tool used in this analysis is a fully Lagrangian SPH-FEM model (Yang et al., 2010, 2011a,b). The fluid domain is based on Smoothed Particle Hydrodynamics and the structural domain employs large-deformation Finite Element Method.

1.2 Research Purpose

The purpose of this research is to find a non-linear CFD solver to quantitatively assess design modifications and complement model tests of air cushion vehicles (ACVs). The principle of ACVs is to keep pressurized air under the craft which lifts the main hull and reduces the wet surface to reduce surface interference and drag (Mantle, 1975; Yun and Bliault, 2000). Past developments have shown a flexible skirt system, which is composed of pressurized bags with fingers first proposed in 1958 by C. H. Latimer Needham, to be a viable design to achieve better performance for an ACV (Mantle, 1975; Yun and Bliault, 2000). This gives an ACV a large obstacle clearance and enables real amphibious capability. ACVs have drawn increasing attention to conduct work

in extremely reduced depth environments. During an amphibious transit, it is not unlikely for an ACV to encounter a nonlinear breaking wave in the surf zone. The impact of the wave may result in cushion pressure spikes, excessive skirt material stresses and severe craft deceleration if bow plow-in occurs. Non-linear, plunging breakers can exceed typical craft skirt heights causing ventilation problems. In the scenario of embarkation into the sea, large breaking waves can hinder a craft's ability to make headway (Mantle, 1975; Yun and Bliault, 2000). All the above-mentioned effects need to be included and analyzed in the design phase of the ACV. However, many design parameters are traditionally decided by empirical formulas due to this highly non-linear fluid-structure interaction.

Doctors (1975) coupled a linearized hydrodynamic model based on a wave Green function, a compressible fluid model for the air cushion, and a flow model for the air supply system to simulate the motions of an ACV in waves. The vehicle and air cushion dynamics were coupled to the free surface via a pressure term added to the free surface boundary condition in the region beneath the air cushion. Sullivan et al. (1994) developed coupled simulation models to understand the dynamics of the bag-and-finger skirt system using a Lagrangian technique to derive the 2D equations of motion of the skirt and vehicle. Commercial software like AEGIR and ACVSIM (Milewski et al., 2007, 2008) use potential flow theory or a linear solver to couple with an air cushion model. Thiagarajan and Morris-Thomas (2006) investigated the heave and pitch response of a closed bottom box and an air-cushioned open bottom box based on linear wave theory. Promising results were obtained but a potential flow solver was not able to handle the overtuning wave. This sets the context for the development of the SPH-FEM based simulation tool.

A new non-linear fluid-structure interaction solver as a design tool for the ACV/SES under non-linear breaking waves is actively sought. Since the SPH-FEM model can simulate violent free-surface flow interacting with structural deformation in the time domain (Yang et al., 2010, 2011a,b), it is introduced to simulate a two-dimensional free-stream flow interacting with a deformable, pressurized surface such as an ACV/SES bow seal. The dynamics of deformable surfaces such as the skirt/seal systems of the ACV/SES utilize the large-deformation FEM model. The fluid part in-

cluding the air inside the chamber and water are simulated by SPH. This tool can then be used to study the deflection and internal stress of a skirt/seal system given a set of free-stream flow and cushion/seal parameters. Experimental validation data is available in Zalek and Doctors (2010). The validation results lend credence to the use of this 2D SPH-FEM tool, and emphasis toward future development of a 3D tool, for ACV/SES skirt/seal dynamics.

1.3 Content Outline

Chapter 2 presents the theory of Smoothed Particle Hydrodynamics. The basics of the SPH including SPH formulation of the Navier-Stokes Equations, boundary condition, stability condition and some applications utilizing SPH model (Liu and Liu, 2003, 2010; Monaghan, 1992, 2005) are discussed.

Chapter 3 provides the derivation of the Lagrangian large-deformation Finite Element Method (Bathe, 1996; Bathe et al., 1975; Zienkiewics and Taylor, 2005) for the structural analysis. The theory starts from the principle of virtual work and the weak form of the governing equation is then obtained. The non-linearity from both geometric deformation and constitutive relations are discussed. Some applications using this FEM model are also presented. Chapters 2 and 3 essentially summarize existing knowledge and provide verification and validation for the SPH-FEM model.

Chapter 4 shows two validation cases using a coupled SPH-FEM model solving free-surface flow interacting with deformable structures. The validation results show good agreement with the published experimental result in Antoci et al. (2007) and Souto-Iglesias et al. (2008)

Chapter 5 applies the SPH-FEM described in Chapter 4 to the seal/skirt systems of hovercraft. The numerical simulation to investigate the dynamics of the bow seal/skirt of a Surface Effect Ship (SES) is performed via comparison with Zalek and Doctors (2010). Chapters 4 and 5 are focused on novel new applications and development of the SPH-FEM model.

Chapter 6 summarizes the achievements of the current work and provides suggestions for future work.

Chapter 2

Smoothed Particle Hydrodynamics

2.1 Introduction

Smoothed Particle Hydrodynamics (SPH) is a meshless Lagrangian particle method first proposed in astrophysics (Gingold and Monaghan, 1977; Lucy, 1977) and later successfully applied to complex fluid problems. The basic concept of SPH is to discretize the flow into particles for which one can reproduce the physical field variables for enabling this integral representation. A smoothing function, known as the kernel function is the SPH convention. It is introduced to approximate the physical field variables as the summation of neighboring particles. The spatial derivative of field variables is related to the derivative of the kernel function. The following section discusses the basics of conventional SPH applied to free-surface problems as summarized in Monaghan's review paper (Monaghan, 1992, 1994, 2005) and corrections applied to gain the consistency of the SPH model.

2.2 SPH Approximation of a Function and Its Derivatives

SPH starts from the identity that (Liu and Liu, 2003; Monaghan, 1992, 2005):

$$f(\mathbf{x}) = \int_{\Omega} f(\mathbf{x}')\,\delta\left(\mathbf{x}-\mathbf{x}'\right)\,\mathrm{d}\mathbf{x}' \tag{2.1}$$

In which $\delta\left(\mathbf{x}-\mathbf{x}'\right)$ is the Dirac delta function:

$$\delta\left(\mathbf{x}-\mathbf{x}'\right) = \begin{cases} 0 & \mathbf{x} \neq \mathbf{x}' \\ \\ 1 & \mathbf{x} = \mathbf{x}' \end{cases} \tag{2.2}$$

Ω is the domain of integration. The Dirac delta function is only a point function and the basic idea of SPH is to replace the Dirac delta function with a smoothing function $W\left(\mathbf{x}-\mathbf{x}', h\right)$, or called kernel function in SPH convention, to have an area (2D) or a volume (3D) of integration domain (Liu and Liu, 2003; Monaghan, 1992, 2005). The size of the area or volume is related to h, the smoothed length. The function f is then approximated by the kernel function (Liu and Liu, 2003; Monaghan, 1992, 2005):

$$\langle f(\mathbf{x})\rangle = \int_{\Omega} f(\mathbf{x}')\,W\left(\mathbf{x}-\mathbf{x}', h\right)\,\mathrm{d}\mathbf{x}' \tag{2.3}$$

Angle brackets denote the variables approximated by the kernel function. W is the interpolating kernel. The approximation of the derivative of the function f is to replace f with $\nabla \cdot f(\mathbf{x})$ in Eq. (2.3) (Liu and Liu, 2003, 2010; Monaghan, 1992, 2005):

$$\langle \nabla \cdot f(\mathbf{x})\rangle = \int_{\Omega} \nabla \cdot f(\mathbf{x}')\,W\left(\mathbf{x}-\mathbf{x}', h\right)\,\mathrm{d}\mathbf{x}' \tag{2.4}$$

Considering $\nabla \cdot (ab) = \nabla a \cdot b + a \cdot \nabla b$ and the divergence theorem (Liu and Liu, 2003; Monaghan, 1992, 2005):

$$\langle \nabla \cdot f(\mathbf{x})\rangle = \int_{S} f(\mathbf{x}')W(\mathbf{x}-\mathbf{x}', h)\cdot \vec{n}\,dS - \int_{\Omega} f(\mathbf{x}')\cdot \nabla W(\mathbf{x}-\mathbf{x}', h)\,\mathrm{d}\mathbf{x}' \tag{2.5}$$

As will be given in Section 2.3, the kernel function W should be zero long the boundary of the integration domain so that Eq. (2.5) is further simplified as (Liu and Liu, 2003; Monaghan, 1992, 2005):

$$\langle \nabla \cdot f(\mathbf{x}) \rangle = -\int_{\Omega} f(\mathbf{x}') \cdot \nabla W(\mathbf{x} - \mathbf{x}', h)\, \mathrm{d}\mathbf{x}' \tag{2.6}$$

For numerical calculation, the integral interpolant is approximated by a summation interpolant (Monaghan, 1992). As a particle method, SPH discretizes the computational domain into number of particles. Each particle has a lumped area (2D) or volume (3D) and can be represented as m_a/ρ_a. Then according to Eq. (2.3), the particle approximation for a field variable becomes (Liu and Liu, 2003, 2010; Monaghan, 1992, 2005):

$$\langle f(\mathbf{x}) \rangle = \sum_{b=1}^{N} \frac{m_b}{\rho_b} f(\mathbf{x}_b)\, W(\mathbf{x} - \mathbf{x}_b, h) \tag{2.7}$$

In which b is the particles within a particle's smoothed area determined by the smoothed length h. N is the total number of its neighboring particles. The derivative of a function as in Eq. (2.6) becomes (Liu and Liu, 2003, 2010; Monaghan, 1992, 2005):

$$\langle \nabla \cdot f(\mathbf{x}) \rangle = -\sum_{b=1}^{N} \frac{m_b}{\rho_b} f(\mathbf{x}_b) \cdot W(\mathbf{x} - \mathbf{x}_b, h) \tag{2.8}$$

2.3 Kernel Function

As the essential part of SPH formulation, the kernel function can determine the accuracy and stability of the numerical results. In Liu and Liu (2003, 2010), the efforts by different researchers to improve the performance of SPH kernel function were summarized. Different kernel functions have been proposed such as a bell-shaped function, Gaussian kernel function, B-spline function, quintic spline function, quadratic smoothing function, etc. (Liu and Liu, 2003, 2010). Despite their differences in forms, there are several common features that all kernel functions must satisfy discussed below including symmetric, normalization (unity), monotonic, and compact support (Liu

and Liu, 2003). The quintic Wendland kernel (Wendland, 1995) was chosen as the SPH kernel function W_{ab}. Morris et al. (1997) and Monaghan and Kajtar (2009) demonstrate the superior performance and stability of the Wendland kernel function relative to the commonly used cubic spline kernel. The quintic Wendland kernel is given as:

$$W = C\,(1 + 2\,R)(1 - \frac{1}{2}\,R)^4 \tag{2.9}$$

In which R is the normalized distance between particles $R = r/h$. The coefficient C is calculated under the unity condition for 1D, 2D and 3D cases:

$$\int_\Omega W\,(\mathbf{x} - \mathbf{x}', h)\;\mathrm{d}\mathbf{x}' = 1 \tag{2.10}$$

2.4 Conservation of Mass

For the applications of SPH into incompressible flow (such as water), Incompressible SPH (ISPH) (Cummins and Rudman, 1999; Lee et al., 2008) has been proposed to update pressure by solving a Poisson's equation and the fluid is strictly incompressible. A more common approach and an alternative to save computation time for SPH is the Weakly Compressible SPH (WCSPH) (Monaghan, 1994, 2005). The incompressible flow is idealized as compressible flow by introducing artificial compressibility. The density variation of water is limited within 1%. This is usually achieved by relating the pressure to the density in terms of an equation of state as discussed in Section 2.6. The continuity equation in the SPH formulation can be written in two forms (Liu and Liu, 2003, 2010; Monaghan, 1992, 2005):

$$\rho_a = \sum_b m_b W_{ab} \tag{2.11}$$

or by:

$$\frac{\mathrm{d}\rho_a}{\mathrm{d}t} = \rho_a \sum_b \frac{m_b}{\rho_b}\, v_{ab} \cdot \nabla_a W_{ab} \tag{2.12}$$

As a meshless method, the field variables of an element are lumped on the particle. Subscripts a and b denotes the particle of interest and its neighboring particles. W_{ab} is the kernel function. Eq. (2.12) is preferred because it exhibits less boundary deficiency error than Eq. (2.11). In this work, the weakly compressible formulation is used.

2.5 Conservation of Momentum

$$\frac{\mathrm{d}v_a}{\mathrm{d}t} = -\sum_b m_b \left(\frac{P_a}{\rho_a^2} + \frac{P_b}{\rho_b^2} + \Pi_{ab} \right) \nabla_a W_{ab} \tag{2.13}$$

$$\frac{\mathrm{d}v_a}{\mathrm{d}t} = -\sum_b m_b \left(\frac{P_a + P_b}{\rho_a \rho_b} + \Pi_{ab} \right) \nabla_a W_{ab} \tag{2.14}$$

The SPH momentum equation is shown in Eq. (2.13) (for non-multiphase flow) and Eq. (2.14) (for multiphase flow) with Π_{ab} representing the viscosity term. Recent study (Shao et al., 2012) has shown a RANS turbulence model embedded into SPH formulation. Fluid-Structure Interaction is the main focus of this thesis and the effects of turbulence model will be investigated in the near future work. Monaghan's artificial viscosity model has been applied to astrophysics and gas dynamics problems (Monaghan, 2005). However, for water simulations, physical viscosity models such as Morris et al. (1997) and Cleary (1998) are preferred. In this thesis, Cleary's viscosity model is chosen because it preserves angular momentum assuming smoothing length h remains constant.

$$\Pi_{ab} = -\frac{\xi}{\rho_a \rho_b} \frac{4\mu_a \mu_b}{(\mu_a + \mu_b)} \frac{v_{ab} r_{ab}}{r_{ab}^2} \tag{2.15}$$

In Eq. (2.15), μ is the dynamic viscosity of the fluid. Numerical calibration yields $\xi = 4.9633$ (Cleary, 1998). To validate the viscosity models used in these tests, a Couette flow is simulated using Cleary's viscosity model and shown in Section 2.11.1.

2.6 Equation of State

In addition to SPH methods, there are other grid-based methods using equation of state for steady incompressible flow (Morris et al., 1997). The density variation of water is limited within 1%. This is usually achieved by relating the pressure to the density in terms of an equation of state. The isentropic equation of state per Batchelor (1967) is used and expressed as:

$$\frac{P+B}{I+B} = \left(\frac{\rho}{\rho_0}\right)^n \tag{2.16}$$

$$P = -B + \left(\frac{\rho}{\rho_0}\right)^n + B\left(\frac{\rho}{\rho_0}\right)^n \tag{2.17}$$

Since in most cases, $B \gg 1$, the term $\left(\frac{\rho}{\rho_0}\right)^n$ is omitted and the Tait equation of state per Batchelor (1967) is expressed in Eq. (2.18):

$$P = B\left[\left(\frac{\rho}{\rho_0}\right)^\gamma - 1\right] \tag{2.18}$$

where B is a reference pressure and ρ_0 is a reference density. Cole (1948) suggested $B = 3.047$ kilobars and $\gamma = 7.15$ for water based on experimental data. Choosing a larger value of B could reduce the density variation, better approximating the near incompressibility of water. However, in practice the value of B is limited by stability criteria resulting from the explicit numerical integration scheme. This is due to the inverse proportionality of the time step to the speed of sound. In Section 2.7,the derivation of value B is detailed.

For the simulation of multi-phase air-water flows, such as the air bubble rise in Section 2.11.3 and the air cushion vehicle in Chapter 5, the ideal gas law is applied and adiabatic process is assumed. The density and pressure is related by:

$$P = \rho RT \tag{2.19}$$

In which P is the absolute pressure, R is the individual gas constant, for air $R = 286.9(J/kgK)$, T is the Kelvin temperature. The gauge pressure of each individual particle is obtained by subtracting

atmosphere pressure from the absolute pressure.

2.7 Numerical Speed of Sound

From thermodynamics we know that the density variation is proportional to the Mach number (Monaghan, 2005):

$$\frac{|\delta\rho|}{\rho} \sim \frac{v^2}{c^2} = \mathrm{M} \tag{2.20}$$

c is the speed of sound of the fluid and given as:

$$c^2 = \frac{\partial P}{\partial \rho} \tag{2.21}$$

An equation of state is used to relate pressure with density as in Eq. (2.18) and Eq. (2.21) can be further expressed as:

$$c^2 = \frac{B\,\gamma\rho^{\gamma-1}}{\rho_0^{\gamma}} \tag{2.22}$$

As discussed in the previous section, use of the true speed of sound for water, which results in a large B, imposes an excessively strict limit on time step. Therefore a numerical speed of sound C_n instead of the true speed of sound is introduced to allow a reasonable time step while limiting the density variation within 1%. From Eq. (2.20) we get the numerical Mach number using numerical speed of sound should be less than 0.1. The common approach in the SPH community is first to find the maximum velocity $V_{\max}$ of the simulation case. For a free surface flow like the dam-break case in Section 4.4, $V_{\max}$ is approximated by $V_{\max} = \sqrt{2gH}$ and for free stream flow, $V_{\max}$ is taken as free-stream flow velocity. The numerical speed of sound is chosen as $C_{n0} = 10V_{\max}$. From Eq. (2.22), the value of B is initialized as (Liu and Liu, 2003, 2010; Monaghan, 1994, 2005):

$$B = \frac{100\,\rho_0\,V_{\max}^2}{\gamma} \tag{2.23}$$

The numerical speed of sound also plays the role to govern the compressibility of the fluid as would the real speed of sound. In Lee (2007), it is observed that increasing the numerical speed of sound can reduce the void generated behind a square in a uniform flow.

Again the purpose of this use of numerical speed of sounds is to allow weak compressibility for the water so that an equation of state can be used instead of solving the Poisson equation. The value of this numerical speed of sound is determined in order to limit the density variation within 1%. 1% is an acceptable tolerance per the work of Monaghan (1994, 2005). In Chapter 4, a validation case of dam-break flow through an elastic gate is shown. Fig. 4.10 is plotted with water density profiles and demonstrates that the density variation control is achieved.

2.8 Boundary Condition

2.8.1 Monaghan Repulsive Boundary Particles

As summarized by Monaghan and Kajtar (2009), there are four common types of boundary conditions in SPH. Among them Monaghan repulsive boundary particles and ghost (image) particles are two of the most widely used boundary conditions. The principle of the Monaghan repulsive boundary condition is to distribute boundary particles along the boundary which exert a Leonard-Jones type repulsive force (Monaghan, 2005) upon approaching fluid particles to prevent boundary penetration. This boundary condition considers the interaction between a rigid or elastic surface and the a fluid as a force in the acceleration equation of the fluid (Monaghan and Kajtar, 2009). The use of the normal forces went back to Sirovich (1968) and Peskin (1977) while Sirovich (1968) deals with rigid boundaries and Peskin (1977) with elastic surfaces. Monaghan (1994) was the first to apply the repulsive boundary condition into incompressible flow, but with this approach the fluid feels a non-zero tangential force along the boundary. Monaghan has since improved upon this boundary force model to conserve linear and angular momentum (Monaghan, 2005). Although this boundary model can not remove the boundary deficiency problem inherent in the SPH formulation near the

boundary, it is preferred due to its advantage of simple application in complicated geometry and less computational time compared with the ghost particles approach discussed in Section 2.8.2.

A detailed description of the Monaghan type boundary condition is found in Monaghan and Kos (1999), Gómez-Gesteira et al. (2010), Rogers and Dalrymple (2008) and listed here for reference. The force per unit mass (acceleration) acting from a boundary particle to a fluid particle within its neighboring domain is (Gómez-Gesteira et al., 2010; Monaghan and Kos, 1999; Rogers and Dalrymple, 2008):

$$\vec{f_{BtoF}} = \vec{n}R(\eta)P(\xi) \tag{2.24}$$

where $\vec{n}$ is the normal of the boundary particle. η is the normal distance from the fluid particle to the boundary particle. ξ is the distance between the fluid particle and the boundary particle projected on the tangent of the boundary particle. R and P are acceleration functions related to the normal and tangential distance of a fluid particle a relative to a boundary particle b.

$$R(\eta) = A\frac{1-q}{\sqrt{q}} \tag{2.25}$$

In which $q = \dfrac{\eta}{2\Delta p}$ and Δp is the boundary particle spacing. The term $2\Delta p$ determines the cut-off-distance in which the fluid particles experience the repulsive forces from boundary particles. $A = \dfrac{1}{h}\left(0.01{c_a}^2 + \beta\, c_a \mathbf{V}_{ab}\, \mathbf{n}_b\right)$. c is the numerical speed of sound of fluid particles, and:

$$\beta = \begin{cases} 0 & \text{if } \mathbf{V}_{ab} > 0 \quad \text{Departing} \\ 1 & \text{if } \mathbf{V}_{ab} < 0 \quad \text{Approaching} \end{cases}$$

$$P(\xi) = \frac{1}{2}\left(1 + \cos\left(\frac{\pi\xi}{\Delta p}\right)\right) \tag{2.26}$$

2.8.2 Ghost Particles

Another widely used boundary condition is to introduce ghost particles. Ghost particles are similar to the concept of ghost cells in a grid method. The properties (such as positions, density, velocity, etc) of the ghost particles are extrapolated from the SPH fluid particles inside the boundaries. The normal velocity has the opposite sign and the tangential velocity will have either the same sign or the opposite sign depending on free slip or no slip condition. Libersky et al. (1993) started to use the "image particles" for SPH solving structural dynamics which is similar to the idea of ghost particles. The ghost particles applied into free-surface flow can be found in the work by Colagrossi and Landrini (2003), Oger et al. (2006), Delorme et al. (2009). Colagrossi and Landrini (2003) use ghost particles to simulate the boundary of a moving wave-maker. Oger et al. (2006) generate the ghost particles along the boundary of a wedge which is free to drop into a static water tank. Delorme et al. (2009) performed a numerical simulation of flow inside a sloshing tank and at the boundary of the sloshing tank ghost particles are mirrored from inside the tank to prevent water penetration.

There are two kinds of ghost particles, static and dynamic. Static ghost particles are initialized at the beginning of the simulation and their properties are not updated. For example, a water column inside a static water tank can use this static ghost particles boundary conditions. The properties of the dynamic ghost particles require the information of the fluid inside the domain which is then mirrored at each time step. Both ghost particle boundary conditions can greatly alleviate the boundary deficiency problem in SPH since the fluid particles near the boundary will not have truncated boundaries. However, although mirroring of ghost particles is relatively easy for a rectangular shape, more computational time is needed once the boundaries are experiencing non-linear deformation. If the thickness of an object undergoing deformation is small, the mirrored ghost particles from the fluid particles on both sides of boundaries may be located within the fluid domain and special treatment is needed to solve this boundary clipping problem. It is computationally doable but more expensive than the Monaghan repulsive boundary condition.

Most simulation and validation results in this thesis use a Monaghan boundary condition. Cases partly or fully using ghost particles are the boundaries in the case of Couette flow in Section 2.11.1, water column boundaries in the case of air bubble rise in water in Section 2.11.3, and the bottom boundary of the water in the case of Surface Effect Ship in Chapter 5.

2.9 Time Integration Scheme

The Predictor-Corrector time integration scheme is implemented for the SPH model (Gómez-Gesteira et al., 2010):

$$\begin{aligned} \frac{\mathrm{d}\vec{v}_a}{\mathrm{d}t} &= \vec{\dot{v}}_a \\ \frac{\mathrm{d}r_a}{\mathrm{d}t} &= \vec{v}_a \\ \frac{\mathrm{d}\rho_a}{\mathrm{d}t} &= \dot{\rho}_a \end{aligned} \tag{2.27}$$

Intermediate variables are first calculated at the half time step and the variables are denoted with superscripts "*" (Gómez-Gesteira et al., 2010):

$$\begin{aligned} \vec{v}_a^* &= \vec{v}_a^n + \frac{\Delta t}{2}\vec{\dot{v}}^n \\ \vec{r}_a^* &= \vec{r}_a^n + \frac{\Delta t}{2}\vec{v}^n \\ \vec{\rho}_a^* &= \vec{\rho}_a^n + \frac{\Delta t}{2}\vec{\dot{\rho}}^n \end{aligned} \tag{2.28}$$

The predicted pressure is calculated from the equation of state $P_a^* = f(\rho_a^*)$. The variables at the half time step are then corrected by (Gómez-Gesteira et al., 2010):

$$\begin{aligned} \vec{v}_a^{**} &= \vec{v}_a^n + \frac{\Delta t}{2}\vec{\dot{v}}^* \\ \vec{r}_a^{**} &= \vec{r}_a^n + \frac{\Delta t}{2}\vec{v}^* \\ \vec{\rho}_a^{**} &= \vec{\rho}_a^n + \frac{\Delta t}{2}\vec{\dot{\rho}}^* \end{aligned} \tag{2.29}$$

The values at a new time step are updated as the following (Gómez-Gesteira et al., 2010):

$$\begin{aligned} \vec{v}_a^{n+1} &= 2\vec{v}_a^{**} - \vec{v}_a^{n} \\ \vec{r}_a^{n+1} &= 2\vec{r}_a^{**} - \vec{r}_a^{n} \\ \vec{\rho}_a^{n+1} &= 2\vec{\rho}_a^{**} - \vec{\rho}_a^{n} \end{aligned} \tag{2.30}$$

The pressure is updated according to the equation of state $P_a^{n+1} = f(\rho_a^{n+1})$.

2.10 Stability Condition

2.10.1 Time Step

Most of the cases under investigation involve high Reynolds number flow and the CFL conditions governing the convective terms become important for numerical stability. The time step based on CFL condition is expressed in Equation (2.31) :

$$\Delta t \leqslant \mathrm{CFL}\frac{h}{C_{n0}} \tag{2.31}$$

In the case of Couette flow in Section 2.11.1, viscosity terms become important and the time step based on viscous diffusion (Morris et al., 1997) is listed in Equation (2.32) where h is the smoothing length.

$$\Delta t \leqslant 0.125\frac{h^2}{\nu} \tag{2.32}$$

2.10.2 Moving Least Square Method

Boundary deficiency remains a subtle problem for the SPH model. For regularly spaced interior particles, SPH can achieve second-order accuracy (Liu and Liu, 2003, 2010). However, the

support domain of the particles near the boundary is truncated and even loses zeroth order consistency when particles are distributed irregularly (Liu and Liu, 2010). To remedy the boundary deficiency, methods based on correcting the kernel function and its derivatives have been proposed and summarized in Belytschko et al. (1998). Among them, a Moving Least Square scheme has been applied to interfacial flow problems (Colagrossi and Landrini, 2003) to restore the consistency of the SPH model. It is found that MLS is also critical for the stability of the numerical scheme (Colagrossi and Landrini, 2003). Without MLS correction, the hydrodynamic pressure of the water oscillates at the boundary due to boundary deficiency problem and propagates into the interior domain, causing spurious pressure leading to instability. In this analysis, the same approach of a periodic density re-initialization as found in Colagrossi and Landrini (2003) has been applied to prevent numerical drift in density. Density re-initialization using MLS correction also smooths density and pressure gradients. The detailed principles and applications of MLS may be found in the work by Belytschko et al. (1998); Colagrossi and Landrini (2003); Dilts (1999).

2.11 Validation of SPH Model

2.11.1 Couette Flow

A Couette flow case is simulated using Cleary's viscosity model. The smoothing length h is set to $3\,\mathrm{d}p$, where $\mathrm{d}p$ is the initial rectilinear particle spacing. Three rows of boundary particles are distributed at both the top and bottom boundaries to counteract boundary deficiency effects as in Fig. 2.1. The top boundary particles move with constant velocity v_0 while the bottom boundary remains fixed. Horizontal domain bounds use a periodic boundary condition as described in Gómez-Gesteira et al. (2010). The exact solution of this flow is given in Batchelor (1967) and expressed in Eq. (2.33). Figure 2.2 presents comparison of the numerical and exact solutions showing good agreement:

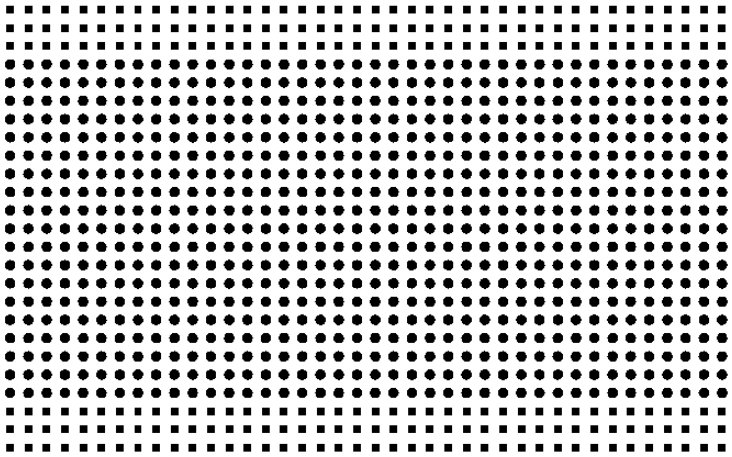

Figure 2.1: Couette flow configuration. (• Fluid particles. ■ Boundary particles.)

$$v_x(z,t) = \frac{v_0}{L}z + \sum_{n=1}^{\infty} \frac{2v_0}{n\pi}(-1)^n \sin\left(\frac{n\pi}{L}z\right) \exp^{-\nu\frac{n^2\pi^2}{L^2}t} \tag{2.33}$$

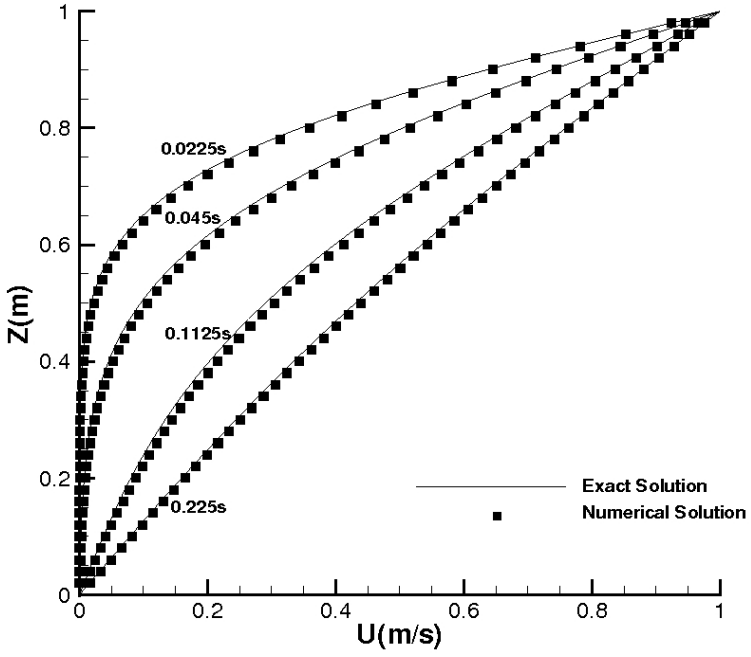

Figure 2.2: Couette flow verification result.

A convergence study is performed for this benchmark case to investigate the performance of SPH

model with the change of spatial and temporal discretization. Four spatial discretizations are run at the same time step dt=2.63E-5s . The discretization errors at four time instants (0.0225s, 0.045s, 0.1125s and 0.225s) are calculated and averaged. The order of accuracy for a scaling factor of 2 is computed as (Oberkampf and Roy, 2010):

$$n = \frac{ln(\varepsilon_{2h}/\varepsilon_h)}{2} \tag{2.34}$$

Table 2.1: Order of accuracy for temporal discretizations.

Number of particles	Water Spacing (m)	Discretization Error	Order of Accuracy
800	5.E-5	21.07	
3200	2.5E-5	11.93	0.82
12800	1.25E-5	6.53	0.87
51200	6.25E-6	3.43	0.93

To investigate the effect of time steps, water spacing is chosen as 1.25E-5 m and four CFL numbers are chosen. Same approaches are adopted to calculate the order of accuracy:

Table 2.2: Order of accuracy for spatial discretizations.

CFL	Time step (s)	Discretization Error	Order of Accuracy
0.5	5.26E-5	16.08	
0.25	2.63E-5	6.53	1.30
0.125	1.32E-5	2.59	1.33
0.0625	6.58E-6	0.98	1.40

2.11.2 Flow in a Sloshing Tank

A flow inside a sloshing tank case is simulated to further validate the SPH model and have a look at the fluid-structure interaction force using this model. This validation test also provided a foundation for later fluid-structure interaction force work between fluid and deformable structures in Chapter 4. The numerical results obtained are compared with the experimental data published in Souto-Iglesias et al. (2006). The initial configuration is illustrated in Fig. 2.3. Monaghan type boundary particles are distributed along the the sloshing tank boundaries. SPH fluid particles are distributed uniformly to a finite depth and initialized with hydrostatic pressure. The tank oscillates with a prescribed sinusoidal motion with the rotation center 10 cm under the bottom center of the tank. The simulation parameters for this validation case are listed in Table 2.3:

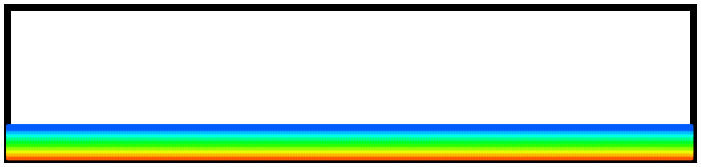

Figure 2.3: Initial configuration of sloshing tank case with water particles colored by hydrostatic pressure scaled from 0 to 300 pa.

Table 2.3: Simulation parameters. (Geometry is per Souto-Iglesias et al. (2006).)

Tank height	0.14 (m)
Tank width	0.64 (m)
Tank thickness	0.252 (m)
Water height	0.03 (m)
Max roll angle	6°
Sloshing frequency	4.34 or 4.87 (rad/s)
Water spacing	0.0015 (m)
Boundary particle spacing	0.001 (m)
No. of fluid particles	8967
No. of boundary particles	1568
dt	2.67E-6(s)
Simulation time	0–12(s)
Computer time used	90(h)

The validation measurement for this case is the total moment exerted upon the sloshing tank about the rotation center. Souto-Iglesias et al. (2006) published the amplitude of moment with different sloshing frequency as in Fig. 2.4. It is noted that there is a substantial drop in amplitude between Point A at ω=4.34 rad/s with amplitude about 7 N.m and Point B at ω=4.87 rad/s with amplitude dropped to about 2.5 N.m. This is due to the different characteristics of the free surface flow inside the sloshing tank which will be presented below. In addition to the experimental results in Souto-Iglesias et al. (2006), numerical simulation was also performed by using SPH models and proved the feasibility of SPH models. It is therefore interesting to see if the developed in-house

SPH code can simulate these two cases of flow which are sensitive to the sloshing frequency. The time history of the total moment upon the sloshing tank about the rotation center is recorded. Each fluid particle close to the boundary particles will experience a Monaghan-type repulsive force as described in Eq. (2.24). The opposite of this force is taken as the force from the fluid particles to the boundary particle. Summing up all the opposite of the repulsive forces from the boundary particles to other fluid particles result in the total force from the fluid to this boundary particle. Iterating upon this procedure for all the boundary particles and then summing the force on each boundary particle multiplied by its distance from the rotation center yields the total moment from the fluid upon the tank about the rotation center per unit thickness. Since the simulation case is in 2D and the tank is 3D, the final moment needs to be multiplied by the tank thickness 0.252 m to obtain the final moment value. Figure 2.5 and Figure 2.6 demonstrate the time history of the moment on the sloshing tank at sloshing frequencies of 4.34 and 4.87 rad/s respectively, which correspond to Point A and Point B in Fig. 2.4. Simulation of one cycle of motion for each case is plotted in Fig. 2.7 and Fig. 2.8.

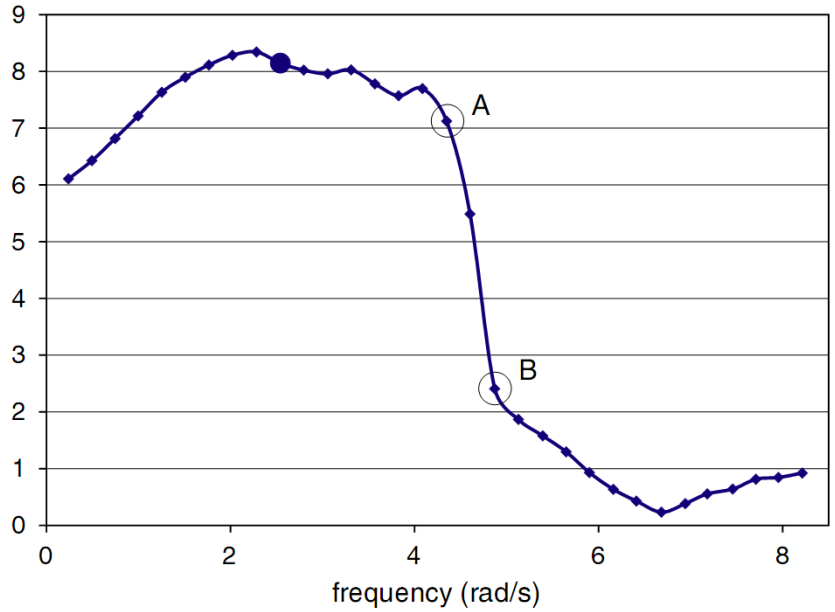

Figure 2.4: Amplitude of moment upon the sloshing tank with the change of sloshing frequency by Souto-Iglesias et al. (2006).

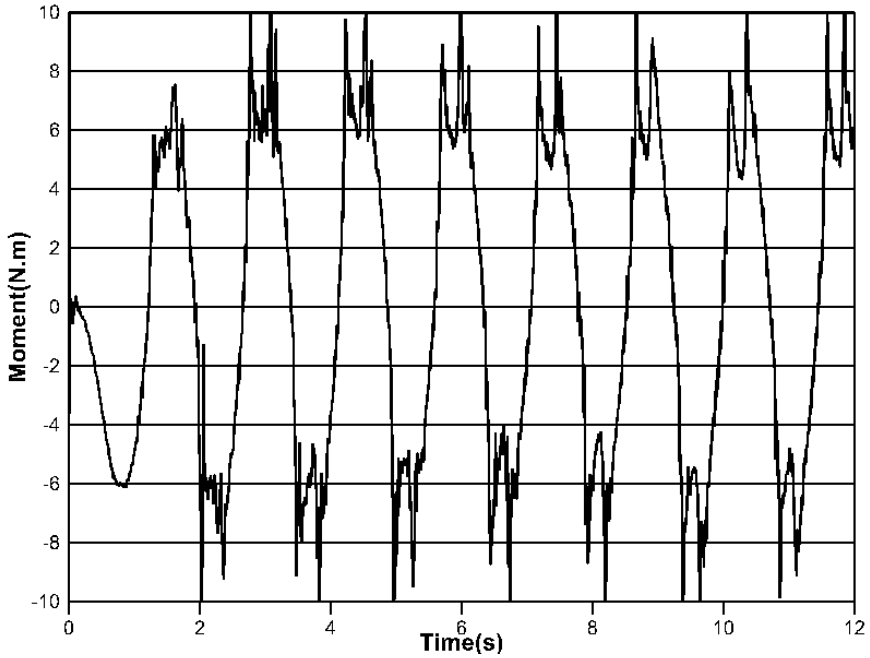

Figure 2.5: Time history of total moment upon sloshing tank for sloshing frequency ω=4.34 rad/s using SPH formulation.

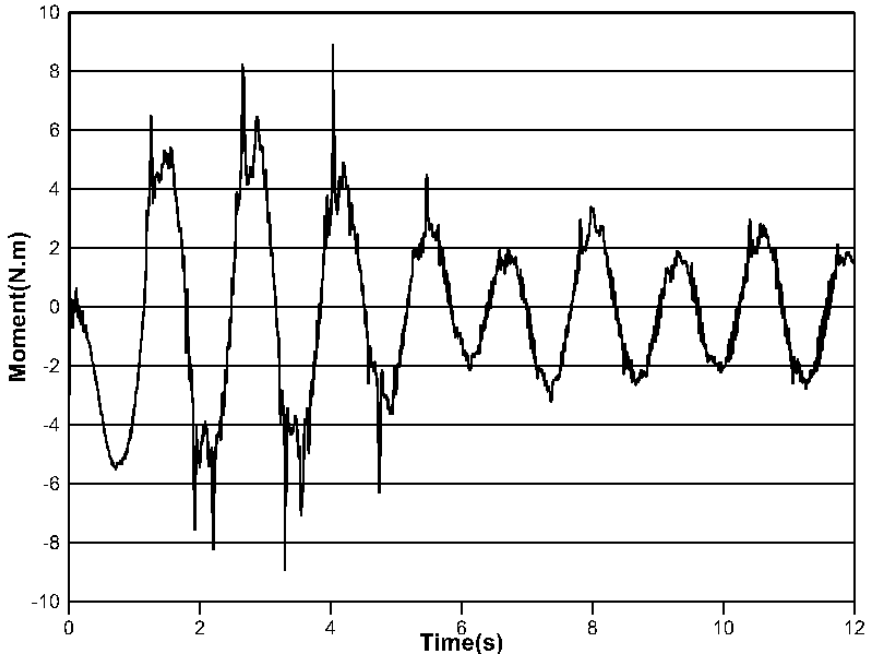

Figure 2.6: Time history of total moment upon sloshing tank for sloshing frequency ω=4.87 rad/s using SPH formulation.

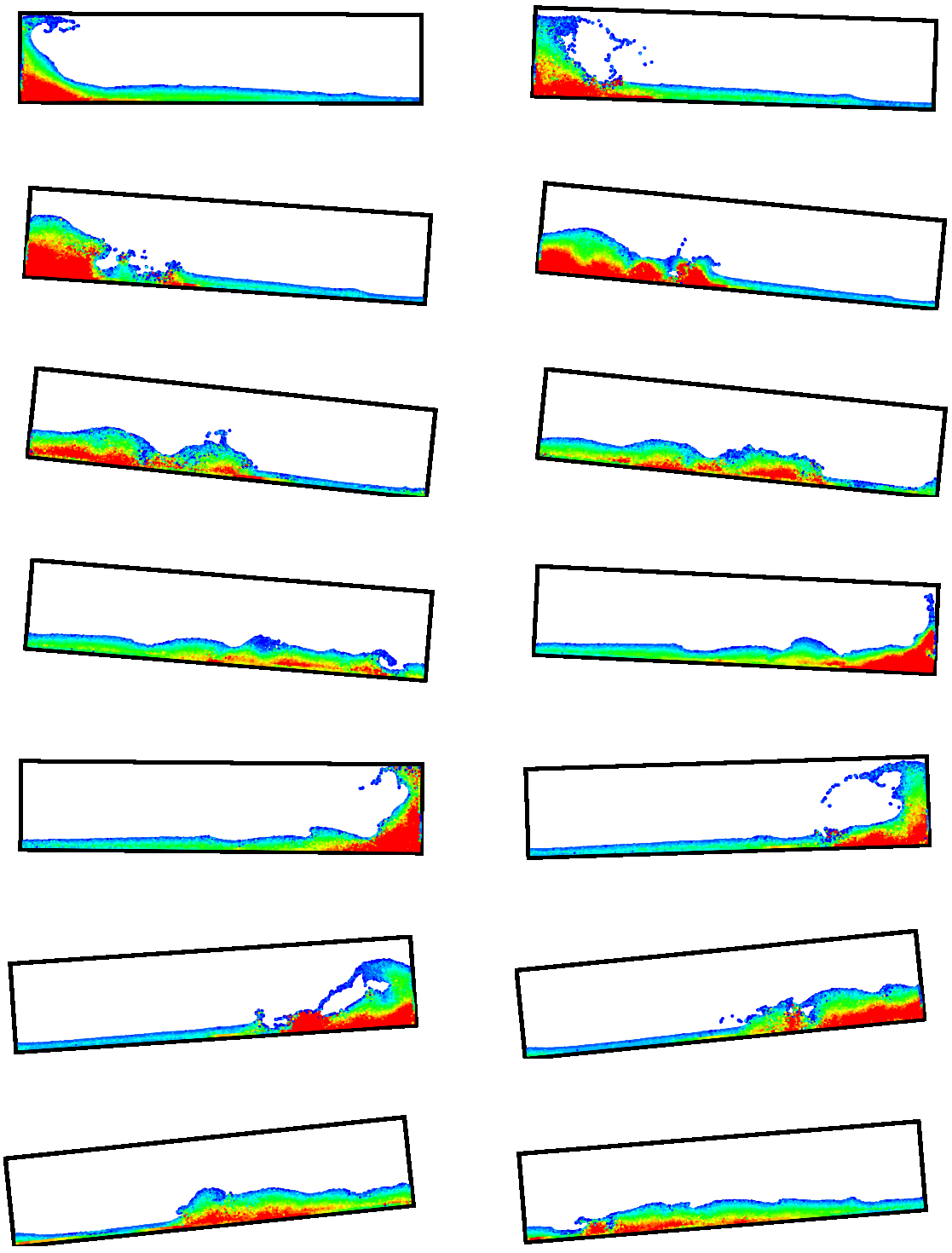

Figure 2.7: Simulation of a complete period for sloshing frequency ω =4.87 rad/s with SPH particles colored by the pressure scaled from 0 pa to 300 pa.

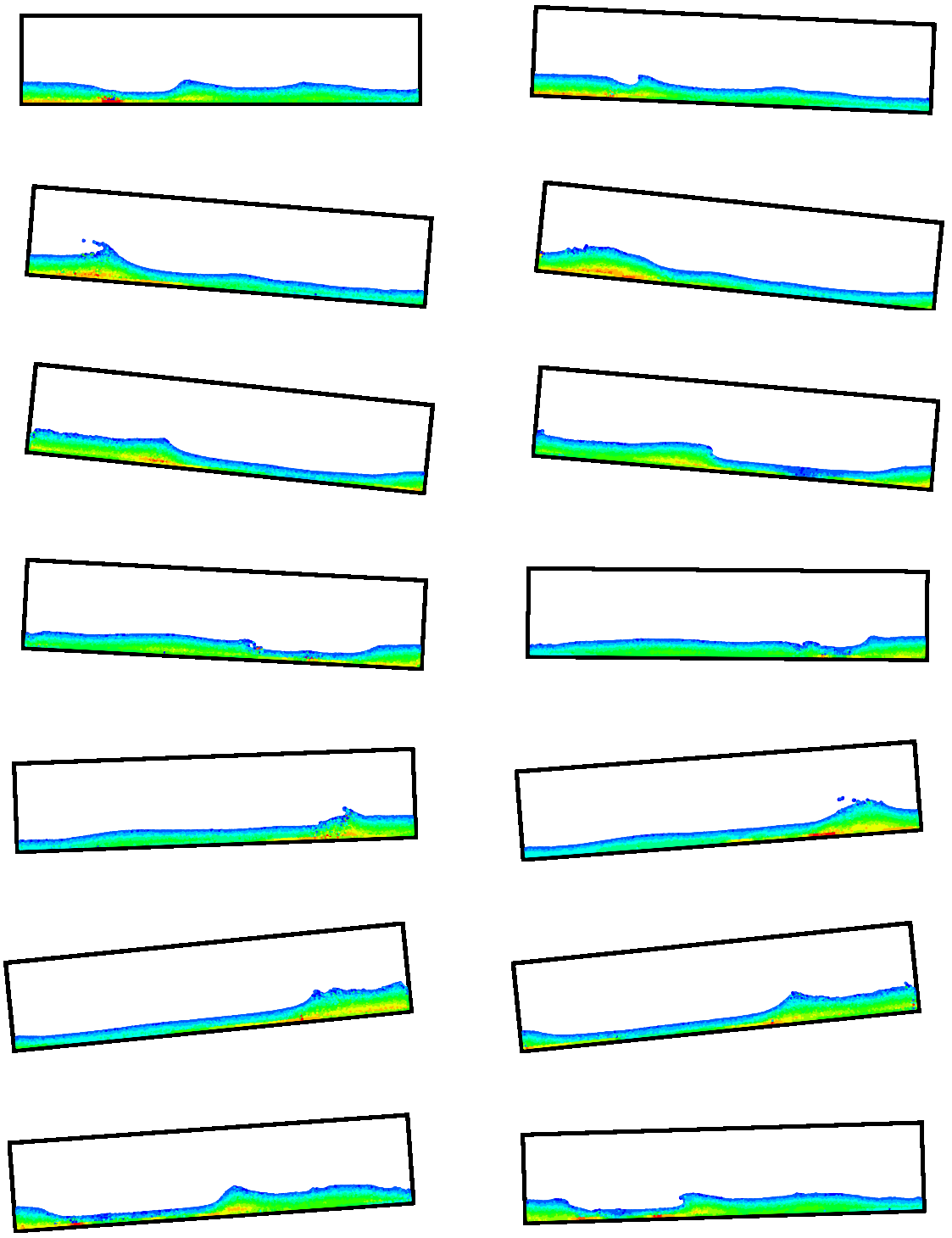

Figure 2.8: Simulation of a complete period for sloshing frequency ω=4.34 rad/s with SPH particles colored by the pressure scaled from 0 pa to 300 pa.

Figure 2.5 shows a periodic feature after the first cycle while Figure 2.5 reaches periodic behavior

after 6s. The average peak amplitude for a sloshing frequency of 4.34 rad/s is 6.76 N.m and 2.28 N.m for sloshing frequency of 4.87 rad/s. These two values are very close to the values in Fig. 2.4 by Souto-Iglesias et al. (2006). The drop in the amplitude can be explained by Fig. 2.7 and Fig. 2.8. In Fig. 2.7, the traveling wave climbs up and reaches the top of the tank when the tank reaches maximum roll angle. However, for the larger sloshing frequency ω=4.87 rad/s, the traveling wave can not follow the motion of the tank and a traveling wave will encounter a reflecting wave in the middle of the tank and breaks, so that the tank will experience less moment. Figures 2.5 to Fig. 2.8 show that the SPH solver developed can not only capture the main feature of the free surface flow, but also transmit accurate forces between fluids and boundaries for further investigation of force transmission between fluids and deformable structures.

A convergence study is performed for this case to investigate the change of results with variations of spatial and temporal discretization. Four spatial discretizations are run with the same time step dt=2.67E-6s and ω = 4.34 rad/s. The results are summarized in Table 2.4:

Table 2.4: Average amplitude of sloshing tank cases with ω = 4.34 rad/s for different spatial discretizations.

Number of particles	Water Spacing (m)	Average Amplitude (N.m)
1261	0.004	5.92
5044	0.002	6.52
8967	0.0015	6.76
20176	0.001	6.82

To investigate the effect of time steps, water spacing is chosen as 0.0015 m and three CFL numbers are chosen. The results are summarized in Table 2.5:

Table 2.5: Average amplitude of sloshing tank cases with ω = 4.34 rad/s for different time steps.

CFL	Time step (s)	Average Amplitude (N.m)
0.25	2.67E-6	6.76
0.125	1.34E-6	6.77
0.0625	6.71E-7	6.77

From Table 2.4 and Table 2.5 it can be seen that the results are more sensitive to spatial discretizations than temporal discretizations. With refinement of mesh and time steps, the average moment amplitudes show convergence.

2.11.3 Air Bubble Rise in Water

To test the capability of SPH handling multi-phase flow and as a key step for later investigation of hovercraft, a classic air-bubble rise in water case is simulated. A circular air-bubble is initially placed near the bottom of the water domain. The air bubble will rise due to the pressure gradient in the water. The SPH formulation is based on the improved continuity and momentum equation for small-density-ratio interfacial flow. The Tait equation of state is used for water and the ideal gas law is applied to the air particles. Figure 2.9 shows the whole simulation. The model is initialized with symmetric distribution. However, with the development of the simulation, asymmetric shedding of air bubbles is observed. Small differences, such as truncation error stored in the acceleration or velocity of the particles may gradually induce this asymmetry. However, increasing the number of particles and refining the time step did not alleviate this asymmetry. This would be an interesting case for further study. Unfortunately, the published work to which this is compared (Colagrossi and Landrini, 2003) only shows the half-plane result and presumes symmetry. By comparison with Fig. 6 in Colagrossi and Landrini (2003), it is found that the characteristic saddle

shape of the bubble is formed and small air bubble shedding is also observed. This bubble rise example is developed to test the stability of SPH code dealing with multi-phase flow. The successful simulation of this case paves the way for the later simulation of cushioned air inside the chamber of ACV or SES interacting with the incoming water.

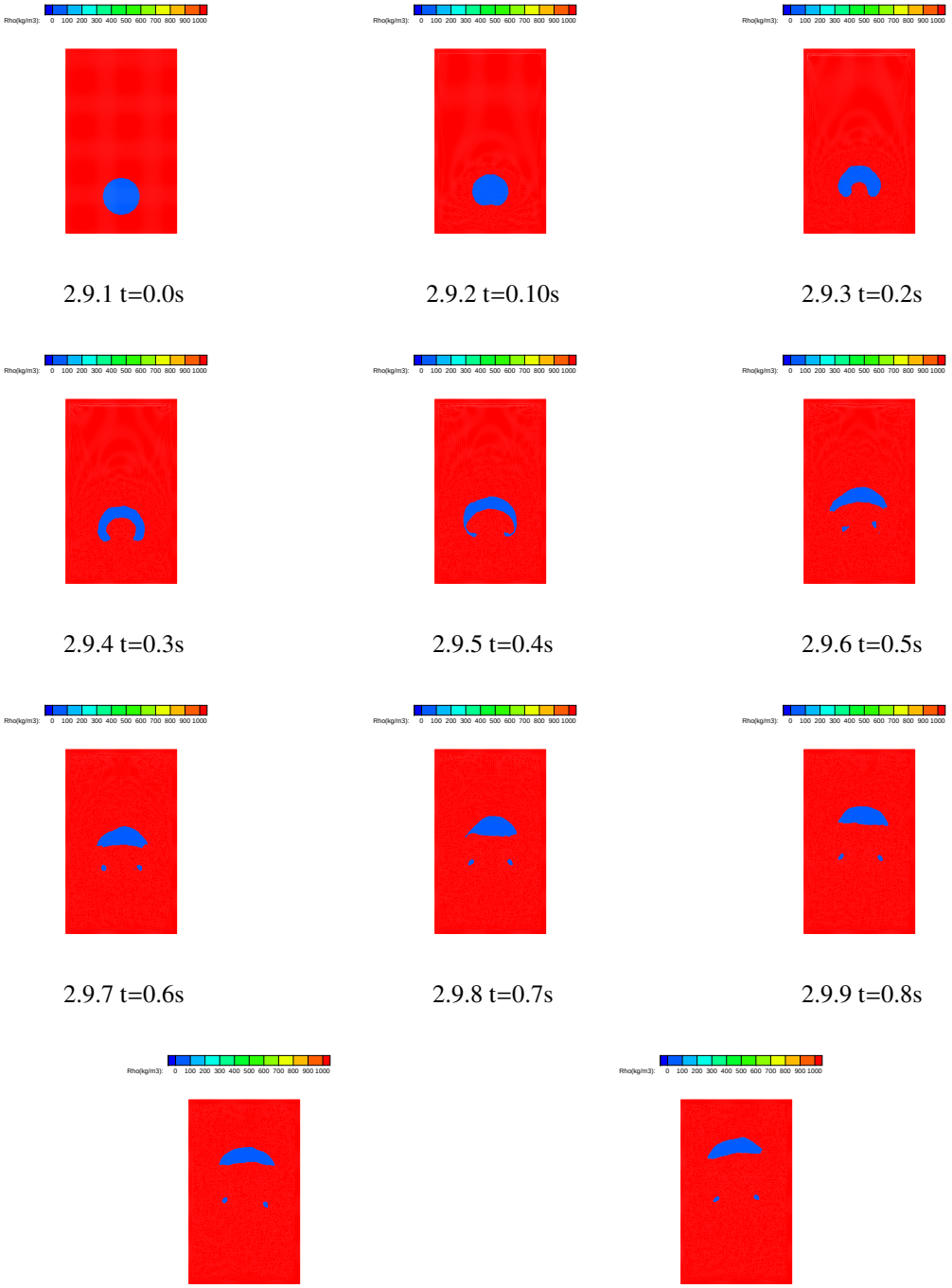

2.9.1 t=0.0s 2.9.2 t=0.10s 2.9.3 t=0.2s

2.9.4 t=0.3s 2.9.5 t=0.4s 2.9.6 t=0.5s

2.9.7 t=0.6s 2.9.8 t=0.7s 2.9.9 t=0.8s

2.9.10 t=0.9s 2.9.11 t=1.0s

Figure 2.9: Simulation results for every 0.1s. SPH particles colored by density. (Blue part for air and red part for water.)

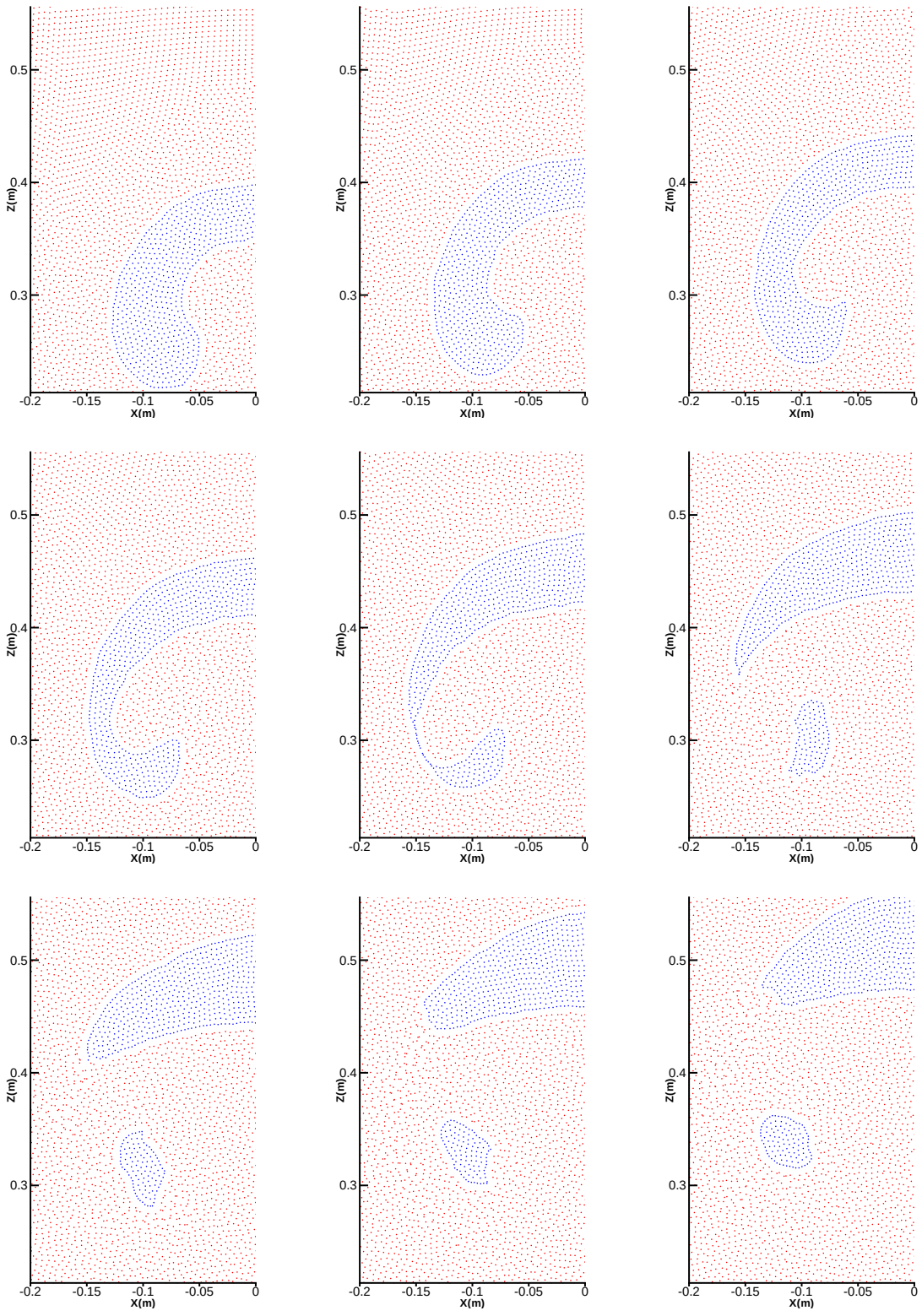

Figure 2.10: Simulation results for every 0.1s. SPH particles colored by density. (Blue part for air and red part for water.)

Chapter 3

Finite-Deformation Formulation of Finite Element Methods

3.1 Introduction

The purpose of this chapter is to give a brief overview to finite element methods. There is no new research in this chapter, rather, this lays the groundwork for research to be described in Chapter 4 and Chapter 5. The Finite Element Method (FEM) is an established numerical tool for analysis of structural systems. The start of FEM traces back to Turner et al. (1956), recognized as the first comprehensive treatment of FEM. Many classic textbooks and papers have been published to fulfill the development of the FEM theory (Bathe, 1996; Bathe et al., 1975; Cook, 1974; Oden, 1972; Zienkiewics and Taylor, 2005; Zienkiewics et al., 2005).

FEM formulation can be obtained through different approaches like the Galerkin method, variational methods or the principle of virtual work, etc (Cook, 1974; Zienkiewics et al., 2005). In this analysis, the FEM formulation is derived from the principle of virtual work due to its straightforwardness in physical understanding. Corresponding to the Lagrangian nature of SPH, a Lagrangian rather than an Eulerian perspective of FEM is utilized. A small-deformation FEM formulation is

first described followed by a finite-deformation (large-deformation) FEM. In the finite-deformation FEM, there are Total Lagrangian and Updated Lagrangian formulations. The Updated Lagrangian formulation is adopted due to its conciseness of matrix assembly. Both formulations should be numerically identical (Bathe, 1996; Bathe et al., 1975).

In this chapter, the FEM formulation is first derived from the principle of virtual work for a general continuous structure (Bathe, 1996; Cook, 1974; Zienkiewics and Taylor, 2005). A plane isoparametric formulation is used for general displacement-based problems. A finite-deformation formulation of an FEM model is then described for dealing with structure undergoing large deformation. Material constitutive relation for both linear elasticity and hyperelasticity are given. Numerical methods to obtain the solutions for both static and dynamic problem are also described. Comparison results are provided and show good results with theoretical results (Timoshenko and Goodier, 1970) and Abaqus results.

3.2 FEM Formulation Using the Principle of Virtual Work

The equilibrium equations for the force acting on an internal structural element is:

$$\sigma_{ji,j} + b_i = \rho \ddot{u}_i \tag{3.1}$$

The variational description of virtual work for an elastic body is obtained by multiplying Eq. (3.1) a virtual displacement δu_i and integrating over the domain (Bathe, 1996; Cook, 1974; Zienkiewics and Taylor, 2005):

$$\delta\Pi = \int_\omega \delta u_i \left[\rho \ddot{u}_i - \sigma_{ji,j} - b_i\right] \mathrm{d}\omega = 0 \tag{3.2}$$

By performing an integration by parts and applying Gauss Theorem:

$$\delta\Pi = \int_\omega \delta u_i \rho \ddot{u}_i \,\mathrm{d}\omega + \int_\omega \delta\varepsilon_{ij}\sigma_{ij} \,\mathrm{d}\omega - \int_\omega \delta u_i \rho b_i \,\mathrm{d}\omega - \int_{\gamma_t} \delta u_i t_i \,\mathrm{d}\gamma = 0 \tag{3.3}$$

Π Total energy including potential energy and external work

σ_{ij} Cauchy stress

u_i Nodal displacement

b_i body force

t_i boundary traction

$\mathrm{d}\omega$ Elemental area

$\mathrm{d}\gamma$ Elemental boundary

Discontinuities are absent in this research so it is reasonable to assume an irreducible, or displacement form of the finite element methods. The problem domain Ω is divided into individual elements and the weak form of the equilibrium condition can be written as (Bathe, 1996; Bathe et al., 1975; Zienkiewics and Taylor, 2005):

$$\delta\Pi \approx \delta\hat{\Pi} = \sum_e \left[\int_{\omega_e} \delta u_i \rho \ddot{u}_i \,\mathrm{d}\omega + \int_{\omega_e} \delta\varepsilon_{ij}\sigma_{ij} \,\mathrm{d}\omega - \int_{\omega_e} \delta u_i \rho b_i \,\mathrm{d}\omega \right] - \sum_{et} \left[\int_{\gamma_{te}} \delta u_i t_i \,\mathrm{d}\gamma \right] = 0 \quad (3.4)$$

The major topic covered in this thesis is analyzed in two-dimensional simulation. Plane stress and plane strain models are assumed and more details of them are discussed in Section 3.5. Under small deformation, the Cauchy infinitesimal strain tensor ε_{ij} is related to the displacements by the strain-displacement relationship:

$$\varepsilon_{ij} = \begin{bmatrix} \varepsilon_{xx} \\ \varepsilon_{yy} \\ \gamma_{xy} \end{bmatrix} = \begin{bmatrix} \frac{\partial}{\partial x} & 0 \\ 0 & \frac{\partial}{\partial y} \\ \frac{\partial}{\partial y} & \frac{\partial}{\partial x} \end{bmatrix} \begin{bmatrix} u \\ v \end{bmatrix} = D\mathbf{u} \quad (3.5)$$

Considering Eq. (3.5), the vector form of Eq. (3.4) is expressed as (Zienkiewics and Taylor, 2005):

$$\delta\hat{\Pi} = \sum_e \left[\int_{\omega_e} \delta\mathbf{u}^T \rho \ddot{\mathbf{u}} \, \mathrm{d}\omega + \int_{\omega_e} \delta \left(D\mathbf{u}\right)^T \boldsymbol{\sigma} \, \mathrm{d}\omega - \int_{\omega_e} \delta\mathbf{u}^T \rho \mathbf{b} \, \mathrm{d}\omega \right] - \sum_{et} \left[\int_{\gamma_{t_e}} \delta\mathbf{u}^T \mathbf{t} \, \mathrm{d}\gamma \right] \tag{3.6}$$

$$= \sum_e \delta\hat{\Pi}^e + \sum_{et} \delta\hat{\Pi}_t^e = 0 \tag{3.7}$$

$\delta\hat{\Pi}^e$ are total energy variations within an element and $\delta\hat{\Pi}_t^e$ are along the boundary traction surfaces γ_{t_e}. The fundamental idea for the displacement approximation at any point and any time in the finite element method is to introduce a shape function, $\mathbf{N}$, and interpolate displacements $\mathbf{u}$ and displacement variation $\delta\mathbf{u}$ inside an element using its nodal displacements:

$$\mathbf{u}(\mathbf{x}, t) \approx \hat{\mathbf{u}} = \sum_b N_b(\mathbf{x}) \tilde{\mathbf{u}}_b(t) = \mathbf{N}\tilde{\mathbf{u}} \tag{3.8}$$

$$\delta\mathbf{u}(\mathbf{x}, t) \approx \delta\hat{\mathbf{u}} = \sum_b N_b(\mathbf{x}) \delta\tilde{\mathbf{u}}_b(t) = \mathbf{N}\delta\tilde{\mathbf{u}} \tag{3.9}$$

Where notations with " ˜ " indicate nodal variables and b is the number of element nodes. For example, if triangular elements are used, b iterates from 1 to 3 while for rectangular elements b iterates from 1 to 4. Choosing a shape function which has continuous first-order spatial derivative $\mathbf{B}$ (Bathe, 1996; Bathe et al., 1975; Zienkiewics and Taylor, 2005):

$$\mathbf{B} = \begin{bmatrix} \dfrac{\partial}{\partial x} & 0 \\ 0 & \dfrac{\partial}{\partial y} \\ \dfrac{\partial}{\partial y} & \dfrac{\partial}{\partial x} \end{bmatrix} \mathbf{N} = D\mathbf{N} \tag{3.10}$$

Combining Eq. (3.8) and Eq. (3.10) into Eq. (3.5) and get the strain and stress under small-deformation assumption (Bathe, 1996; Bathe et al., 1975; Zienkiewics and Taylor, 2005):

$$\boldsymbol{\varepsilon} = D\mathbf{u} \approx \left(DN_b\right) \tilde{u}_b = \sum_b \mathbf{B}_b \tilde{\mathbf{u}}_b = \mathbf{B}\tilde{\mathbf{u}} \tag{3.11}$$

$$\boldsymbol{\sigma} = \mathbf{C}\,\boldsymbol{\varepsilon} = \mathbf{CB}\tilde{\mathbf{u}} \tag{3.12}$$

C is the elastic moduli of the material. Substituting Eqs. (3.9) and (3.12) into Eq. (3.6) yields the equilibrium condition for one element (Bathe, 1996; Bathe et al., 1975; Zienkiewics and Taylor, 2005):

$$\delta\hat{\Pi}^e = \delta\tilde{\mathbf{u}}^T \left[\int_{\omega_e} \mathbf{N}^T \rho \mathbf{N}\, \mathrm{d}\omega \ddot{\tilde{\mathbf{u}}} + \int_{\omega_e} \mathbf{B}^T \mathbf{CB}\, \mathrm{d}\omega \tilde{\mathbf{u}} - \int_{\omega_e} \mathbf{N}^T \mathbf{b}\, \mathrm{d}\omega - \int_{\gamma_{t_e}} \mathbf{N}^T \bar{\mathbf{t}}\, \mathrm{d}\gamma \right] = 0 \tag{3.13}$$

Noting that for arbitrary virtual displacement $\delta\tilde{\mathbf{u}}$ Eq. (3.13) is satisfied which gives the relations:

$$\int_{\omega_e} \mathbf{N}^T \rho \mathbf{N}\, \mathrm{d}\omega \ddot{\tilde{\mathbf{u}}} + \int_{\omega_e} \mathbf{B}^T \mathbf{CB}\, \mathrm{d}\omega \tilde{\mathbf{u}} - \int_{\omega_e} \mathbf{N}^T \mathbf{b}\, \mathrm{d}\omega - \int_{\gamma_{t_e}} \mathbf{N}^T \bar{\mathbf{t}}\, \mathrm{d}\gamma = 0 \tag{3.14}$$

and can be further expressed as (Bathe, 1996; Bathe et al., 1975; Zienkiewics and Taylor, 2005):

$$\mathbf{M}^e \ddot{\tilde{\mathbf{u}}} + \mathbf{K}^e \tilde{\mathbf{u}} = \mathbf{f}^e \tag{3.15}$$

$\mathbf{M}^e = \int_{\omega_e} \mathbf{N}^T \rho \mathbf{N}\, \mathrm{d}\omega$ Element mass matrix

$\mathbf{K}^e = \int_{\omega_e} \mathbf{B}^T \mathbf{CB}\, \mathrm{d}\omega$ Element stiffness matrix

$\mathbf{f}^e = \int_{\omega_e} \mathbf{N}^T \mathbf{b}\, \mathrm{d}\omega + \int_{\gamma_{t_e}} \mathbf{N}^T \bar{\mathbf{t}}\, \mathrm{d}\gamma$ Element nodal forces

By summing over all the elements, the global mass and stiffness matrix can be assembled and the equilibrium condition boils down to (Zienkiewics and Taylor, 2005):

$$\mathbf{M}\ddot{\tilde{\mathbf{u}}} + \mathbf{K}\tilde{\mathbf{u}} = \mathbf{f} \tag{3.16}$$

$$\mathbf{M} = \textstyle\sum_e \mathbf{M}^e; \quad \mathbf{K} = \textstyle\sum_e \mathbf{K}^e; \quad \mathbf{f} = \textstyle\sum_e \mathbf{f}^e + \mathbf{P}_{ext};$$

M Global mass matrix

K Global stiffness matrix

f Global nodal forces

$\mathbf{P}_{ext}$ External point loads on the boundary

Depending on the nature of the problem, static or dynamic, the corresponding solver is then selected to calculate the unknown displacements. The solvers used in this analysis are further discussed in Section 3.7.

3.3 Isoparametric Formulation

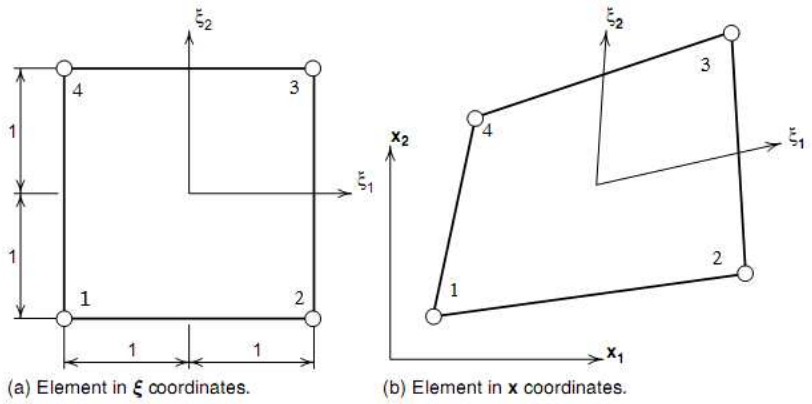

Figure 3.1: Isoparametric element coordinate systems, adapted from Cook (1974). (Left) Element mapped into square computational domain. (Right) Element in unmapped physical domain.

The FEM elements utilized in this research are quadrilateral with initialization of rectangular elements. To enable the expression of the elements after large deformation, the isoparametric formulation of the elements is introduced. Figure 3.1 shows the orientation of the coordinate in both mapped (natural coordinate) and unmapped domain (physical coordinate). The computation of a deformed object is usually performed by mapping from physical coordinate into natural coordinate due to its convenience. The index of the four nodes is in the anti-clockwise order starting from the left-bottom corner of the element. A scalar variable inside the element, ϕ, can be represented by

the interpolation of its nodal variables (Cook, 1974):

$$\phi = \sum_{b=1}^{4} N_b \phi_b \tag{3.17}$$

ϕ_b is the variable at node b. The bilinear shape function, $\mathbf{N}$, is the function of natural coordinate ξ and η (Bathe, 1996; Bathe et al., 1975; Zienkiewics and Taylor, 2005):

$$\begin{aligned} N_1 &= \frac{(1-\xi)(1-\eta)}{4} \\ N_2 &= \frac{(1+\xi)(1-\eta)}{4} \\ N_3 &= \frac{(1+\xi)(1+\eta)}{4} \\ N_4 &= \frac{(1-\xi)(1+\eta)}{4} \end{aligned} \tag{3.18}$$

The spatial derivatives with respect to the physical coordinates are usually of interest but not directly available. Using the chain rule, the spatial derivatives in both coordinates can be associated as:

$$\begin{aligned} \frac{\partial \phi}{\partial \xi} &= \frac{\partial \phi}{\partial x}\frac{\partial x}{\partial \xi} + \frac{\partial \phi}{\partial z}\frac{\partial z}{\partial \xi} \\ \frac{\partial \phi}{\partial \eta} &= \frac{\partial \phi}{\partial x}\frac{\partial x}{\partial \eta} + \frac{\partial \phi}{\partial z}\frac{\partial z}{\partial \eta} \end{aligned} \tag{3.19}$$

$$\begin{bmatrix} \dfrac{\partial \phi}{\partial \xi} \\ \dfrac{\partial \phi}{\partial \eta} \end{bmatrix} = \begin{bmatrix} \dfrac{\partial x}{\partial \xi} & \dfrac{\partial z}{\partial \xi} \\ \dfrac{\partial x}{\partial \eta} & \dfrac{\partial z}{\partial \eta} \end{bmatrix} \begin{bmatrix} \dfrac{\partial \phi}{\partial x} \\ \dfrac{\partial \phi}{\partial z} \end{bmatrix} \tag{3.20}$$

The transformation matrix, or called Jacobian matrix is defined as:

$$[\mathbf{J^{pn}}] = \begin{bmatrix} \dfrac{\partial x}{\partial \xi} & \dfrac{\partial z}{\partial \xi} \\ \dfrac{\partial x}{\partial \eta} & \dfrac{\partial z}{\partial \eta} \end{bmatrix} \tag{3.21}$$

The superscripts "**pn**" indicates this Jacobian matrix relates the physical coordinate systems to natural or computational coordinate systems. This notation is to distinguish from another Jacobian

matrix relating different configurations as will be later given in Section 3.4. The Jacobian matrix can be expressed using the spatial derivative of the shape function and nodal coordinates based on Eq. (3.17):

$$[\mathbf{J^{pn}}] = \begin{bmatrix} \dfrac{\partial N_1}{\partial \xi} & \dfrac{\partial N_2}{\partial \xi} & \dfrac{\partial N_3}{\partial \xi} & \dfrac{\partial N_4}{\partial \xi} \\ \dfrac{\partial N_1}{\partial \eta} & \dfrac{\partial N_2}{\partial \eta} & \dfrac{\partial N_3}{\partial \eta} & \dfrac{\partial N_4}{\partial \eta} \end{bmatrix} \begin{bmatrix} x_1 & z_1 \\ x_2 & z_2 \\ x_3 & z_3 \\ x_4 & z_4 \end{bmatrix} \tag{3.22}$$

In which the spatial derivative of the shape function can be derived from Eq. (3.18) (Bathe, 1996; Bathe et al., 1975; Zienkiewics and Taylor, 2005):

$$\begin{bmatrix} \dfrac{\partial N_a}{\partial \xi} \\ \dfrac{\partial N_a}{\partial \eta} \end{bmatrix} = \frac{1}{4} \begin{bmatrix} -(1-\eta) & (1-\eta) & (1+\eta) & -(1+\eta) \\ -(1-\xi) & -(1+\xi) & (1+\xi) & (1-\eta) \end{bmatrix} \tag{3.23}$$

After obtaining the Jacobian matrix, inverting Eq. (3.20) and get the spatial derivatives in the physical coordinate (Bathe, 1996; Bathe et al., 1975; Zienkiewics and Taylor, 2005):

$$\begin{bmatrix} \dfrac{\partial \phi}{\partial x} \\ \dfrac{\partial \phi}{\partial y} \end{bmatrix} = [\mathbf{\Gamma^{pn}}] \begin{bmatrix} \dfrac{\partial \phi}{\partial \xi} \\ \dfrac{\partial \phi}{\partial \eta} \end{bmatrix} \tag{3.24}$$

In which:

$$[\mathbf{\Gamma^{pn}}] = [\mathbf{J^{pn}}]^{-1} = \begin{bmatrix} \dfrac{\partial \xi}{\partial x} & \dfrac{\partial \eta}{\partial x} \\ \dfrac{\partial \xi}{\partial z} & \dfrac{\partial \eta}{\partial z} \end{bmatrix} \tag{3.25}$$

The Cauchy infinitesimal strain can then be derived from Eq. (3.5) (Bathe, 1996; Bathe et al., 1975; Zienkiewics and Taylor, 2005):

$$
\begin{bmatrix} \varepsilon_{xx} \\ \varepsilon_{zz} \\ \varepsilon_{xz} \end{bmatrix} = \begin{bmatrix} 1 & 0 & 0 & 0 \\ 0 & 0 & 0 & 1 \\ 0 & 1 & 1 & 0 \end{bmatrix} \begin{bmatrix} \dfrac{\partial u}{\partial x} \\ \dfrac{\partial u}{\partial z} \\ \dfrac{\partial w}{\partial x} \\ \dfrac{\partial w}{\partial z} \end{bmatrix}
$$

$$
= \begin{bmatrix} 1 & 0 & 0 & 0 \\ 0 & 0 & 0 & 1 \\ 0 & 1 & 1 & 0 \end{bmatrix} \begin{bmatrix} \Gamma_{11} & \Gamma_{12} & 0 & 0 \\ \Gamma_{21} & \Gamma_{22} & 0 & 0 \\ 0 & 0 & \Gamma_{11} & \Gamma_{12} \\ 0 & 0 & \Gamma_{21} & \Gamma_{22} \end{bmatrix} \begin{bmatrix} \dfrac{\partial u}{\partial \xi} \\ \dfrac{\partial u}{\partial \eta} \\ \dfrac{\partial w}{\partial \xi} \\ \dfrac{\partial w}{\partial \eta} \end{bmatrix}
$$

$$
= \begin{bmatrix} 1 & 0 & 0 & 0 \\ 0 & 0 & 0 & 1 \\ 0 & 1 & 1 & 0 \end{bmatrix} \begin{bmatrix} \Gamma_{11} & \Gamma_{12} & 0 & 0 \\ \Gamma_{21} & \Gamma_{22} & 0 & 0 \\ 0 & 0 & \Gamma_{11} & \Gamma_{12} \\ 0 & 0 & \Gamma_{21} & \Gamma_{22} \end{bmatrix} \begin{bmatrix} \dfrac{\partial N_1}{\partial \xi} & 0 & \dfrac{\partial N_2}{\partial \xi} & 0 & \dfrac{\partial N_3}{\partial \xi} & 0 & \dfrac{\partial N_4}{\partial \xi} & 0 \\ \dfrac{\partial N_1}{\partial \eta} & 0 & \dfrac{\partial N_2}{\partial \eta} & 0 & \dfrac{\partial N_3}{\partial \eta} & 0 & \dfrac{\partial N_4}{\partial \eta} & 0 \\ 0 & \dfrac{\partial N_1}{\partial \xi} & 0 & \dfrac{\partial N_2}{\partial \xi} & 0 & \dfrac{\partial N_3}{\partial \xi} & 0 & \dfrac{\partial N_4}{\partial \xi} \\ 0 & \dfrac{\partial N_1}{\partial \eta} & 0 & \dfrac{\partial N_2}{\partial \eta} & 0 & \dfrac{\partial N_3}{\partial \eta} & 0 & \dfrac{\partial N_4}{\partial \eta} \end{bmatrix} \begin{bmatrix} u_1 \\ w_1 \\ u_2 \\ w_2 \\ u_3 \\ w_3 \\ u_4 \\ w_4 \end{bmatrix}
$$

(3.26)

3.4 Finite-Deformation Finite Element Methods

The small-deformation FEM model was initially coupled with SPH for solving fluid-structure interaction problems. Qualitative results are obtained but since the structures, for the applications of interest, often undergo large geometric deformation, it is found that geometric non-linearity must be included in the FEM modeling. As such, the theory of finite-deformation FEM is emphasized in this Section. The derivation still starts with the equilibrium condition similar to Eq. (3.3) (Bathe, 1996):

$$\int_{^{t+\Delta t}\omega} \delta\, {}_{t+\Delta t}\varepsilon_{ij}\, {}^{t+\Delta t}\sigma_{ij}\, \mathrm{d}^{t+\Delta t}\omega = \int_{^{t+\Delta t}\omega} \delta u_i\, {}^{t+\Delta t}\rho\, {}^{t+\Delta t}_{t+\Delta t}b_i\, \mathrm{d}^{t+\Delta t}\omega + \int_{^{t+\Delta t}\gamma_t} \delta u_i\, {}^{t+\Delta t}_{t+\Delta t}t_i\, \mathrm{d}^{t+\Delta t}\gamma - \int_{^{t+\Delta t}\omega} \delta u_i\, {}^{t+\Delta t}\rho \ddot{u}_i\, \mathrm{d}^{t+\Delta t}\omega \tag{3.27}$$

The left superscript indicates the time at which the variable is measured. The left subscript indicates the time to which the variable is referenced. Cauchy-Stress σ_{ij} are always referred to the configuration they occur, so the subscript is omitted. It is assumed that the information at time 0, Δt, $2\Delta t$, ..., t is available. However, the variables at time $t + \Delta t$ are unknown and it is necessary to relate them to available variables. The deformation gradient is introduced in large-deformation analysis and plays the role to relate variables in different configurations.

$${}^{t}_{0}\mathbf{F} = \frac{\partial {}^{t}x_i}{\partial {}^{0}x_i} = \begin{bmatrix} \dfrac{\partial {}^{t}x_1}{\partial {}^{0}x_1} & \dfrac{\partial {}^{t}x_1}{\partial {}^{0}x_2} & \dfrac{\partial {}^{t}x_1}{\partial {}^{0}x_3} \\ \dfrac{\partial {}^{t}x_2}{\partial {}^{0}x_1} & \dfrac{\partial {}^{t}x_2}{\partial {}^{0}x_2} & \dfrac{\partial {}^{t}x_2}{\partial {}^{0}x_3} \\ \dfrac{\partial {}^{t}x_3}{\partial {}^{0}x_1} & \dfrac{\partial {}^{t}x_3}{\partial {}^{0}x_2} & \dfrac{\partial {}^{t}x_3}{\partial {}^{0}x_3} \end{bmatrix} \tag{3.28}$$

It is very similar to the concept of Jacobian matrix, or transformation matrix as discussed in Eq. (3.21) which relates physical and natural coordinates. Here the deformation gradient is used to relate variables in configuration at time 0 and t. Appropriate stress and strain measures are also introduced to continue the analysis. The second Piola-Kirchhoff stress measured at time t and

reference to the initial configuration time 0 is given as (Bathe, 1996):

$$
\begin{aligned}
{}^{t}_{0}\mathbf{S} &= J\,{}^{0}_{t}\mathbf{F}\,{}^{t}\boldsymbol{\sigma}\,{}^{0}_{t}\mathbf{F} \\
J\,{}^{t}\boldsymbol{\sigma} &= {}^{t}_{0}\mathbf{F}\,{}^{t}_{0}\mathbf{S}\,{}^{t}_{0}\mathbf{F}
\end{aligned}
\tag{3.29}
$$

In component form:

$$
\begin{aligned}
{}^{t}_{0}S_{mn} &= J\,{}^{0}_{t}F_{mi}\,{}^{t}\sigma_{ij}\,{}^{0}_{t}F_{nj} \\
J\,{}^{t}\sigma_{ij} &= {}^{t}_{0}F_{im}\,{}^{t}_{0}S_{mn}\,{}^{t}_{0}F_{jn}
\end{aligned}
\tag{3.30}
$$

J is the determinant of the deformation gradient matrix. While Cauchy Stress is a true stress measured in the deformed configuration, Piola-Kirchhoff stress is a virtual stress that can be referenced to other known configurations. While Cauchy Stress physically represents the stress that loads in the deformed configuration acting on the deformed area, second Piola-Kirchhoff stress equals to the load mapped into another configuration of interest acting on the area of that configuration.

The Cauchy infinitesimal strain ε_{ij} under small-deformation assumption contains all linear terms:

$$
\begin{aligned}
\varepsilon_{xx} &= \frac{\partial u}{\partial x} \\
\varepsilon_{zz} &= \frac{\partial w}{\partial z} \\
\varepsilon_{xz} &= \frac{1}{2}\gamma_{xz} = \frac{1}{2}\left(\frac{\partial u}{\partial z} + \frac{\partial w}{\partial x}\right)
\end{aligned}
\tag{3.31}
$$

However, when an object is under large deformation and rotation, the Green-Lagrangian strain tensor E_{ij} is used to count in the geometrically non-linear deformation:

$$
E_{ij} = \frac{1}{2}\left(\frac{\partial u_i}{\partial x_j} + \frac{\partial u_j}{\partial x_i} + \frac{\partial u_k}{\partial x_i}\frac{\partial u_k}{\partial x_j}\right) \tag{3.32}
$$

Or in detail form:

$$
\begin{aligned}
E_{xx} &= \frac{\partial u}{\partial x} + \frac{1}{2}\left(\left(\frac{\partial u}{\partial x}\right)^2 + \left(\frac{\partial w}{\partial x}\right)^2\right) \\
E_{zz} &= \frac{\partial w}{\partial z} + \frac{1}{2}\left(\left(\frac{\partial u}{\partial z}\right)^2 + \left(\frac{\partial w}{\partial z}\right)^2\right) \\
E_{xz} &= \frac{1}{2}\left(\frac{\partial u}{\partial z} + \frac{\partial w}{\partial x} + \frac{\partial u}{\partial x}\frac{\partial u}{\partial z} + \frac{\partial w}{\partial x}\frac{\partial w}{\partial z}\right)
\end{aligned}
\tag{3.33}
$$

Non-linear terms are included in Eq. (3.33) by comparison with Eq. (3.31). It can be proved (see Bathe (1996)) that:

$$
{}^{\mathrm{t}}_{0}\delta E_{mn} = {}^{\mathrm{t}}_{0}F_{im}\, {}_{\mathrm{t}}\delta\varepsilon_{ij}\, {}^{\mathrm{t}}_{0}F_{jn} \tag{3.34}
$$

With Eq. (3.30) and Eq. (3.34), it is found that between two configuration at time t_1 and t_2, the following relationship can be established (Bathe, 1996):

$$
\begin{aligned}
\int_{{}^{\mathrm{t}_1}\omega} \delta_{\mathrm{t}_1}\varepsilon_{ij}\, {}^{\mathrm{t}_1}\sigma_{ij}\, \mathrm{d}^{\mathrm{t}_1}\omega &= \int_{{}^{\mathrm{t}_1}\omega} \left({}^{\mathrm{t}_2}_{\mathrm{t}_1}F_{mi}\, \delta^{\mathrm{t}_1}_{\mathrm{t}_2}E_{mn}\, {}^{\mathrm{t}_2}_{\mathrm{t}_1}F_{nj}\right)\left(\frac{1}{J}\, {}^{\mathrm{t}_1}_{\mathrm{t}_2}F_{ip}\, {}^{\mathrm{t}_1}_{\mathrm{t}_2}S_{pq}\, {}^{\mathrm{t}_1}_{\mathrm{t}_2}F_{jq}\right)\mathrm{d}^{\mathrm{t}_1}\omega \\
&= \int_{{}^{\mathrm{t}_1}\omega} \frac{1}{J}\, \underbrace{\delta_{mp}\,\delta_{nq}}_{\text{Kronecker delta}}\, \delta^{\mathrm{t}_1}_{\mathrm{t}_2}E_{mn}\, {}^{\mathrm{t}_1}_{\mathrm{t}_2}S_{pq}\, \mathrm{d}^{\mathrm{t}_1}\omega \\
&= \int_{{}^{\mathrm{t}_2}\omega} \delta^{\mathrm{t}_1}_{\mathrm{t}_2}E_{ij}\, {}^{\mathrm{t}_1}_{\mathrm{t}_2}S_{ij}\, \mathrm{d}^{\mathrm{t}_2}\omega
\end{aligned}
\tag{3.35}
$$

When dealing with finite-deformation FEM, there are two Lagrangian approaches. The first one is the so-called Total Lagrangian (T.L.) formulation in which all variables are referenced to the initial/undeformed/reference configuration at time 0. The second one is the Updated Lagrangian (U.L.) formulation where all variables are referenced to the current/deformed configuration at time t. Considering Eq. (3.35), the governing equation Eq. (3.27) of finite-deformation FEM for T.L. and U.L. formulation are (Bathe, 1996; Zienkiewics and Taylor, 2005):

$$
\int_{{}^{\mathrm{t}+\Delta\mathrm{t}}\omega} \delta_{\mathrm{t}+\Delta\mathrm{t}}\varepsilon_{ij}\, {}^{\mathrm{t}+\Delta\mathrm{t}}\sigma_{ij}\, \mathrm{d}^{\mathrm{t}+\Delta\mathrm{t}}\omega = \int_{{}^{0}\omega} \delta^{\mathrm{t}+\Delta\mathrm{t}}_{0}E_{ij}\, {}^{\mathrm{t}+\Delta\mathrm{t}}_{0}S_{ij}\, \mathrm{d}^{0}\omega = \mathbf{R}.\mathbf{H}.\mathbf{S}. \tag{3.36}
$$

$$
\int_{{}^{\mathrm{t}+\Delta\mathrm{t}}\omega} \delta_{\mathrm{t}+\Delta\mathrm{t}}\varepsilon_{ij}\, {}^{\mathrm{t}+\Delta\mathrm{t}}\sigma_{ij}\, \mathrm{d}^{\mathrm{t}+\Delta\mathrm{t}}\omega = \int_{{}^{\mathrm{t}}\omega} \delta^{\mathrm{t}+\Delta\mathrm{t}}_{\mathrm{t}}E_{ij}\, {}^{\mathrm{t}+\Delta\mathrm{t}}_{\mathrm{t}}S_{ij}\, \mathrm{d}^{\mathrm{t}}\omega = \mathbf{R}.\mathbf{H}.\mathbf{S}. \tag{3.37}
$$

Equation (3.36) is the governing equation referenced to the initial/undeformed/reference configu-

ration values, while Eq. (3.37) is the governing equation referenced to the current/deformed configuration values. Due to its relative convenience when formulating the element stiffness matrix, the Updated Lagrangian formulation was chosen for the problem at hands and will be discussed further in this work. Interested readers are referred to Chapter 6 of Bathe (1996) for detail formulation of T.L. formulation. Equations (3.36) and (3.37) should be numerically identical (Bathe, 1996; Bathe et al., 1975).

Following Eq. (3.37), the stress and strain can be further decomposed into (Bathe, 1996; Bathe et al., 1975):

$$ {}^{t+\Delta t}_{t}S_{ij} = {}^{t}_{t}S_{ij} + {}_{t}S_{ij} = {}^{t}\sigma_{ij} + {}_{t}S_{ij} \tag{3.38} $$

$$ {}^{t+\Delta t}_{t}E_{ij} = \underbrace{\frac{1}{2}\left(\frac{\partial u_i}{\partial {}^{t}x_j} + \frac{\partial u_j}{\partial {}^{t}x_i}\right)}_{\varepsilon_{ij}} + \underbrace{\frac{1}{2}\left(\frac{\partial u_k}{\partial {}^{t}x_i}\frac{\partial u_k}{\partial {}^{t}x_j}\right)}_{\eta_{ij}} \tag{3.39} $$

Together with the approximations that:

$$ {}_{t}S_{ij} \approx {}_{t}C_{ijkl}\,{}_{t}\varepsilon_{kl} \tag{3.40} $$

and:

$$ \delta_{t}E_{ij} \approx \delta_{t}\varepsilon_{ij} \tag{3.41} $$

For a control volume, it is assumed that there is no transfer of mass across the boundary so that the elemental mass is independent of time:

$$ {}^{t+\Delta t}\rho\, \mathrm{d}^{t+\Delta t}\omega = {}^{0}\rho\, \mathrm{d}^{0}\omega = {}^{t}\rho\, \mathrm{d}^{t}\omega = \rho\, \mathrm{d}\omega \tag{3.42} $$

The governing equation of finite-deformation FEM in U.L. (Eq. (3.37)) formulation boils down

to (Bathe, 1996):

$$\begin{aligned}&\int_{{}^{t}\omega} \delta_{t}\varepsilon_{ij}\, {}_{t}C_{ijkl}\, {}_{t}\varepsilon_{kl}\, \mathrm{d}^{t}\omega + \int_{{}^{t}\omega} \delta_{t}\eta_{ij}\, {}^{t}\sigma_{ij}\, \mathrm{d}^{t}\omega + \int_{{}^{t}\omega} \delta_{t}\varepsilon_{ij}\, {}^{t}\sigma_{ij}\, \mathrm{d}^{t}\omega \\ &= \int_{{}^{t+\Delta t}\omega} \delta u_i\, {}^{t+\Delta t}\rho\, {}^{t+\Delta t}_{t+\Delta t}b_i\, \mathrm{d}^{t+\Delta t}\omega + \int_{{}^{t+\Delta t}\gamma_t} \delta u_i\, {}^{t+\Delta t}_{t+\Delta t}t_i\, \mathrm{d}^{t+\Delta t}\gamma - \int_{\omega} \delta u_i \rho \ddot{u}_i\, \mathrm{d}\omega\end{aligned} \tag{3.43}$$

Again the shape function is introduced to approximate the unknown displacements and displacement variation as in Eq. (3.13). Applying the principle of virtual work, the matrix form of the governing equation can be derived (Bathe, 1996):

$$\mathbf{M}\ddot{\mathbf{u}} + ({}^{t}_{t}\mathbf{K}_M + {}^{t}_{t}\mathbf{K}_G)\mathbf{u} = {}^{t+\Delta t}\mathbf{R} - {}^{t}_{t}\mathbf{F} \tag{3.44}$$

$$\mathbf{M} = \int_{\omega} \mathbf{N}^T \rho\, \mathbf{N}\, \mathrm{d}\omega \tag{3.45}$$

$${}^{t}_{t}\mathbf{K}_M = \int_{{}^{t}\omega} {}^{t}_{t}\mathbf{B}_L^T\, {}^{t}\mathbf{C}\, {}^{t}_{t}\mathbf{B}_L\, \mathrm{d}^{t}\omega \tag{3.46}$$

$${}^{t}_{t}\mathbf{K}_G = \int_{{}^{t}\omega} {}^{t}_{t}\mathbf{B}_{NL}^T\, {}^{t}\boldsymbol{\sigma}\, {}^{t}_{t}\mathbf{B}_{NL}\, \mathrm{d}^{t}\omega \tag{3.47}$$

$${}^{t}_{t}\mathbf{F} = \int_{{}^{t}\omega} {}^{t}_{t}\mathbf{B}_L^T\, {}^{t}\bar{\boldsymbol{\sigma}}\, \mathrm{d}^{t}\omega \tag{3.48}$$

$\mathbf{M}$ Time-independent mass matrix

$\mathbf{K}_M$ Material stiffness matrix

$\mathbf{K}_G$ Geometric stiffness matrix

$\mathbf{F}$ Nodal point forces vector

$\mathbf{R}$ Body force, boundary traction and external force

$\mathbf{C}$ Elastic moduli matrix

$\boldsymbol{\sigma}$ Element Cauchy Stress matrix

$\bar{\boldsymbol{\sigma}}$ Element Cauchy Stress vector

${}_t^t\mathbf{B}_L$ and ${}_t^t\mathbf{B}_{NL}$ are linear and non-linear strain-displacement matrix, respectively. In U.L. formulation, the terms in ${}_t^t\mathbf{B}_L$ and ${}_t^t\mathbf{B}_{NL}$ are similar to linear strain-displacement matrix:

$$ {}_t^t\mathbf{B}_L = \begin{bmatrix} \frac{\partial N_1}{\partial {}^t\mathrm{x}} & 0 & \frac{\partial N_2}{\partial {}^t\mathrm{x}} & 0 & \frac{\partial N_3}{\partial {}^t\mathrm{x}} & 0 & \frac{\partial N_4}{\partial {}^t\mathrm{x}} & 0 \\ 0 & \frac{\partial N_1}{\partial {}^t\mathrm{z}} & 0 & \frac{\partial N_2}{\partial {}^t\mathrm{z}} & 0 & \frac{\partial N_3}{\partial {}^t\mathrm{z}} & 0 & \frac{\partial N_4}{\partial {}^t\mathrm{z}} \\ \frac{\partial N_1}{\partial {}^t\mathrm{z}} & \frac{\partial N_1}{\partial {}^t\mathrm{x}} & \frac{\partial N_2}{\partial {}^t\mathrm{z}} & \frac{\partial N_2}{\partial {}^t\mathrm{x}} & \frac{\partial N_3}{\partial {}^t\mathrm{z}} & \frac{\partial N_3}{\partial {}^t\mathrm{x}} & \frac{\partial N_4}{\partial {}^t\mathrm{z}} & \frac{\partial N_4}{\partial {}^t\mathrm{x}} \end{bmatrix} \tag{3.49} $$

$$ {}_t^t\mathbf{B}_{NL} = \begin{bmatrix} \frac{\partial N_1}{\partial {}^t\mathrm{x}} & 0 & \frac{\partial N_2}{\partial {}^t\mathrm{x}} & 0 & \frac{\partial N_3}{\partial {}^t\mathrm{x}} & 0 & \frac{\partial N_4}{\partial {}^t\mathrm{x}} & 0 \\ \frac{\partial N_1}{\partial {}^t\mathrm{z}} & 0 & \frac{\partial N_2}{\partial {}^t\mathrm{z}} & 0 & \frac{\partial N_3}{\partial {}^t\mathrm{z}} & 0 & \frac{\partial N_4}{\partial {}^t\mathrm{z}} & 0 \\ 0 & \frac{\partial N_1}{\partial {}^t\mathrm{x}} & 0 & \frac{\partial N_2}{\partial {}^t\mathrm{x}} & 0 & \frac{\partial N_3}{\partial {}^t\mathrm{x}} & 0 & \frac{\partial N_4}{\partial {}^t\mathrm{x}} \\ 0 & \frac{\partial N_1}{\partial {}^t\mathrm{z}} & 0 & \frac{\partial N_2}{\partial {}^t\mathrm{z}} & 0 & \frac{\partial N_3}{\partial {}^t\mathrm{z}} & 0 & \frac{\partial N_4}{\partial {}^t\mathrm{z}} \end{bmatrix} \tag{3.50} $$

According to Eq. (3.24) in the isoparametric formulation, the spatial derivatives of the shape

function in physical coordinates are:

$$\begin{bmatrix} \frac{\partial N_1}{\partial {}^{t}x} & \frac{\partial N_2}{\partial {}^{t}x} & \frac{\partial N_3}{\partial {}^{t}x} & \frac{\partial N_4}{\partial {}^{t}x} \\ \frac{\partial N_1}{\partial {}^{t}z} & \frac{\partial N_2}{\partial {}^{t}z} & \frac{\partial N_3}{\partial {}^{t}z} & \frac{\partial N_4}{\partial {}^{t}z} \end{bmatrix} = \begin{bmatrix} \Gamma_{11} & \Gamma_{12} \\ \Gamma_{21} & \Gamma_{22} \end{bmatrix} \begin{bmatrix} \frac{\partial N_1}{\partial \xi} & \frac{\partial N_2}{\partial \xi} & \frac{\partial N_3}{\partial \xi} & \frac{\partial N_4}{\partial \xi} \\ \frac{\partial N_1}{\partial \eta} & \frac{\partial N_2}{\partial \eta} & \frac{\partial N_3}{\partial \eta} & \frac{\partial N_4}{\partial \eta} \end{bmatrix} \tag{3.51}$$

These terms are used to populate ${}^{t}_{t}\mathbf{B}_L$ and ${}^{t}_{t}\mathbf{B}_{NL}$. ${}^{t}\mathbf{C}$ is the matrix of elastic moduli in the current configuration and will be further discussed in Section 3.5 and Section 3.6.

${}^{t}\boldsymbol{\sigma}$ is the Cauchy Stress matrix and ${}^{t}\bar{\boldsymbol{\sigma}}$ is the Cauchy Stress vector (Bathe, 1996; Bathe et al., 1975):

$${}^{t}\boldsymbol{\sigma} = \begin{bmatrix} {}^{t}\sigma_{11} & {}^{t}\sigma_{12} & 0 & 0 \\ {}^{t}\sigma_{21} & {}^{t}\sigma_{22} & 0 & 0 \\ 0 & 0 & {}^{t}\sigma_{11} & {}^{t}\sigma_{12} \\ 0 & 0 & {}^{t}\sigma_{21} & {}^{t}\sigma_{22} \end{bmatrix} \tag{3.52}$$

$${}^{t}\bar{\boldsymbol{\sigma}} = \begin{bmatrix} {}^{t}\sigma_{11} \\ {}^{t}\sigma_{22} \\ {}^{t}\sigma_{12} \end{bmatrix} \tag{3.53}$$

${}^{t}\sigma_{ij}$ is calculated by:

$${}^{t}\sigma_{ij} = {}^{t}C_{ijkl}\,{}^{t}\varepsilon_{kl} \tag{3.54}$$

Here ${}^{t}\varepsilon_{ij}$ is the Almansi strain tensor computed using:

$${}^{t}\varepsilon_{ij} = \frac{1}{2}\left(\delta_{ij} - {}^{t}_{0}b^{-1}_{ij}\right) \tag{3.55}$$

${}^{t}_{0}b_{ij}$ is the left Cauchy-Green deformation tensor expressed as:

$${}^{t}_{0}b_{ij} = {}^{t}_{0}F_{ik}\,{}^{t}_{0}F_{jk} = {}^{t}_{0}\mathbf{F}\,{}^{t}_{0}\mathbf{F}^{T} \tag{3.56}$$

The integration of Eqs. (3.46) and (3.47) in an isoparametric formulation will first be mapped into natural coordinates through the transformation:

$$\int_{{}^{t}\omega} f(x,z)\,\mathrm{d}^{t}\omega = \iint_{{}^{t}\omega} f({}^{t}\mathrm{x},{}^{t}\mathrm{z})\,\mathrm{d}^{t}\mathrm{x}\,\mathrm{d}^{t}\mathrm{z} = \int_{-1}^{1}\int_{-1}^{1} f(\xi,\eta)\;\mathrm{d}\xi\,\mathrm{d}\eta \tag{3.57}$$

Define $J^{\mathbf{PN}}$ as the determinant of the Jacobian matrix relating physical and natural coordinates:

$$J^{\mathbf{PN}} = \mathrm{Det}\left(\mathbf{J}^{\mathbf{PN}}\right) = \begin{vmatrix} \dfrac{\partial^{t}\mathrm{x}}{\partial\xi} & \dfrac{\partial^{t}\mathrm{z}}{\partial\xi} \\ \dfrac{\partial^{t}\mathrm{x}}{\partial\eta} & \dfrac{\partial^{t}\mathrm{z}}{\partial\eta} \end{vmatrix} \tag{3.58}$$

$J^{\mathbf{PN}}$ is physically interpreted as the area ratio of the elemental area between physical and natural coordinates with $\mathrm{d}^{t}\omega = J^{\mathbf{PN}}\,\mathrm{d}\xi\,\mathrm{d}\eta$, so $f(x,z) = J^{\mathbf{PN}}\,f(\xi,\eta)$. Since the analytical expression of $f({}^{t}x,{}^{t}z)$ or $f(\xi,\eta)$ is usually unavailable, numerical integration is alternatively used. For the bi-linear quadrilateral elements, Gaussian quadrature is implemented for numerical integration of the matrix. The basic idea of a quadrature rule is to approximate an integral function into weighted sum of a function. Here two Gaussian points are distributed along each direction (Bathe, 1996; Zienkiewics and Taylor, 2005):

$$\int_{-1}^{1}\int_{-1}^{1} f(\xi,\eta)\;\mathrm{d}\xi\,\mathrm{d}\eta = \sum_{i=1}^{2}\sum_{j=1}^{2} W_i W_j f(\xi_i,\eta_j) \tag{3.59}$$

W_i is weight factors and ξ_i is Gaussian point location. With order of 2 in each dimension, it can be found that $W_i = 1$ and $\xi_i = \pm 1/\sqrt{3}$.

Using the Gaussian quadrature, each element stiffness matrix can be formed and then the global stiffness matrix including non-linear effects is assembled. The unknown displacements is calculated using appropriate solver.

3.5 Plane Stress and Plane Strain Problems

In two special cases, when the third dimension is either comparatively small or larger than the other two dimensions, the three-dimensional problems can be simplified into two-dimensional problems. The first case is called a plane stress problem and the later one called a plane strain problem. Recall that for an isotropic, linear-elastic material, given Young's modulus and Poisson ratio, the complete stress-strain relationship ignoring thermal effects is (Zienkiewics and Taylor, 2005):

$$\begin{bmatrix} \varepsilon_{xx} \\ \varepsilon_{yy} \\ \varepsilon_{zz} \\ 2\varepsilon_{yz} \\ 2\varepsilon_{xz} \\ 2\varepsilon_{xy} \end{bmatrix} = \frac{1}{E} \begin{bmatrix} 1 & -\nu & -\nu & 0 & 0 & 0 \\ -\nu & 1 & -\nu & 0 & 0 & 0 \\ -\nu & -\nu & 1 & 0 & 0 & 0 \\ 0 & 0 & 0 & 2(1+\nu) & 0 & 0 \\ 0 & 0 & 0 & 0 & 2(1+\nu) & 0 \\ 0 & 0 & 0 & 0 & 0 & 2(1+\nu) \end{bmatrix} \begin{bmatrix} \sigma_{xx} \\ \sigma_{yy} \\ \sigma_{zz} \\ \sigma_{yz} \\ \sigma_{xz} \\ \sigma_{xy} \end{bmatrix} \tag{3.60}$$

$$\begin{bmatrix} \sigma_{xx} \\ \sigma_{yy} \\ \sigma_{zz} \\ \sigma_{yz} \\ \sigma_{xz} \\ \sigma_{xy} \end{bmatrix} = \frac{E}{(1+\nu)(1-2\nu)} \begin{bmatrix} 1-\nu & \nu & \nu & 0 & 0 & 0 \\ \nu & 1-\nu & \nu & 0 & 0 & 0 \\ \nu & \nu & 1-\nu & 0 & 0 & 0 \\ 0 & 0 & 0 & \frac{(1-2\nu)}{2} & 0 & 0 \\ 0 & 0 & 0 & 0 & \frac{(1-2\nu)}{2} & 0 \\ 0 & 0 & 0 & 0 & 0 & \frac{(1-2\nu)}{2} \end{bmatrix} \begin{bmatrix} \varepsilon_{xx} \\ \varepsilon_{yy} \\ \varepsilon_{zz} \\ 2\varepsilon_{yz} \\ 2\varepsilon_{xz} \\ 2\varepsilon_{xy} \end{bmatrix} \tag{3.61}$$

In a plane stress problems, taking y as the out-of-plane dimension, the assumptions $\sigma_{xy} = \sigma_{yz} = \sigma_{yy} = 0$ are made and the simplified stress-strain relations is matrix is (Zienkiewics and Taylor,

2005):

$$\begin{bmatrix} \sigma_{xx} \\ \sigma_{zz} \\ \sigma_{xz} \end{bmatrix} = \frac{E}{1-\nu^2} \begin{bmatrix} 1 & \nu & 0 \\ \nu & 1 & 0 \\ 0 & 0 & \frac{1-\nu}{2} \end{bmatrix} \begin{bmatrix} \varepsilon_{xx} \\ \varepsilon_{zz} \\ 2\varepsilon_{xz} \end{bmatrix} \tag{3.62}$$

With elastic moduli:

$$\mathbf{C}_{\text{plane stress}} = \frac{E}{1-\nu^2} \begin{bmatrix} 1 & \nu & 0 \\ \nu & 1 & 0 \\ 0 & 0 & \frac{1-\nu}{2} \end{bmatrix} \tag{3.63}$$

and the deformation gradient becomes (Zienkiewics and Taylor, 2005):

$${}^{\mathrm{t}}_{0}\mathbf{F} = \begin{bmatrix} \frac{\partial^{\mathrm{t}} x_1}{\partial^0 x_1} & \frac{\partial^{\mathrm{t}} x_1}{\partial^0 x_2} & 0 \\ \frac{\partial^{\mathrm{t}} x_2}{\partial^0 x_1} & \frac{\partial^{\mathrm{t}} x_2}{\partial^0 x_2} & 0 \\ 0 & 0 & \frac{\partial^{\mathrm{t}} x_3}{\partial^0 x_3} \end{bmatrix} \tag{3.64}$$

In a plane strain problem, it is assumed that $\varepsilon_{xy} = \varepsilon_{yz} = \varepsilon_{yy} = 0$ and the resulting elastic moduli is (Zienkiewics and Taylor, 2005):

$$\mathbf{C}_{\text{plane strain}} = \frac{E}{(1+\nu)(1-2\nu)} \begin{bmatrix} 1-\nu & \nu & 0 \\ \nu & 1-\nu & 0 \\ 0 & 0 & \frac{1-2\nu}{2} \end{bmatrix} \tag{3.65}$$

and the deformation gradient reduced to:

$${}^{\mathrm{t}}_{0}\mathbf{F} = \begin{bmatrix} \frac{\partial^{\mathrm{t}} x_1}{\partial^0 x_1} & \frac{\partial^{\mathrm{t}} x_1}{\partial^0 x_2} & 0 \\ \frac{\partial^{\mathrm{t}} x_2}{\partial^0 x_1} & \frac{\partial^{\mathrm{t}} x_2}{\partial^0 x_2} & 0 \\ 0 & 0 & 1 \end{bmatrix} \tag{3.66}$$

For linear elasticity problem, arrange the terms in Eq. (3.63) and Eq.(3.65) with correct order to form the elastic moduli ${}^{0}\mathbf{C}$.

3.6 Material Constitutive Relations

For structural model within the scope of linear elasticity, the material constitutive relation is:

$$ {}^{t}\boldsymbol{\sigma} = {}^{t}\mathbf{C}\,{}^{t}\boldsymbol{\varepsilon} \tag{3.67} $$

However, some materials like rubber display non-linear stress-strain relations under large deformation and the linear constitutive relation is insufficient to reveal the nonlinearity. It is also found that the consideration of the non-linear material constitutive relation is critical for one of the validation test so the theory of the hyperelasticity will be presented here. In the case of hyperelasticity, the stress will be calculated by introducing a strain energy model (Bathe, 1996; Cook, 1974; Zienkiewics and Taylor, 2005):

$$ {}^{t}_{0}S_{ij} = \frac{\partial W}{\partial\, {}^{t}_{0}E_{ij}} \tag{3.68} $$

With ${}^{t}_{0}S_{ij}$ is the 2nd Piola-Kirchhoff Stress, W the strain energy model and ${}^{t}_{0}E_{ij}$ the Cauchy-Lagrangian strain. A Mooney-Rivlin strain energy model is used after a trade-off between numerical accuracy and computational time (Bathe, 1996; Sussman and Bathe, 1987):

$$ {}^{t}_{0}W = C_1({}^{t}_{0}I_1 - 3) + C_1({}^{t}_{0}I_2 - 3) + W_H({}^{t}_{0}I_3) \tag{3.69} $$

C_1, C_2 and W_H are material constants. For isotropic materials W depends on the three invariants of the deformations defined as (Bathe, 1996):

$$\begin{aligned} {}^{\mathrm{t}}_{0}I_1 &= {}^{\mathrm{t}}_{0}C_{kk} \\ {}^{\mathrm{t}}_{0}I_2 &= \frac{1}{2}\left[\left({}^{\mathrm{t}}_{0}I_1\right)^2 - {}^{\mathrm{t}}_{0}C_{ij}\,{}^{\mathrm{t}}_{0}C_{ji}\right] \\ {}^{\mathrm{t}}_{0}I_3 &= \det {}^{\mathrm{t}}_{0}C_{ij} \end{aligned} \tag{3.70}$$

Here ${}^{\mathrm{t}}_{0}C_{ij}$ is the right Cauchy-Green deformation tensor defined as:

$${}^{\mathrm{t}}_{0}C_{ij} = {}^{\mathrm{t}}_{0}F_{ki}\,{}^{\mathrm{t}}_{0}F_{kj} = {}^{\mathrm{t}}_{0}\mathbf{F}^T\,{}^{\mathrm{t}}_{0}\mathbf{F} \tag{3.71}$$

It can be proved that $\delta\,{}^{\mathrm{t}}_{0}E_{ij} = \frac{1}{2}\delta\,{}^{\mathrm{t}}_{0}C_{ij}$ (Bathe, 1996; Zienkiewics and Taylor, 2005). The second Piola-Kirchhoff stress is then expressed as:

$${}^{\mathrm{t}}_{0}S_{ij} = 2\left(\frac{\partial\,{}^{\mathrm{t}}_{0}W}{\partial\,{}^{\mathrm{t}}_{0}I_1}\frac{\partial\,{}^{\mathrm{t}}_{0}I_1}{\partial\,{}^{\mathrm{t}}_{0}C_{ij}} + \frac{\partial\,{}^{\mathrm{t}}_{0}W}{\partial\,{}^{\mathrm{t}}_{0}I_2}\frac{\partial\,{}^{\mathrm{t}}_{0}I_2}{\partial\,{}^{\mathrm{t}}_{0}C_{ij}} + \frac{\partial\,{}^{\mathrm{t}}_{0}W}{\partial\,{}^{\mathrm{t}}_{0}I_3}\frac{\partial\,{}^{\mathrm{t}}_{0}I_3}{\partial\,{}^{\mathrm{t}}_{0}C_{ij}}\right) \tag{3.72}$$

And the elastic moduli in the initial/undeformed/reference configuration is related by:

$${}^{0}C_{ijkl} = \frac{\partial\,{}^{\mathrm{t}}_{0}S_{ij}}{\partial\,{}^{\mathrm{t}}_{0}E_{ij}} \tag{3.73}$$

Due to the use of U.L. formulation, the variables in the reference configuration needs to be transformed into the current configuration. The stress and the elastic moduli are two essential terms to make up the stiffness matrix in Eq. (3.46) and Eq. (3.47). The elastic moduli in both configurations is related by the deformation gradient (Bathe et al., 1975; Zienkiewics and Taylor, 2005):

$$J\,{}^{\mathrm{t}}C_{mnpq} = {}^{\mathrm{t}}_{0}F_{mi}\,{}^{\mathrm{t}}_{0}F_{nj}\,{}^{\mathrm{t}}_{0}F_{pk}\,{}^{\mathrm{t}}_{0}F_{ql}\,{}^{0}C_{ijkl} \tag{3.74}$$

The detail form of this model can be found in the Appendix of Sussman and Bathe (1987).

3.7 Solution of Static and Dynamic Problems

3.7.1 Newton-Raphson Method

For static problem, e.g., to find out the deformation of a statically loaded structure, the governing equations Eq. (3.44) ignoring inertial effects is expressed as:

$$(\mathbf{K}_M + \mathbf{K}_G)\,\mathbf{U} = \mathbf{K}_T\mathbf{U} = \mathbf{R} - \mathbf{F} \tag{3.75}$$

For small-deformation FEM under constant load, the stiffness matrix is assumed to be constant and the resulting displacement is derived by simply inverting the stiffness matrix. The non-linearities can come from geometry such as large rotation of the structure, the material constitutive relation for hyperelastic materials, or external load tangential to the end of a deformed structure. Each of the aforementioned non-linearities cause the stiffness to change with deformation and can not be solved in closed form. For the problem at hand, a Newton-Raphson method is chosen as the non-linear solves due to rapid converge. Taking $\mathbf{U}^0$ as the initial value, $\mathrm{d}\mathbf{U}^i$ as the incremental displacement at the ith-iteration, $\mathbf{U}^i$ is the total displacement at the ith-iteration and $\Psi^i = \mathbf{R}^i - \mathbf{F}^i$ (Zienkiewics and Taylor, 2005):

$$\mathrm{d}\mathbf{U}^i = \left(\mathbf{K}_T^i\right)^{-1} \Psi^i \tag{3.76}$$

$$\mathbf{U}^i = \mathbf{U}^0 + \sum_{k=1}^{i} \mathrm{d}\mathbf{U}^k \tag{3.77}$$

If the residue $\| \Psi^i \|$ is larger than the preset tolerance, the method continues to iterate until convergence is achieved.

3.7.2 Newmark Method

Transient problems will be investigated later and a time integration scheme is necessary. The time integration scheme chosen for the FEM analysis was the Newmark method (Newmark, 1959) based

on Eq. (3.78) and Eq. (3.79):

$$\dot{\mathbf{x}}_{t+\Delta t} = \dot{\mathbf{x}}_t + (1-\gamma)\ddot{\mathbf{x}}_t \Delta t + \gamma \ddot{\mathbf{x}}_{t+\Delta t} \Delta t \tag{3.78}$$

$$\mathbf{x}_{t+\Delta t} = \mathbf{x}_t + \dot{\mathbf{x}}_t \Delta t + \left(\frac{1}{2} - \beta\right)\ddot{\mathbf{x}}_t \Delta t^2 + \beta \ddot{\mathbf{x}}_{t+\Delta t} \Delta t^2 \tag{3.79}$$

$$\gamma \geqslant \frac{1}{2},\ \beta \geqslant \frac{1}{4}\left(\gamma + \frac{1}{2}\right)^2 \tag{3.80}$$

where γ and β are weighting values controlling implicity in the time integration. Equation (3.80) is the Von-Neumann stability criteria.

The equation of motion for structure is:

$$\mathbf{M}\ddot{\mathbf{x}}_{t+\Delta t} + \mathbf{C}\dot{\mathbf{x}}_{t+\Delta t} + \mathbf{K}\mathbf{x}_{t+\Delta t} = \mathbf{F}_{t+\Delta t} \tag{3.81}$$

Expressing $\dot{\mathbf{x}}_{t+\Delta t}$ and $\ddot{\mathbf{x}}_{t+\Delta t}$ in terms of known parameters and $\mathbf{x}_{t+\Delta t}$ given from Eq. (3.78) and Eq. (3.79) we can write (Zienkiewics and Taylor, 2005):

$$\ddot{\mathbf{x}}_{t+\Delta t} = \frac{1}{\beta \Delta t^2}\left(\mathbf{x}_{t+\Delta t} - \mathbf{x}_t\right) - \frac{\dot{\mathbf{x}}_t}{\beta \Delta t} - \left(\frac{1}{2\beta} - 1\right)\ddot{\mathbf{x}}_t \tag{3.82}$$

$$\dot{\mathbf{x}}_{t+\Delta t} = \frac{\gamma}{\beta \Delta t}\left(\mathbf{x}_{t+\Delta t} - \mathbf{x}_t\right) + \left(1 - \frac{\gamma}{\beta}\right)\dot{\mathbf{x}}_t + \left(1 - \frac{\gamma}{2\beta}\right)\Delta t \ddot{\mathbf{x}}_t \tag{3.83}$$

Substituting Eq. (3.82) and Eq. (3.83) into Eq. (3.81) we get:

$$\hat{\mathbf{K}}\mathbf{x}_{t+\Delta t} = \hat{\mathbf{F}}_{t+\Delta t} \tag{3.84}$$

where $\hat{\mathbf{K}}$ is the effective stiffness matrix (Zienkiewics and Taylor, 2005):

$$\hat{\mathbf{K}} = \mathbf{K} + \frac{1}{\beta \Delta t}\mathbf{M} + \frac{\gamma}{\beta \Delta t}\mathbf{C} \tag{3.85}$$

and a is the effective loading vector (Zienkiewics and Taylor, 2005):

$$\hat{\mathbf{F}}_{t+\Delta t} = \mathbf{F}_{t+\Delta t} + \left[\frac{1}{\beta\Delta t^2}\mathbf{x}_t + \frac{1}{\beta\Delta t}\dot{\mathbf{x}}_t + \left(\frac{1}{2\beta} - 1\right)\ddot{\mathbf{x}}_t\right]\mathbf{M} + \left[\frac{\gamma}{\beta\Delta t}\mathbf{x}_t + \left(\frac{\gamma}{\beta} - 1\right)\dot{\mathbf{x}}_t + \left(\frac{\gamma}{2\beta} - 1\right)\Delta t\ddot{\mathbf{x}}_t\right]\mathbf{C} \quad (3.86)$$

The integration parameters γ and β are primarily chosen to guarantee numerical stability. However, a large value of γ can introduce numerical damping which may adversely affect results. Typical values of γ range between 0.5 and 1.0 (Zienkiewics and Taylor, 2005). It was found that in an extreme case, low values of γ require an unacceptably small time step to maintain numerical stability. For a given structural CFL number which controls the time step of the computation, increasing γ tends to stabilize the computation, but also introduces numerical damping. For example, while a case in which $\gamma = 0.5$ may result in numerical instability, for that same case, a value of $\gamma = 1.0$ may yield a stable result. However excessively large γ may also introduce numerical damping and a phase difference in response. As a trade-off, $\gamma = 0.6$ and $\beta = 0.3025$ are used in the following sections.

3.8 Computational Procedure for Structural Dynamics

The complete procedure summarizing the isoparametric formulation and Updated Lagrangian perspective for finite-deformation FEM is summarized below for the purpose of understanding and to assist in implementation:

1. At initial step, create the mesh for the structure and assemble the time-invariant global mass matrix as in Eq. (3.45).

2. For each new time step, first calculate the updated external boundary forces ${}^{\mathrm{t}}_{\mathrm{t}}\mathbf{R}$.

3. Loop over each element at integration points ξ_i and η_j. Calculate local derivative $\dfrac{\partial N_a}{\partial \xi}$ and $\dfrac{\partial N_a}{\partial \eta}$ and Jacobian matrix $\mathbf{J}^{\mathbf{PN}}$. Invert $\mathbf{J}^{\mathbf{PN}}$ to get $\mathbf{\Gamma}^{\mathbf{PN}}$ and global derivative $\dfrac{\partial N_a}{\partial {}^{\mathrm{t}}x}$ and $\dfrac{\partial N_a}{\partial {}^{\mathrm{t}}y}$.

Then the linear and non-linear strain-displacement matrix ${}^{t}_{t}\mathbf{B}_L$ and ${}^{t}_{t}\mathbf{B}_{NL}$ in Eq. (3.49) and Eq. (3.50) can be obtained.

4. Calculate the deformation gradient ${}^{t}_{0}\mathbf{F}$ and then the elastic moduli according to Eq. (3.74).

5. Assemble ${}^{t}_{t}\mathbf{K}_M$, ${}^{t}_{t}\mathbf{K}_G$, and ${}^{t}_{t}\mathbf{F}$ based on numerical quadrature.

6. Use the Newmark method and compute the unknown incremental displacement for this time step.

3.9 Verification of FEM Model

3.9.1 2D Plate with End Shear Load

A classical structural problem is investigated to verify the FEM code developed according to the finite-deformation FEM discussed in this chapter. A cantilevered plate is subjected to load at its free end. The theoretical result with the small-deformation assumption is given in Timoshenko and Goodier (1970):

$$\begin{aligned} u &= -\frac{Px^2y}{2EI} - \frac{\nu Py^3}{6EI} + \frac{Py^3}{6IG} + \left(\frac{Pl^2}{2EI} - \frac{Pc^2}{2IG}\right)y \\ v &= \frac{\nu Pxy^2}{2EI} + \frac{Px^3}{6EI} - \frac{Pl^2x}{2EI} + \frac{Pl^3}{3EI} \end{aligned} \tag{3.87}$$

where P is the end shear at the tip of cantilever, c=10 the half width of the beam, L=100 the length of the beam, $E = 1000$ the Young's modulus, ν=0.25 the Poisson ratio. A comparison of theoretical and numerical results are shown in Fig. 3.2 with increasing loads. The FEM model agrees well with the theoretical result for small deformation but converges to different solutions at large deformation. This is because the theoretical result is based on the small-deformation theory. For large-deformation problems, commercial FEM software Abaqus is used to be compared with the FEM model in Fig. 3.3. Although Abaqus results give saw-tooth shape at the end due to convergence criteria, It is found that the FEM results agree well with the results of Abaqus for at

large deformation. It has also been demonstrated during the development of the code that both U.L. and T.L. formulation converges to the same result. The FEM solver developed in this chapter also serves as a stepping stone for later validation of fluid-structure-interaction problems.

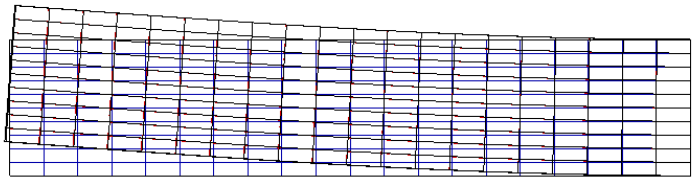

3.2.1 P=10N

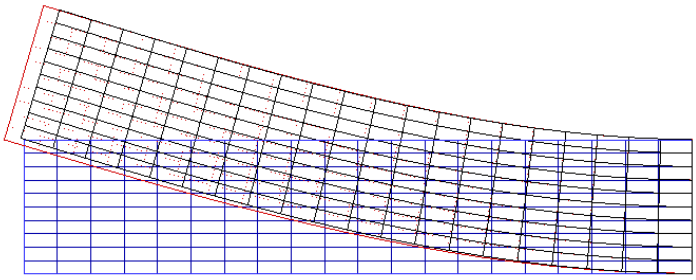

3.2.2 P=40N

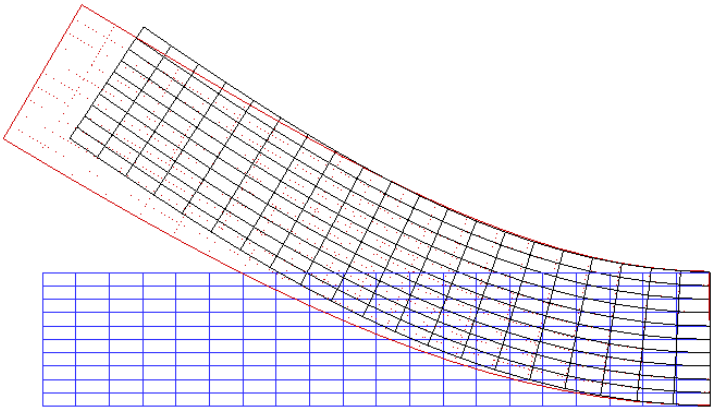

3.2.3 P=80N

Figure 3.2: Comparison of structure deformation between theoretical and finite-deformation FEM for 2D plate under end shear load. (Blue: initial position. Red: theoretical result. Black: numerical result.)

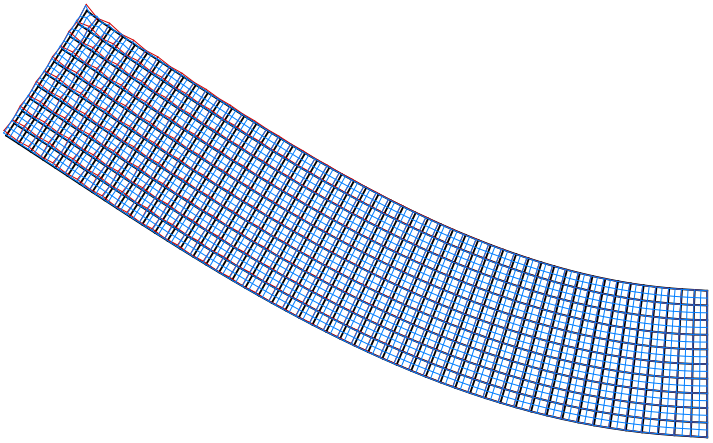

3.3.1 P=100N

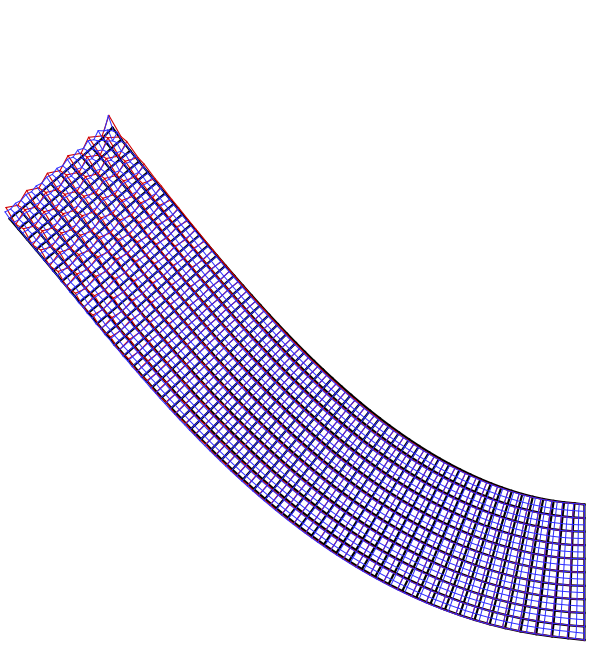

3.3.2 P=200N

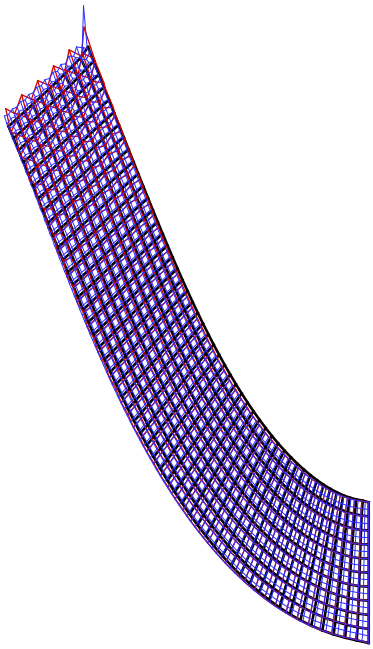

3.3.3 P=300N

Figure 3.3: Comparison of structure deformation between commercial FEM software Abaqus and finite-deformation FEM for 2D plate under end load. (Black: Finite-deformation FEM(51x11), Red: Abaqus(51x11), Blue: Abaqus(101x21))

3.10 Conclusion

A finite-deformation FEM model based on the principle of virtual work is analyzed and utilized for the structure dynamics portion of this work. This model considers the non-linear deformation of the structure and non-linear constitutive relation of the material. In Chapter 4 and Chapter 5, it is coupled with Smoothed Particle Hydrodynamics to solve fluid-structure-interaction problems. This displacement-based FEM model follows a general theory and the results obtained show excellent agreement with theoretical and commercial software results. This model can also incorporate plasticity, three dimensional models, etc as the complexity of future problems increases.

Chapter 4

Validation of SPH-FEM Model for Fluid-Structure Interaction

4.1 Introduction

This chapter combines the SPH and FEM theory described in the previous chapters and proposes a SPH-FEM for solving fluid-structure interaction problems. Validation tests are performed to assess the capability of the SPH-FEM model for the investigation of free-surface flow interacting with deformable structures. The validation results show good agreement with the published experimental result in Antoci et al. (2007) and Souto-Iglesias et al. (2008). A mesh dependency study is included to demonstrate the variation and convergence of results with different spatial and temporal discretizations.

4.2 Principle of SPH-FEM Modeling

The motivation for proposing the SPH-FEM model is to obtain the established structural modeling of FEM while maintaining the advantages of SPH for free surface flows. To illustrate the numerical

configuration of the SPH-FEM model, Fig. 4.1 is a detail of the clamped edge of the flexible gate used for the validation case described in detail in Section 4.4. SPH particles are denoted with dots simulating the fluid domain in the right hand side of the figure. The grid on the left hand side denotes the FEM mesh for the structural domain. Rectangular blocks show rigid boundary particles using a Monaghan repulsive force (Gómez-Gesteira et al., 2010; Monaghan and Kos, 1999; Rogers and Dalrymple, 2008). The triangular symbols are interface particles transmitting the interaction forces.

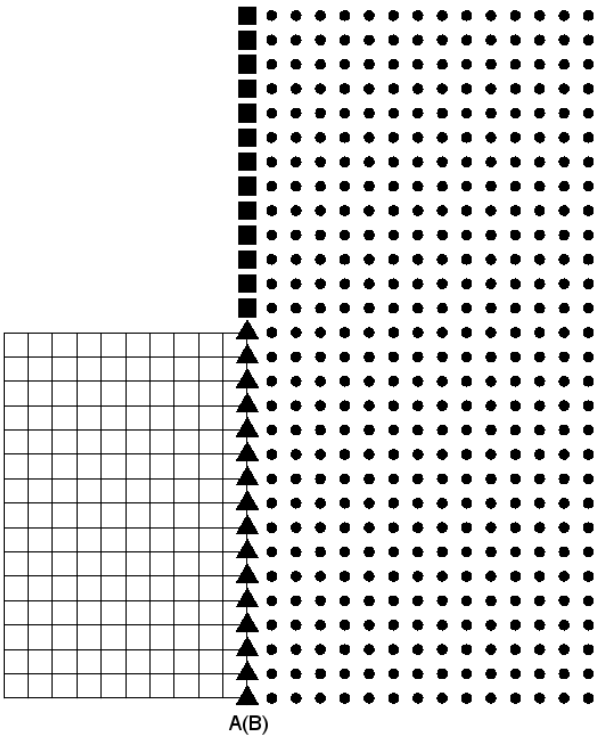

Figure 4.1: Configuration of SPH-FEM model (• Fluid particles. ▲ Interface particles. ■ Boundary particles. FEM Mesh: Structural domain.)

The detailed process of coupling is listed as below and a flow chart summarizing the process is illustrated in Fig. 4.2:

1. At the beginning of each time step, the positions of interface particles are determined from the positions of the exterior layer of FEM nodes. (e.g. In Fig. 4.1, interface particle A is collocated with FEM node B.)

2. Determine the neighboring fluid particles for interface particle A.

3. Exert a repulsive force from A to its neighboring fluid particles and sum the forces from structure to fluid as $\vec{F}_{StF}$.

4. Use SPH to update fluid particle properties.

5. Apply equal and opposite reaction force, $\vec{F}_{StF}$, from fluid to structure $\vec{F}_{FtS} = -\vec{F}_{StF}$ for particle A.

6. Force $\vec{F}_{FtS}$ is transmitted into the external force term for FEM node B.

7. Repeat steps 2 – 6 to find $\vec{F}_{FtS}$ for all fluid structure interface particles, and then transmit the force to corresponding FEM nodes.

8. Apply FEM governing equations to update the deformable structure under the fluid force.

9. Advance to next iteration.

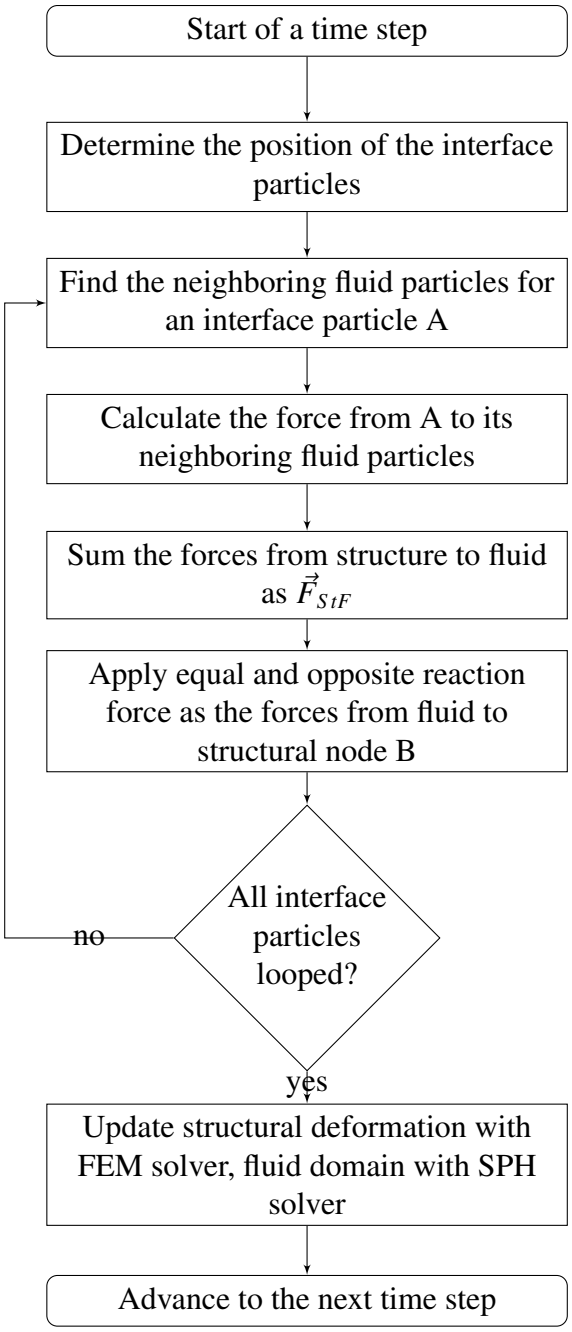

Figure 4.2: Flow chart showing the coupling procedure of the SPH-FEM model.

4.3 Flow in Sloshing Tank Interaction with an Elastic Body

4.3.1 Simulation Setup

The first validation test for SPH-FEM model is to simulate the flow in a sloshing tank interacting with an elastic body as compared with Souto-Iglesias et al. (2008). The initial configuration is illustrated in Fig. 4.3. The sloshing tank bounds are enforced by Monaghan type boundary particles. SPH fluid particles are distributed uniformly to a finite depth. The fluid used is vegetable oil with a viscosity fifty times that of water (Souto-Iglesias et al., 2008). A sinusoidal oscillation is prescribed to the tank. A flexible boundary is represented by a FEM mesh located at the center bottom of the tank with a height equal to the vegetable oil depth. The simulation parameters for this validation case are listed in Table 4.1:

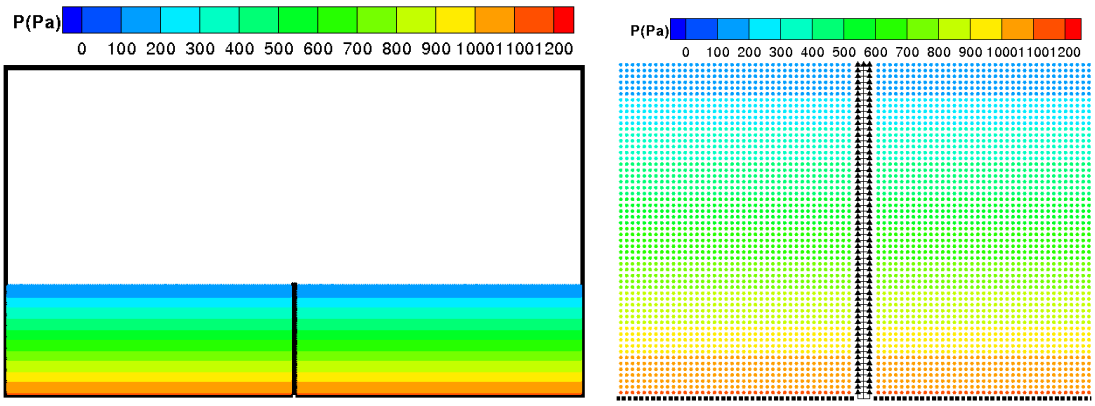

Figure 4.3: Initial configuration of SPH-FEM model for flow in sloshing tank interaction with an elastic body. (Left) Whole picture of simulation setup, with fluid particles colored by pressure. (Right) Close-up view of the configuration of SPH-FEM model including SPH fluid particles, interface particles, boundary particles and FEM mesh.

Table 4.1: Simulation parameters. (Geometry is per Souto-Iglesias et al. (2008).)

Parameters	
Tank height	344.5(mm)
Tank width	609(mm)
Water height	115(mm)
Water width	609(mm)
Fluid spacing	1(mm)
Boundary spacing	0.5(mm)
Elastic body height	115(mm)
Elastic body width	4(mm)
FEM node spacing	2(mm)
dt	1.3E-5(s)
Oscillation period	1.21(s)
No. of structural FEM nodes	174
No. of interface particles	115
No. of fluid particles	16986
No. of boundary particles	949

4.3.2 Simulation and Validation Results

The experimental results for this validation test may be found in both Souto-Iglesias et al. (2008) and Botia-Vera et al. (2010). The same experiment was conducted with the later paper publishing a longer time history of the results. A clamped elastic beam in a mid-depth oil case is validated with the SPH-FEM model. The available physical variables for validation are the local displacement of the tip of the elastic body and four photographs taken during the experiment to illustrate the deformation of the elastic body and free surface. The origin of the local coordinates is taken at the connection point between the elastic body and sloshing tank. The local X axis is aligned with the bottom of the tank and the local Z axis is aligned with the initial position of the elastic body. Figure 4.4 shows the time history of the local X displacement at the tip of the elastic body. Figure 4.5 gives a close-up look of the dynamics of the elastic body in the SPH-FEM model. Figure 4.6 shows a comparison of the simulation results with the photographs from the experimental results of Souto-Iglesias et al. (2008).

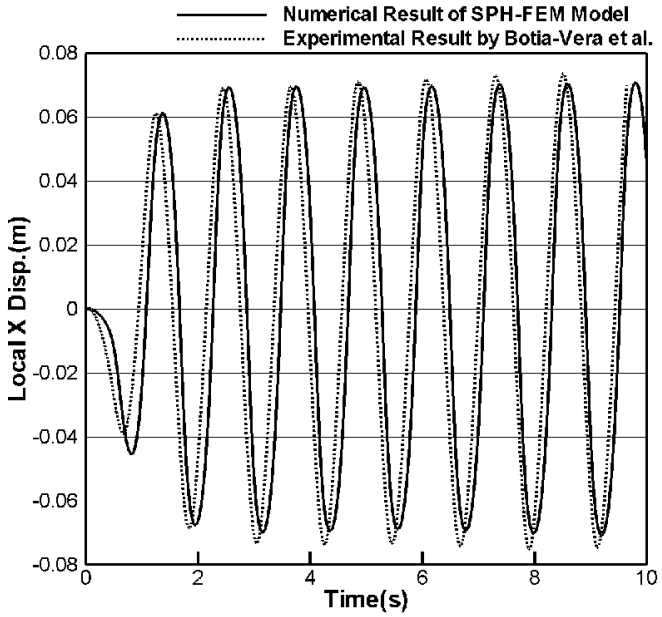

Figure 4.4: Comparison of local X displacement at the tip of the elastic body. (Solid) Numerical results from SPH-FEM simulation. (Dashed) Experimental results from Botia-Vera et al. (2010).

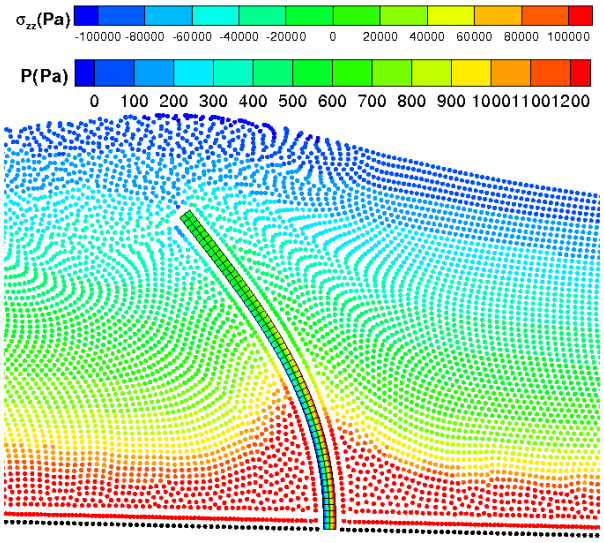

Figure 4.5: Close-up look of dynamics of elastic body at t = 2.12s. FEM mesh colored by σ_{zz}.

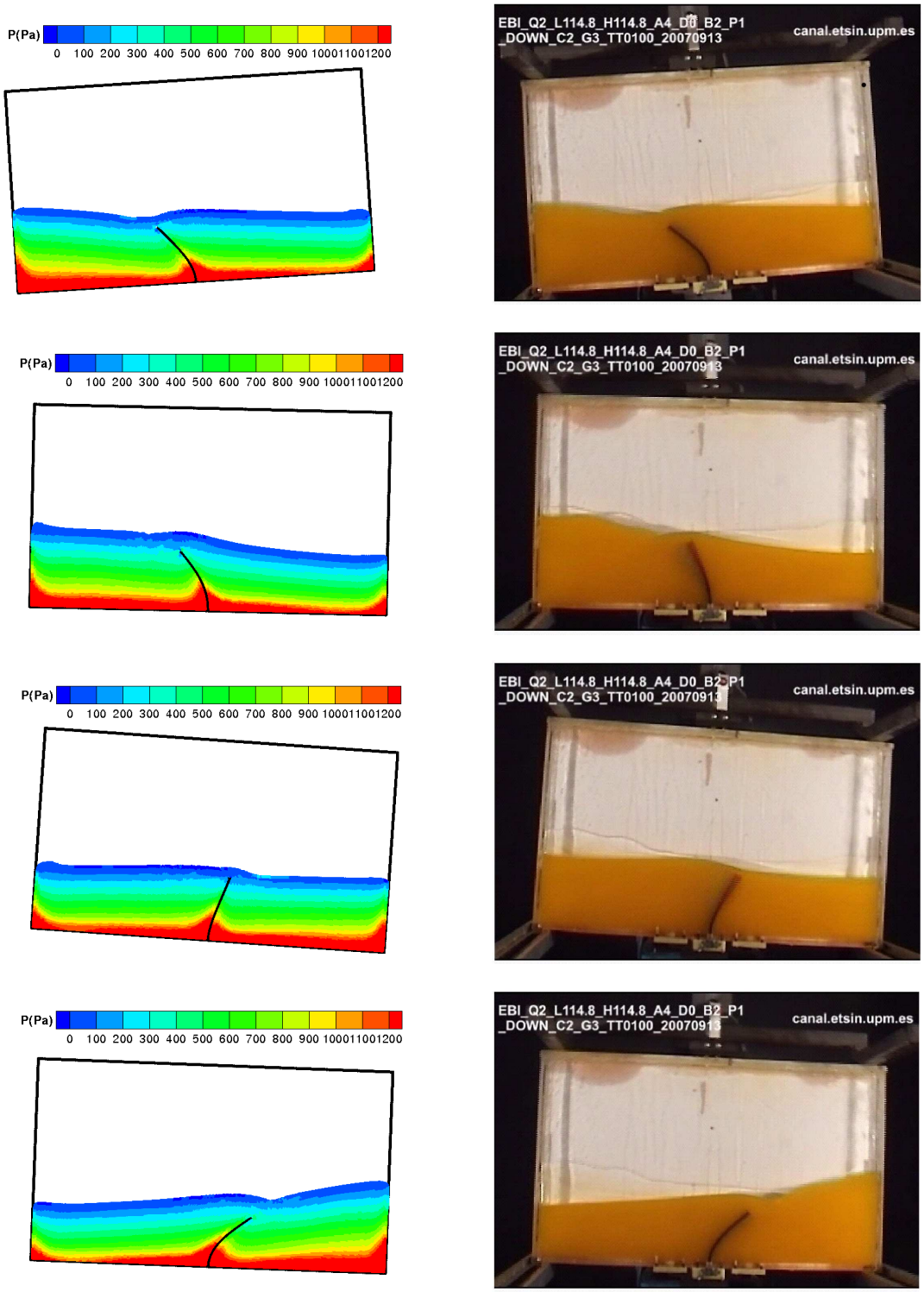

Figure 4.6: Comparison of numerical and experimental results (Souto-Iglesias et al., 2008) for time = 1.84, 2.12, 2.32, 2.56s consecutively. Water particles are colored by pressure (Pa).

4.3.3 Discussion of Results

Before embarking on large-deformation FEM model, a tentative test is conducted to couple SPH with a small-deformation FEM model. It is found that the amplitude and period shows fair agreement with the work of Souto-Iglesias et al. (2008). But the saw-tooth-shape curve of deflection indicates linear relationship between strain and force which necessitates the large-deformation FEM model. After implementing this SPH coupling with large-deformation FEM model, Figure 4.4 shows good agreement with the experimental results of Souto-Iglesias et al. (2008). However, it is noted that there is a phase difference starting from the beginning and remaining through the simulation. Souto-Iglesias et al. (2008) state that the input curve is not purely sinusoidal at the start of the experiment. Purely sinusoidal motion requires large angular velocity at the beginning which is not practical in the experiment. This results in a small ramp starting from zero at the beginning of the prescribed motion later transitioning to sinusoidal motion. The input curve is reproduced given in Souto-Iglesias et al. (2008). The phase difference may then be due to reproduction of this initial ramp. Additionally, the boundary condition/boundary deficiency may be a contributor to the observed phase difference. Clumping is visible in Fig. 4.5 in the fluid domain near the fluid-structure interface and the sloshing tank boundary. In general, the displacement curve shows periodic motion with respect to the sloshing tank as in the experiment. The good agreement in the amplitude of the displacement indicates that the SPH-FEM model can accurately transmit fluid-structure interaction forces. Figure 4.6 shows that the SPH-FEM model accurately captures the profile of the free surface of the fluid and the deflection of the structure. For time=1.84, 2.12 and 2.56s, the positions of the wave trough and crest show good match between the simulation and the experiment. For time=2.32s, the free surfaces matches with experimental result while the structural deformation shows a phase lag behind the experiment.

4.4 Dam-break Flow through an Elastic Gate

4.4.1 Simulation Setup

Another validation case using the SPH-FEM model is performed via comparison with results obtained by Antoci et al. (2007) for a dam-break flow of water through an elastic gate case. The initial configuration is illustrated in Fig. 4.7. SPH fluid particles are distributed uniformly to a finite depth throughout the right half of the domain. A vertical FEM mesh acts as an elastic gate. Two types of boundary condition are investigated. The first option is a virtual boundary condition for right and bottom boundaries. In the virtual boundary condition, if a fluid particle crosses a virtual boundary its velocity is inverted in the direction along the boundary normal. In the second method, Monaghan boundary particles are located along the fluid-wall interface. Both cases uses Monaghan boundary particles for the interface particles of the elastic gate. The results using these two boundary conditions are plotted in Fig. 4.9. In this case, structural damping is assumed negligible compared to inertial forces. The simulation parameters for this validation case are listed in Table 4.2.

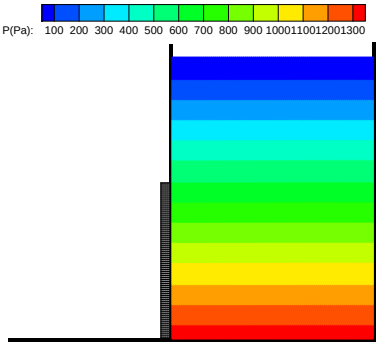

Figure 4.7: Initial configuration of dam-break through elastic gate case.

Table 4.2: Simulation parameters. (Geometry is per Antoci et al. (2007).)

Water height	0.14(m)
Water width	0.1(m)
Gate length	0.079(m)
Gate thickness	0.005(m)
Reynolds number	1.31E5
Fluid spacing	0.001(m)
Rubber spacing	0.001(m)
Rubber density	1100(kg/m^3)
No. of structural FEM nodes	480
No. of interface particles	85
No. of fluid particles	14000
No. of boundary particles	717
dt	4.15E-6(s)
Simulation time	0–0.4(s)
CPU	Serial 3.3 GHz
Computer time used	69(h)

4.4.2 Simulation and Validation Results

Results obtained using a linear elasticity constitutive relation yield only fair agreement with experimental data as in Fig. 4.9. Using the Mooney-Rivlin model to reproduce the nonlinear stress-strain curve for the material as described in Antoci (2006) yields better agreement with the experimental results as shown in Fig. 4.8. The comparison of different constitutive relations and boundary conditions is illustrated in Fig. 4.9. Figures 4.10–4.12 show fluid and gate properties at the time of maximum gate deflection (t=0.15s). Figure 4.10 shows fluid density and gate lateral stress σ_{xx}. Figure 4.11 shows fluid pressure and gate axial stress σ_{zz}. Figure 4.12 shows total velocity of fluid and gate shear stress τ_{xz}. Figure 4.13 shows fluid pressures and gate stresses σ_{zz} over the entire simulation.

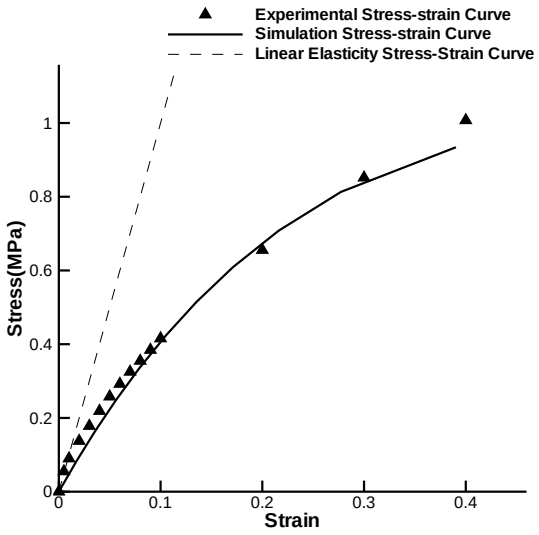

Figure 4.8: Comparison of stress-strain curve of linear elasticity, Mooney-Rivlin model (Sussman and Bathe, 1987) and tensile test (Antoci, 2006).

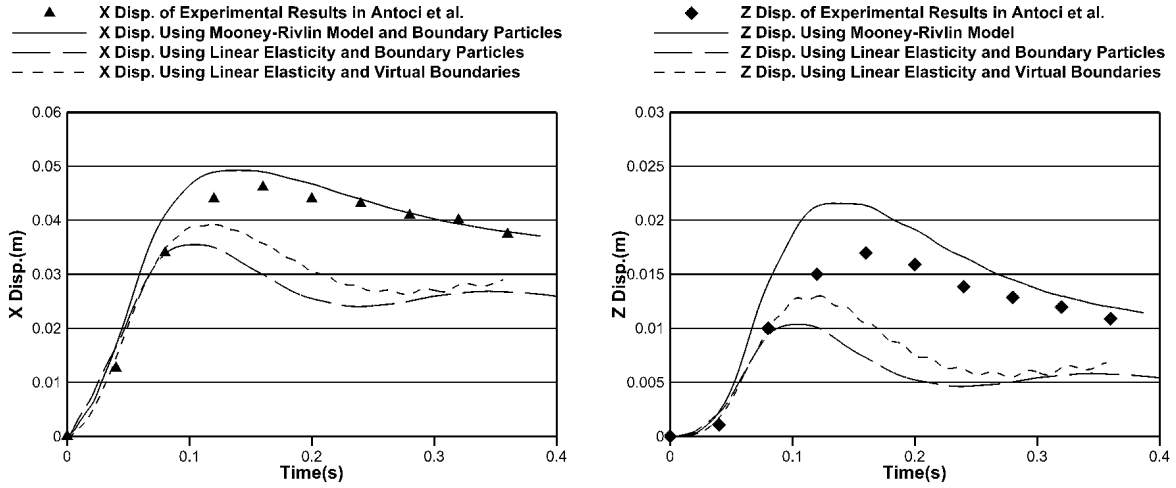

Figure 4.9: Comparison of displacement at the midpoint of gate tip between simulation and experimental results (Antoci et al., 2007) using spacing for FS and ES specified in Table 4.2. (Left) Horizontal displacement. (Right) Vertical displacement.

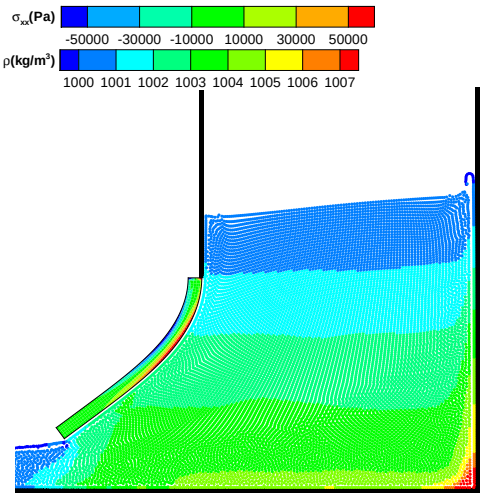

Figure 4.10: Plot of SPH-FEM model at t=0.15s with water particles colored by density ρ and FEM nodes colored by lateral stress σ_{xx}.

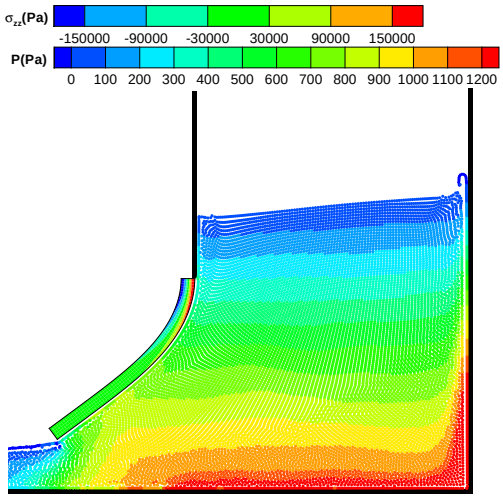

Figure 4.11: Plot of SPH-FEM model at t=0.15s with water particles colored by pressure P and FEM nodes colored by axial stress σ_{zz}.

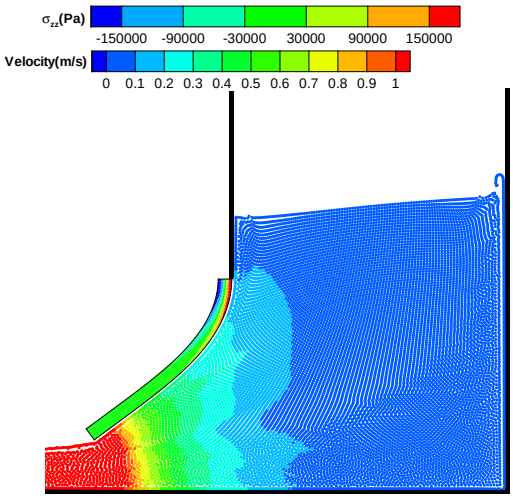

Figure 4.12: Plot of SPH-FEM model at t=0.15s with water particles colored by total velocity V and FEM nodes colored by shear stress τ_{xz}.

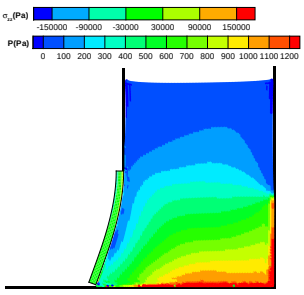

4.13.1 t=0.04s

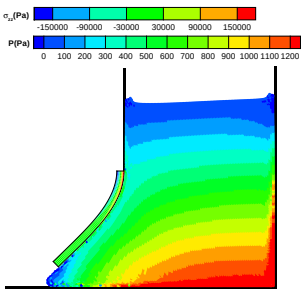

4.13.2 t=0.08s

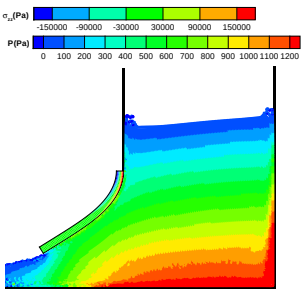

4.13.3 t=0.12s

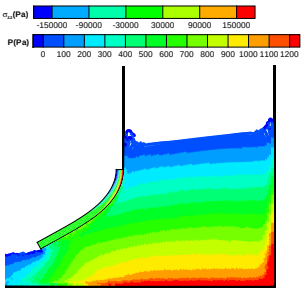

4.13.4 t=0.16s

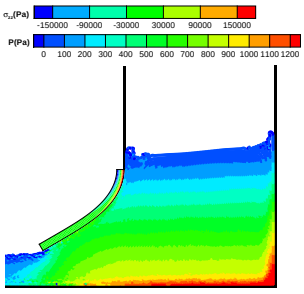

4.13.5 t=0.20s

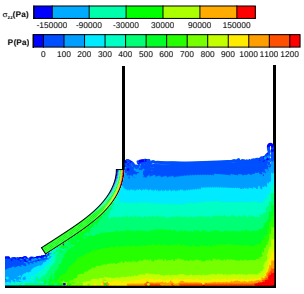

4.13.6 t=0.24s

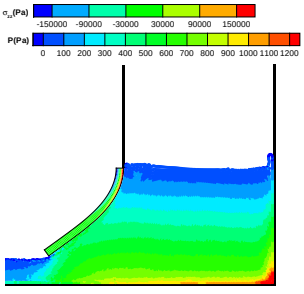

4.13.7 t=0.28s

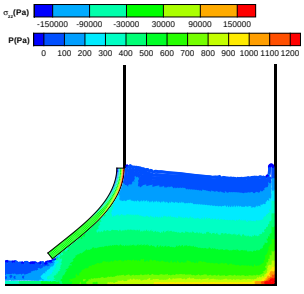

4.13.8 t=0.32s

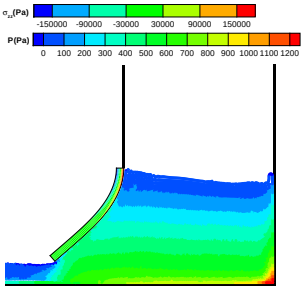

4.13.9 t=0.36s

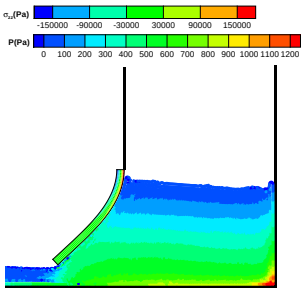

4.13.10 t=0.40s

Figure 4.13: Simulation results for every 0.04s. Water particles colored by pressure and structure FEM nodes by σ_{zz}.

4.4.3 Discussion of Results

The effects of the non-linear constitutive relation can be seen in Fig. 4.9. The model using linear elasticity under-predicts the displacements for both virtual boundaries and Monaghan boundaries and predicts an earlier occurrence of maximum displacement. Better agreement with experimental results is achieved after applying the Mooney-Rivlin hyperelasticity model. This can be explained from an energy perspective. Assuming an equal fluid-structure energy transfer, the stiffer linear elasticity constitutive equation will result in a lower total tip displacement for the same internal strain energy.

Numerical results obtained by Antoci et al. (2007) also exhibited over-prediction of the displacement. Antoci theorized that water leaking at the side of the gate caused a pressure drop in the fluid, which is not captured in either of the numerical simulations. Comparing the different boundary conditions, it can be observed that the displacement oscillation is a result of the presence of virtual boundaries. This is due to the large pressure oscillation originating from the right and bottom boundaries and propagating throughout the fluid domain. Although Monaghan boundary particles are sufficient to prevent boundary penetration and largely reduce the pressure oscillation, an acceleration deficiency is still present which may contribute to the non-physical shape by fluid particles near boundaries in Figures 4.10 – 4.12.

In general, the agreement of displacements with experimental results indicates accurate force transmission between SPH and FEM models. Figure 4.10 shows desirable less than 1% of density fluctuations which satisfies the WCSPH assumption. When compared to results by Antoci et al. (2007), the interested reader can note that the structural stresses σ_{xx} and τ_{xz} agree well, although σ_{zz} is somewhat lower than experimental results. From Fig. 4.13, the advantage of accessing the information such as density, pressure, velocity, internal stress of both fluid and structural models in the time domain utilizing a SPH-FEM model is revealed.

4.5 Mesh Dependency and Convergence Study

In addition to the good agreement with the experimental results for the SPH-FEM model, a mesh dependency/convergence study is conducted to examine how the results vary with the change of SPH particle spacing, FEM mesh spacing and time step. The following analysis is based on the case of dam-break flow through an elastic gate in Section 4.4.

In this high Reynolds number flow, the Courant-Friedrichs-Lewy (CFL) condition which is related to the convective part of the flow is the major limitation for time step. As defined in Chapter 2, the time step for fluid is $\mathrm{dt}_{fluid-CFL} = \mathrm{CFL}\frac{\Delta_{fluid}}{Cs_0}$ and the for structure is $\mathrm{dt}_{struc-CFL} = \mathrm{CFL}\frac{\Delta_{rubber}}{\sqrt{E_{YM}/\rho}}$ in which CFL is the CFL number with value usually less than 1. The time step is determined by the smaller value of $\mathrm{dt}_{fluid-CFL}$ or $\mathrm{dt}_{struc-CFL}$. Since the term $\sqrt{E_{YM}/\rho}$ is usually chosen much larger than Cs_0, the structure part normally limits the time step.

The results shown in Section 4.4 are with RS(rubber spacing) of 0.001 m and FS(fluid spacing) of 0.001 m. More cases are run to show the convergence and performance of this SPH-FEM model with RS of 0.0025 m, FS of 0.0025, 0.005 and 0.01 m and CFL of 1, 0.5, 0.25, 0.1 and 0.005.

Figure 4.14 to Figure 4.17 show the effect of the time step at different geometric spacings. Figure 4.14 to Figure 4.16 are results with RS=0.0025 m. In Fig. 4.14 and Fig. 4.15, it is observed that the change of the time step did not have a significant change on the results and the results are convergent. In Fig. 4.16, although the curve with largest time step (1.04E-5) has a slight difference with the other two curves, the results still converged closely with the refinement of the time step. Figure 4.17 summarizes all results with RS=0.001 m. It is found that the time step has less impact on the results than the effect of refinement of fluid spacing. The results with the same geometric configurations converged with the refinement of time steps. Less cases are completed when RS=0.001 than RS=0.0025 since a large CFL number (0.5 or 1) tends to cause particle clumping and instability in SPH and a smaller CFL number requires excessive computation time (on the order of weeks for a single simulation case).

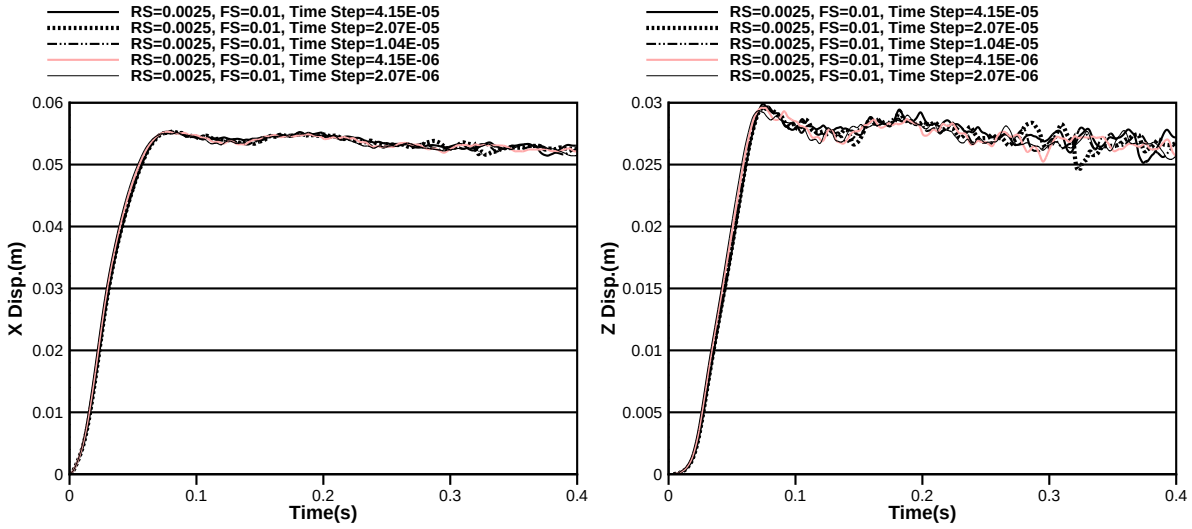

Figure 4.14: Plot of time history for the displacements at the tip of the gate with RS=0.0025 and FS=0.01 at five different time steps. (Left) X displacements. (Right) Z displacements.

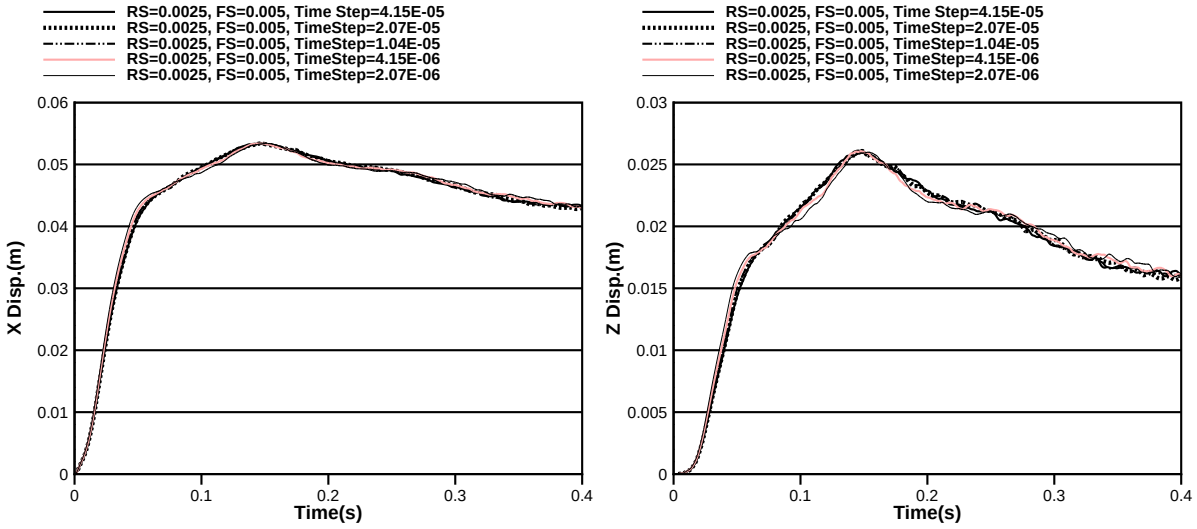

Figure 4.15: Plot of time history for the displacements at the tip of the gate with RS=0.0025 and FS=0.005 at five different time steps. (Left) X displacements. (Right) Z displacements.

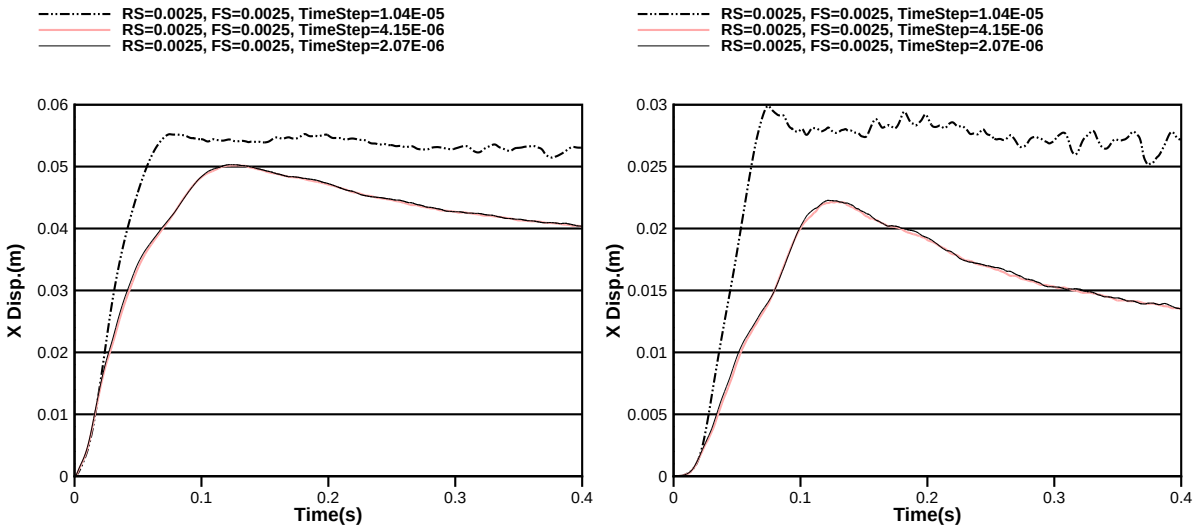

Figure 4.16: Plot of time history for the displacements at the tip of the gate with RS=0.0025 and FS=0.0025 at five different time steps. (Left) X displacements. (Right) Z displacements.

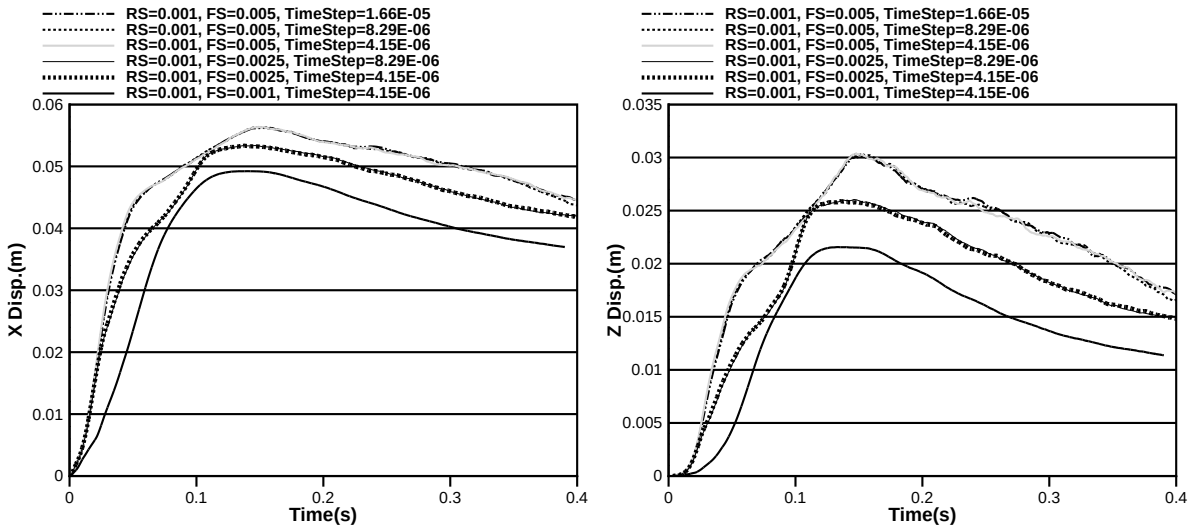

Figure 4.17: Plot of time history for the displacements at the tip of the gate with RS=0.001 and different FS and Time Steps. (Left) X Displacements. (Right) Z Displacements.

In addition to the effect of the temporal discretization, the effect of spatial discretization is also plotted in Fig. 4.18. Figure 4.18 summarized all the cases with the same time step = 4.15E-6 second. This time step is chosen since the results reach the convergent solution as seen from Fig. 4.14 to Fig. 4.17. It can be seen that with the refinement of the SPH particles or FEM mesh, the curves become smoother which indicate smoother transmission of the fluid-structure interaction forces. The refinement of the SPH discretization for both RS=0.0025 and RS=0.001 can improve

the results to better agreement with the experiment. But the refinement of FEM mesh tends to increase the amplitude of displacements.

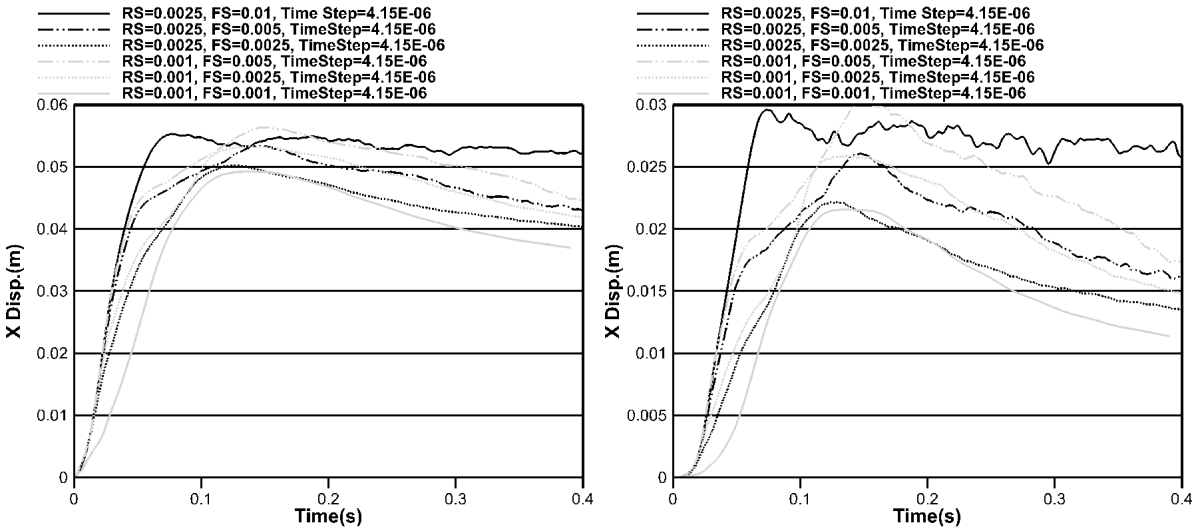

Figure 4.18: Plot of time history for the displacements at the tip of the gate with same time step and different RS and FS. (Left) X displacements. (Right) Z displacements.

It is found that when FS is less than RS, e.g., RS=0.0025 m, FS=0.001 m, all cases fail numerically since the smaller SPH particles penetrate into the structure and causing the simulation to terminate. Similarly, when RS=0.001 and FS=0.01, water penetration into the structure causes the numerical simulation to terminate. It is recommended that the ratio of structural node spacing to fluid particle spacing be larger than 1:5 but less than 1:1.

It is also of interest to estimate the ratio of computation time spent on the fluid and structural portions of this simulation. Table 4.3 shows the summarized results for all the completed cases. It is no surprise that the explicit SPH solver takes much less time than the implicit FEM solver. It is striking, however, the large amount of computational resources the FEM takes with increasingly finer meshing. It is therefore recommended for future work that an explicit FEM solver be tried and/or an optimized solver be developed for inverting the FEM global mass and stiffness matrices.

Table 4.3: Comparison of computational time for SPH and FEM solver.

Geometric Spacing (m)	Time Step (s)	Total No. Of Time steps	Total Time (h)	Fluid Time Percent.	Structure Time Percent.	Total Fluid No.	Total Structure No.	Time Per SPH Particle(s)	Time Per FEM Nodes(s)	Ratio per FEM Nodes To per SPH Particle
RS=0.0025, FS=0.01	4.15E-05	9649	0.05	3.55	95.82	140	96	0.05	1.80	39.42
	2.07E-05	19297	0.10	3.60	95.97	140	96	0.09	3.61	38.86
	1.04E-05	38594	0.20	3.57	96.12	140	96	0.18	7.21	39.24
	4.15E-06	96484	0.50	3.56	96.21	140	96	0.46	17.99	39.42
	2.07E-06	192968	0.99	3.57	96.23	140	96	0.91	35.79	39.33
RS=0.0025, FS=0.005	4.15E-05	9649	0.05	7.23	91.63	560	96	0.02	1.81	73.90
	2.07E-05	19297	0.11	7.09	92.15	560	96	0.05	3.79	75.78
	1.04E-05	38594	0.21	7.15	92.28	560	96	0.10	7.43	75.29
	4.15E-06	96484	0.52	7.35	92.19	560	96	0.24	17.90	73.18
	2.07E-06	192968	1.04	7.23	92.36	560	96	0.48	35.97	74.55
RS=0.0025, FS=0.0025	1.04E-05	38594	0.25	23.77	74.43	2240	96	0.10	6.94	73.06
	4.15E-06	96484	0.63	23.85	74.60	2240	96	0.24	17.57	73.00
	2.07E-06	192968	1.27	23.44	75.11	2240	96	0.48	35.90	74.78
RS=0.001, FS=0.005	1.66E-05	24121	22.08	0.10	99.89	560	480	0.15	165.43	1,116.59
	8.29E-06	48242	37.97	0.12	99.88	560	480	0.29	284.42	981.59
	4.15E-06	96484	69.02	0.13	99.87	560	480	0.57	516.97	902.33
RS=0.001, FS=0.0025	8.29E-06	48242	37.10	0.29	99.69	2240	480	0.17	277.43	1,607.64
	4.15E-06	96484	68.88	0.31	99.68	2240	480	0.34	514.90	1,517.68
RS=0.001, FS=0.001	4.15E-06	96484	69.23	0.80	99.64	14000	480	0.14	517.39	3,645.27

Chapter 5

SPH-FEM Applications to Hovercraft

5.1 Dynamics of Surface-Effect-Ship Bow Seal under High-Speed Flow

5.1.1 Experimental and Numerical Setup

The ultimate aim of this research is the development of a design tool for air cushion vehicles. As such, a modeling of a SES bow seal under high-speed flow is investigated to further validate the SPH-FEM model. The experimental data available in this research was provided by the Marine Hydrodynamics Laboratory of the University of Michigan. A summary of the results have been published in Zalek and Doctors (2010). The purpose of this experiment is stated as"The primary goal of this instrumentation suite is to obtain the seal total thrust force, mean geometric form and bow wave height for a given test apparatus speed, cushion pressure and seal initial immersion depth. Numerical modelers are expected to utilize this data to simulate these experiments in order validate their code performance" (Zalek and Doctors, 2010).

Interested readers are referred to Zalek and Doctors (2010) for detailed experimental setup. The

weight density of the flexible seal is given from the experimental database as 0.005 lb/in^2=3.51 kg/m^2 (Zalek, personal communication, Jan 19, 2011). With a seal thickness of 3.175 mm, the density in international units is 1107 kg/m^3. The flexural rigidity, defined in Eq. (5.1) was determined to be approximately 0.4 lbf-in/unit width based upon some simple beam-bending tests.

$$D = \frac{E_{YM} t^3}{12(1 - \nu^2)} \tag{5.1}$$

E_{YM} is the Young's Modulus of the material, ν is the Poisson's Ratio and t is the thickness of the seal. Given a typical value ν=0.25 for rubber, the Young's Modulus is E_{YM}=12.71 MPa. The parameters are listed in Table 5.1.

Table 5.1: Parameters of SES Experiment. (Geometry is per Zalek and Doctors (2010).)

.

SES Length	3.6576 m / 12 ft
SES Beam Width	1.524 m / 5 ft
SES Height	1.219 m / 4 ft
Bow Seal Slope	45°
Total Bow Seal Length	54.4 inches
Flexible Bow Seal Length	20 inches
Flexible Bow Seal Thickness	3.175 mm
Flexible Bow Seal Density	1107 kg/m^3
Flexible Bow Seal Poisson's Ratio	0.25
Flexible Bow Seal Young's Modulus	12.71 MPa

Since the 2D profiles of the SES projected onto the longitudinal slices are constant, a 2D SPH-FEM model is utilized as a numerical tool to simulate the seal dynamics of the SES and the numerical results are compared with the experimental results provided by Dr. Zalek at University of Michi-

gan. As described in Chapter 3, a FEM model is used to simulate the flexible bow seal and a SPH model is used for the free stream flow. As part of this thesis, two approaches were developed to simulate the air cushion chamber. The first approach is herein referred to as the specified-pressure approach. The effect of the air cushion is considered by adding a prescribed pressure equal to the given cushion pressure into the FEM nodes at the back side of the flexible bow seal. This approach ignores the air-water interaction at the back of the seal but boasts faster computation time. The other approach is referred to as the air-particle approach in which the cushioned air domain is simulated by distributing SPH particles, ie. a multiphase simulation is performed. This model includes all interaction between the water, cushion air and the bow seal but usually requires more computation resources and more stringent stability conditions.

A Monaghan boundary condition is applied where the hard structures of the SES are located and enforces the non-penetration condition for both air or water particles. The right boundary is an inlet condition in which several layers of SPH water particles are given free-stream properties. The left boundary is an outlet condition in which layers of SPH particles maintain their properties as they exit the computation domain. At the bottom of the water domain lie layers of virtual particles whose pressure is initialized with hydrostatic pressure. The number of the layers of particles at the inlet, outlet and bottom depend on the smoothing length, chosen such that the SPH particles inside the computation domain do not suffer boundary deficiency problems. At the beginning of the simulation, the SPH water particles are initialized with free-stream velocity and hydrostatic pressure and are updated using the SPH formulation. The index of the particles exiting the computational domain is recorded and given to the new water particles generated at the inlet so that the total number of particles is limited and computational resources are saved.

Section 5.1.2 and Section 5.1.3 show the simulation and validation results using both the specified-pressure and air-particle approaches given the SES initial immersion depth, cushion pressure inside the chamber and flow speed / SES forward speed.

5.1.2 Validation Results Using Specified-Pressure Approach

The SPH-FEM model described in Chapter 4 is utilized to simulate SES skirt dynamics. The results are then compared with the experiment by Zalek and Doctors (2010) as a validation case. The initial numerical configuration is illustrated in Fig. 5.1. SPH fluid particles are distributed uniformly to a finite depth in a rectangular domain. The FEM mesh is used to simulate the lower flexible part of the bow seal with its top boundary clamped onto the rigid part of the bow seal. Interface particles are distributed along the boundary of the flexible seal and transmit fluid-structure interaction forces back and forth in a explicit manner. Monaghan-type boundary particles are placed along the SES hard-structure. The stern part of the SES is neglected to save computational resources. The simulation parameters for this validation case are listed in Table 5.2. The input data include initial immersion depth, cushion pressure and flow speed. The initial immersion depth are chosen as either 7.5 or 9 inches. In the experiment the cushion pressures range from 2–5.2 inches-H_20. In the simulation, the cushion pressures range from 0 to 9 inches-H_20, with increments of 1, to give broad coverage to the parameters domain. The flow speeds in the simulation are chosen corresponding to the flow speeds given in the experimental results. The flow speeds are 6, 7, 8, 9 ft/s at the initial immersion depth of 7.5 inches and 6, 8, 9, 10 ft/s at the initial immersion depth of 9 inches. So for each initial immersion depth, there are 40 runs, giving a total of 80 simulations for the two initial immersion depths. Time histories of the displacements, the bow wave height and the water resistance are recorded. A typical example of the time history curves are shown in Fig. 5.2. Consistent with the experimental data reduction, the mean values of these curves are then calculated after they reach a quasi-steady state (usually averaging from 20-40s) and are compared with the available experimental results. Additionally, the standard deviations from this averaging of the quasi-steady state values are calculated and plotted as error bars on Fig. 5.3 to Fig. 5.18. The validation results are shown in Fig. 5.3 through Fig. 5.18. Two simulation cases are presented in Fig. 5.19 and Fig. 5.20, one with initial immersion depth=7.5 inches, flow speed=6 ft/s, cushion pressure=2 inches-H_20 and the other one initial immersion depth=9 inches, flow speed=10 ft/s,

cushion pressure=9 inches-H_20.

Table 5.2: Simulation parameters using the specified-pressure approach. (Geometry is per Zalek and Doctors (2010).)

Initial immersion depth of SES	7.5 inches and 9 inches
Flow speed	6-10 ft/s
Cushion pressure	0-9 inch-H_20
Water width	10 m
Water height	2 m
Water viscosity	1.0E-6
Reynolds number	3.48E5–6.97E5
No. of structural FEM nodes	13x2 (Config. 0) 25x3 (Config. 1) 52x3 (Config. 2)
No. of interface particles	28 (Config. 0) 53 (Config. 1) 157 (Config. 2)
No. of hard-structure particles	126 (Config. 0) 242 (Config. 1) 586 (Config. 2)
No. of water particles	1993 (Config. 0) 7985 (Config. 1) 49964 (Config. 2)
No. of virtual boundary particles	320 (Config. 0) 800 (Config. 1) 2000 (Config. 2)
dt	3.31E-5 s.
Simulation time	40 s
Total No. of time step	0.2 Million (Config. 0) $\approx$ 0.4 Million (Config. 1) $\approx$ 1.2 Million (Config. 2)
CPU Frequency	3.33 GHz
Computation time	20 minutes (Config. 0) 6 hours (Config. 1) 8 days (Config. 2)

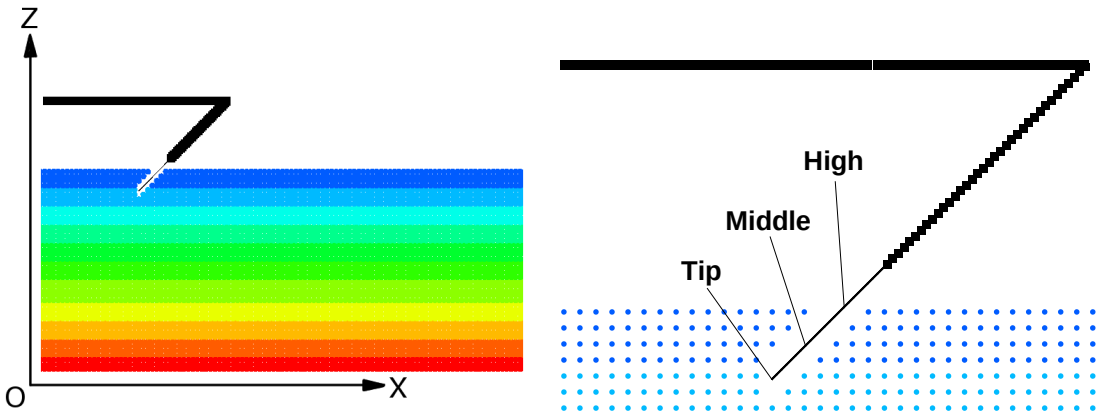

5.1.1 5.1.2

Figure 5.1: Initial configuration Of SPH-FEM model simulating bow seal dynamics under high-speed flow using specified-pressure approach.

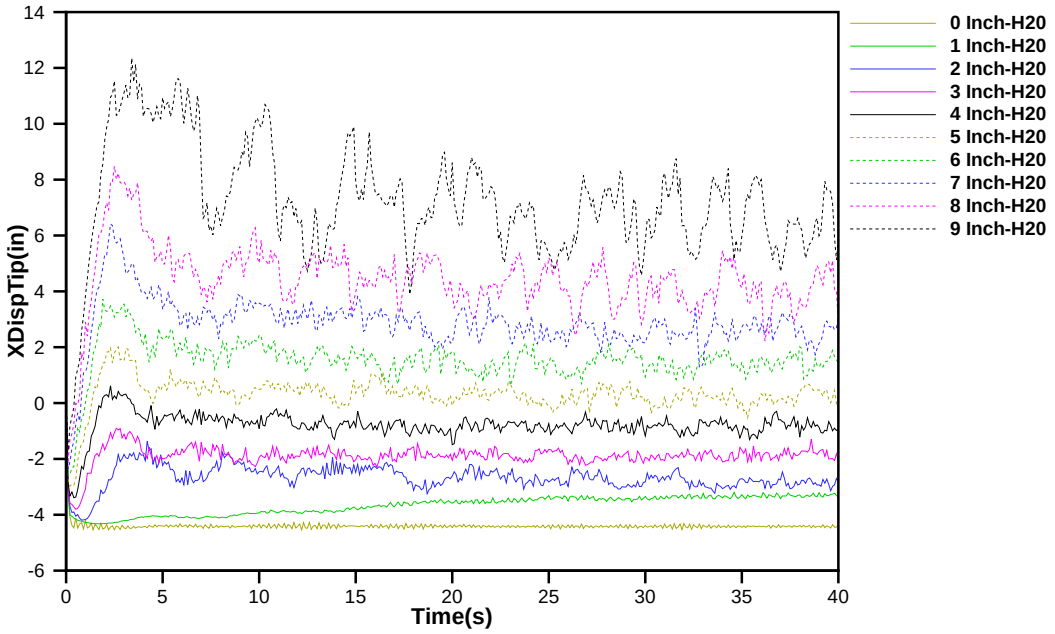

5.2.1 X Displacement at the Tip of the Bow Seal with Initial Immersion Depth = 7.5 inches, Flow Speed = 6 ft/s, Cushion Pressure Ranging from 0-9 inches-H_20

Figure 5.2: Time history curves for initial immersion depth = 7.5 inches, flow speed = 6 ft/s, cushion pressure ranging from 0-9 inches-H_20.

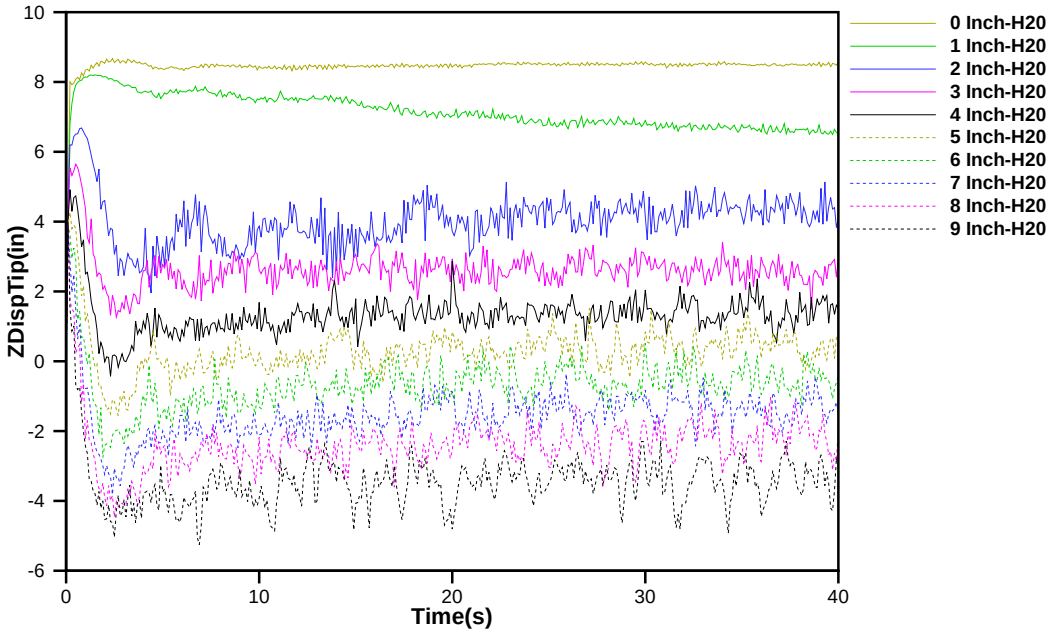

5.2.2 Z Displacement at the Tip of the Bow Seal with Initial Immersion Depth = 7.5 inches, Flow Speed = 6 ft/s, Cushion Pressure Ranging from 0-9 inches-H_20

Figure 5.2: Time history curves for initial immersion depth = 7.5 inches, flow speed = 6 ft/s, cushion pressure ranging from 0-9 inches-H_20. (Continued.)

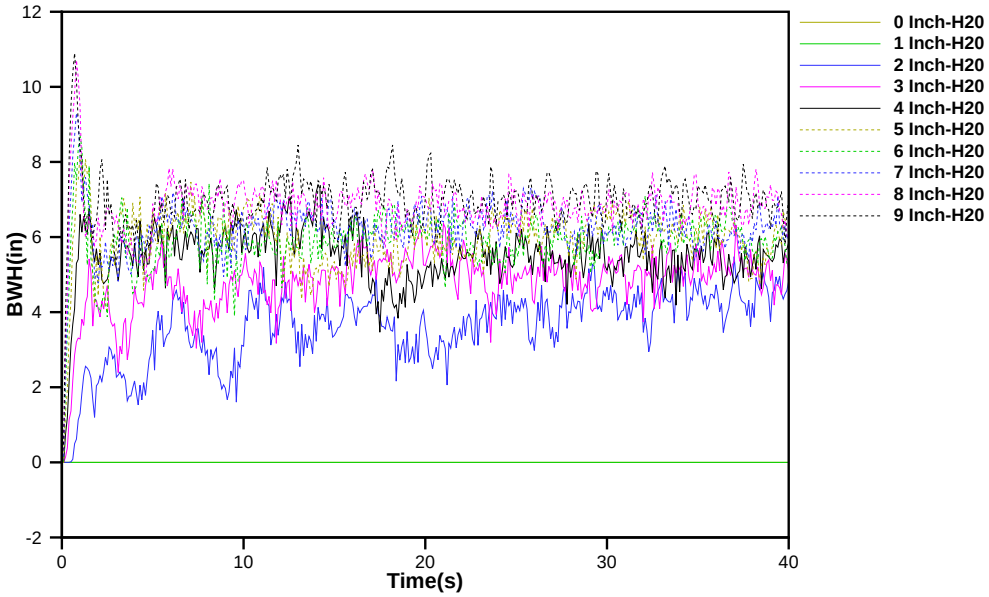

5.2.3 Bow Wave Height before the Bow Seal with Initial Immersion Depth = 7.5 inches, Flow Speed = 6 ft/s, Cushion Pressure Ranging from 0-9 inches-H_20

Figure 5.2: Time history curves for initial immersion depth = 7.5 inches, flow speed = 6 ft/s, cushion pressure ranging from 0-9 inches-H_20. (Continued.)

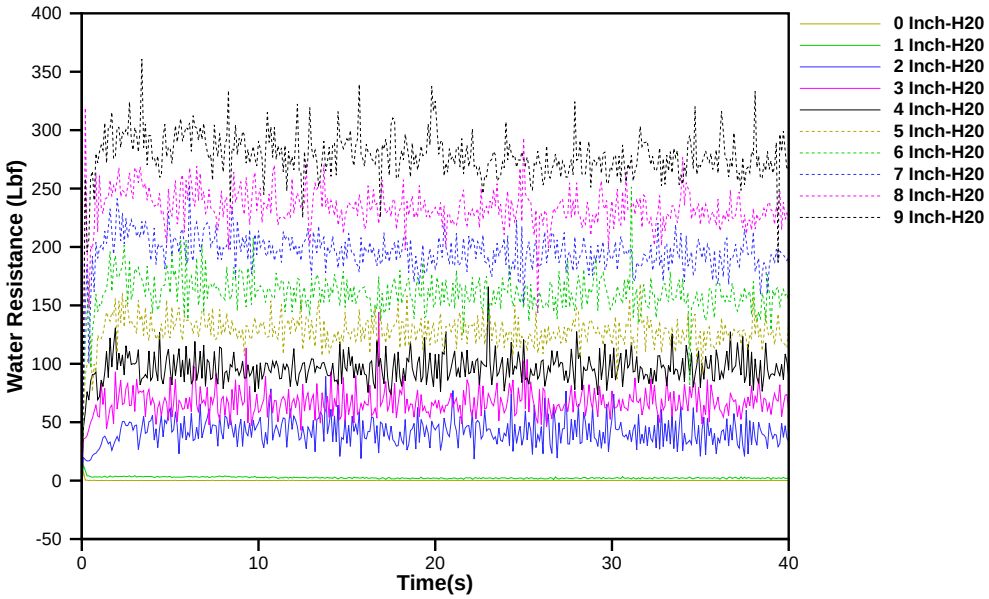

5.2.4 Water Resistance on the Bow Seal with Initial Immersion Depth = 7.5 inches, Flow Speed = 6 ft/s, Cushion Pressure Ranging from 0-9 inches-H_20

Figure 5.2: Time history curves for initial immersion depth = 7.5 inches, flow speed = 6 ft/s, cushion pressure ranging from 0-9 inches-H_20. (Continued.)

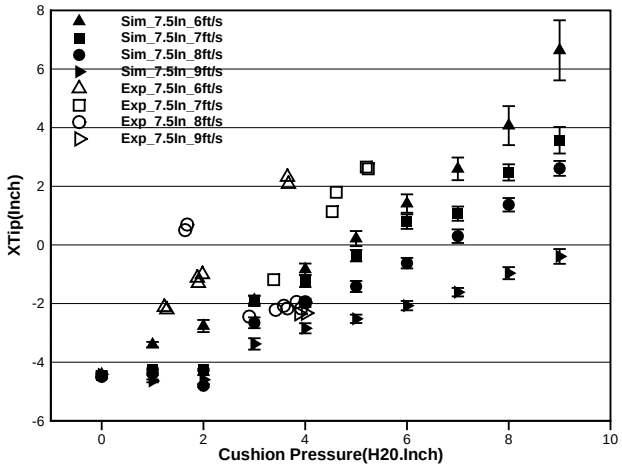

5.3.1

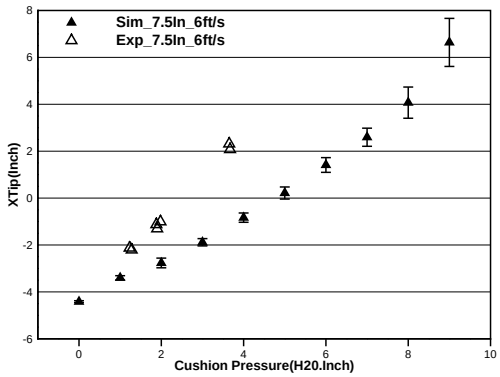

5.3.2

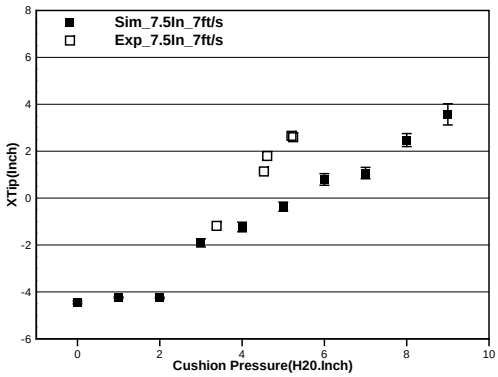

5.3.3

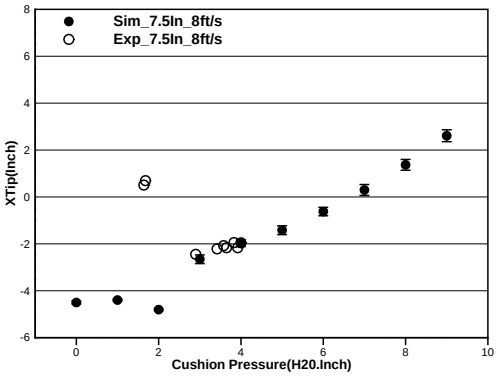

5.3.4

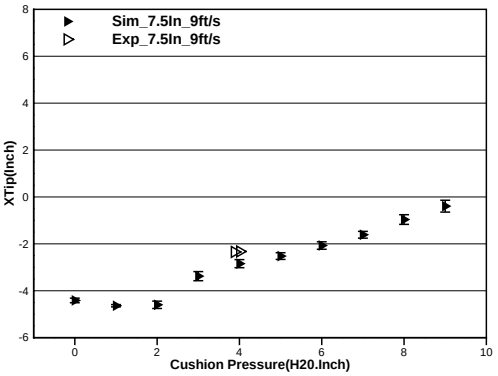

5.3.5

Figure 5.3: Comparison between experiment and SPH-FEM specified-pressure model for X displacement at the tip position of the bow seal for 7.5-inch depth. Error bars denote standard deviation from the mean value.

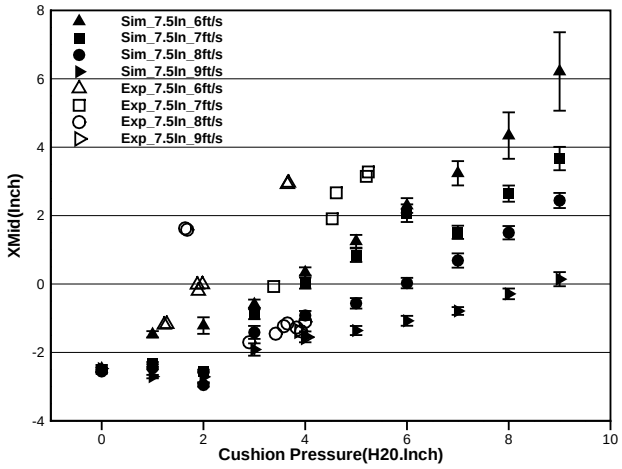

5.4.1

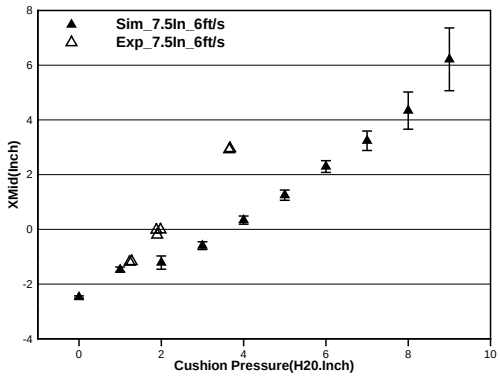

5.4.2

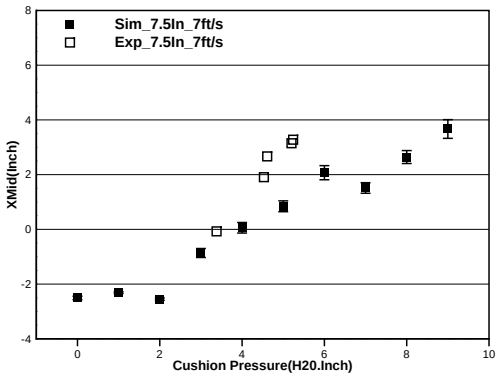

5.4.3

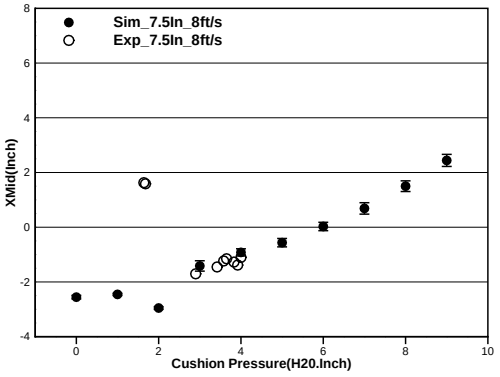

5.4.4

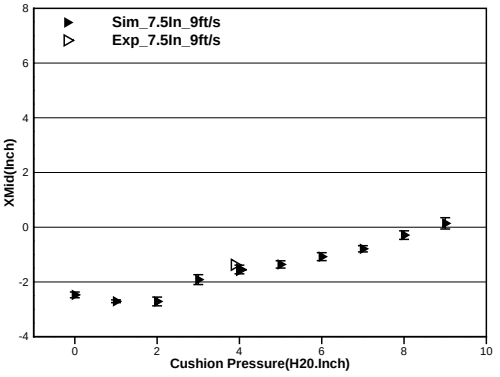

5.4.5

Figure 5.4: Comparison between experiment and SPH-FEM specified-pressure model for X displacement at the middle position of the bow seal for 7.5-inch depth. Error bars denote standard deviation from the mean value.

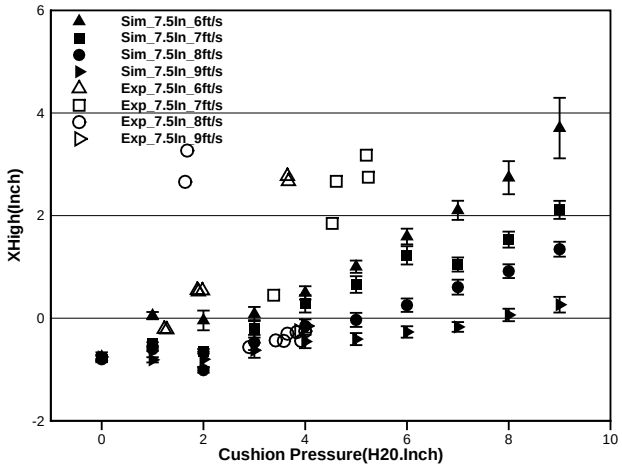

5.5.1

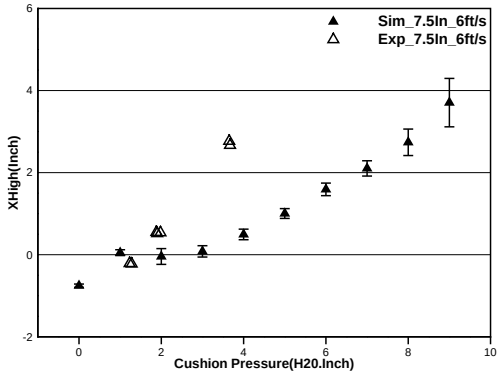

5.5.2

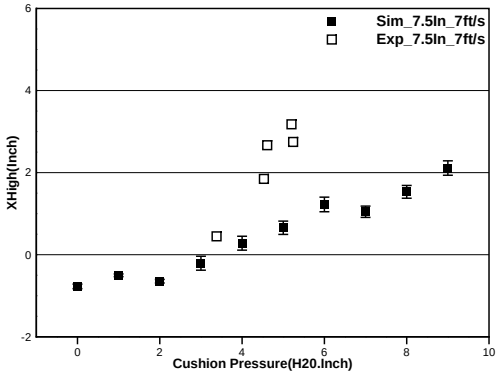

5.5.3

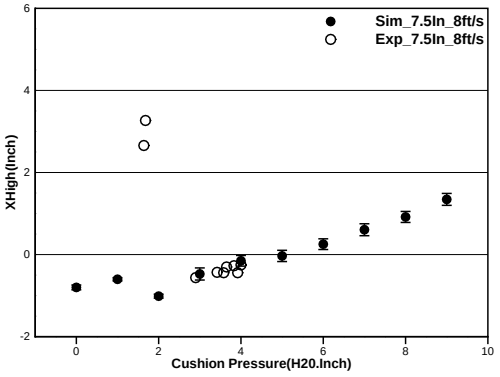

5.5.4

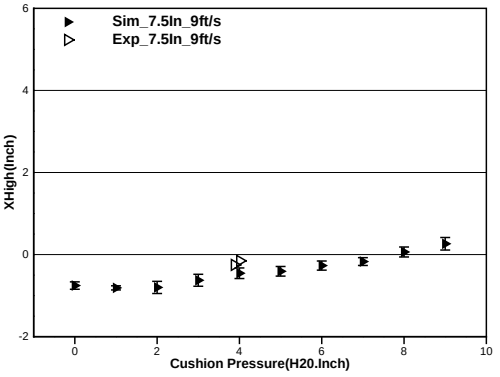

5.5.5

Figure 5.5: Comparison between experiment and SPH-FEM specified-pressure model for X displacement at the high position of the bow seal for 7.5-inch depth. Error bars denote standard deviation from the mean value.

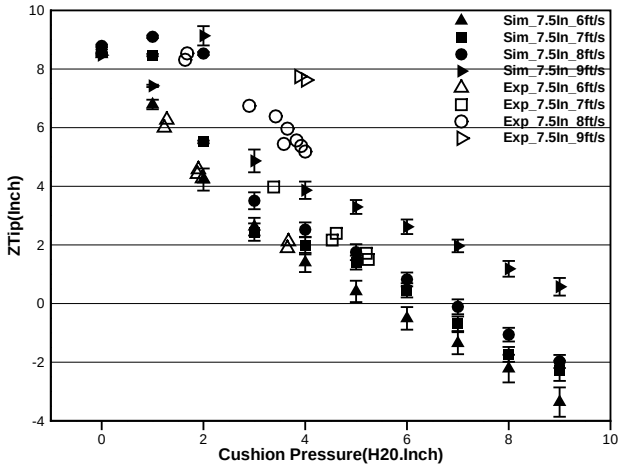

5.6.1

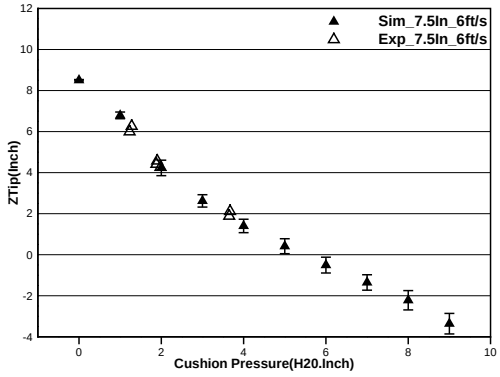

5.6.2

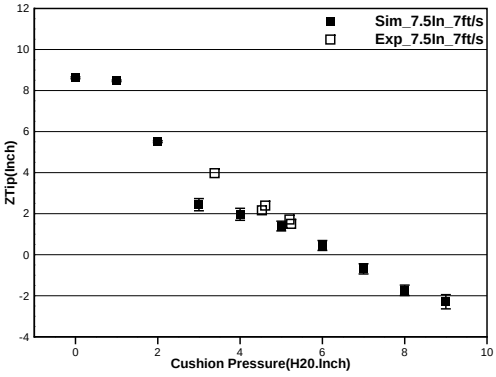

5.6.3

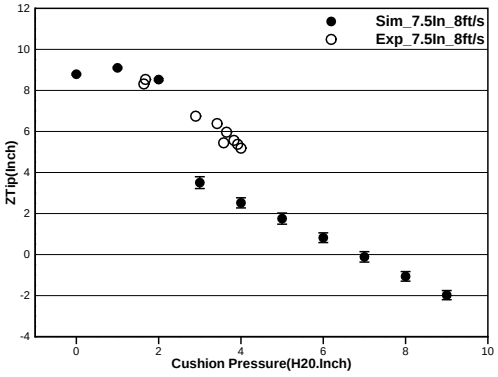

5.6.4

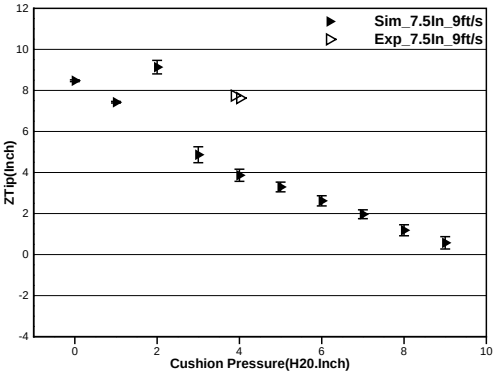

5.6.5

Figure 5.6: Comparison between experiment and SPH-FEM specified-pressure model for Z displacement at the tip position of the bow seal for 7.5-inch depth. Error bars denote standard deviation from the mean value.

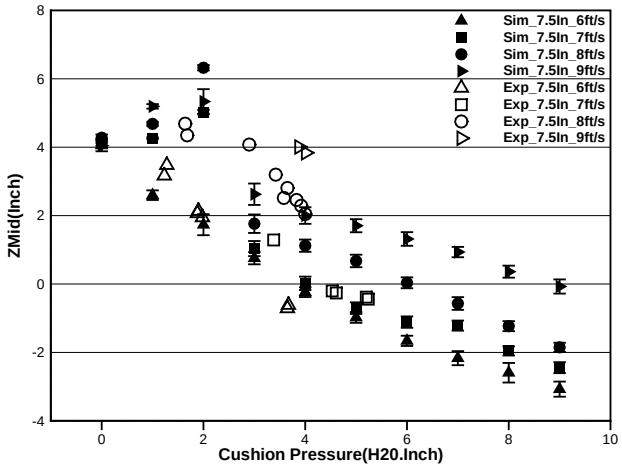

5.7.1

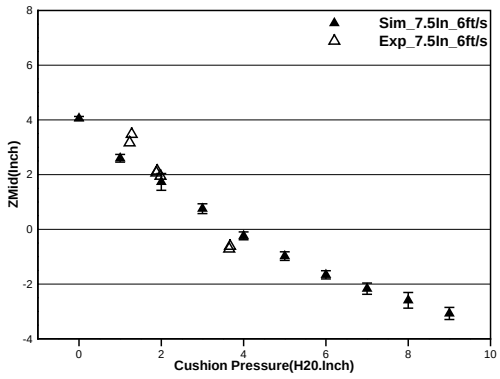

5.7.2

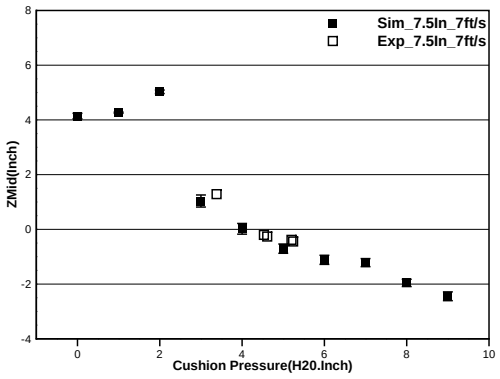

5.7.3

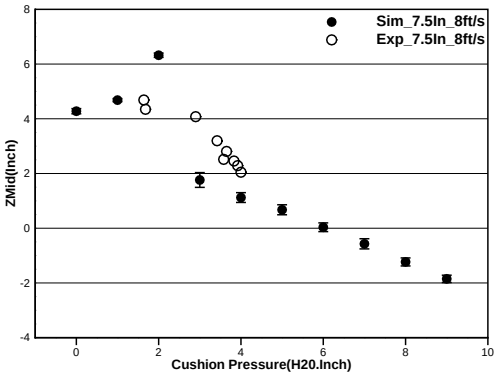

5.7.4

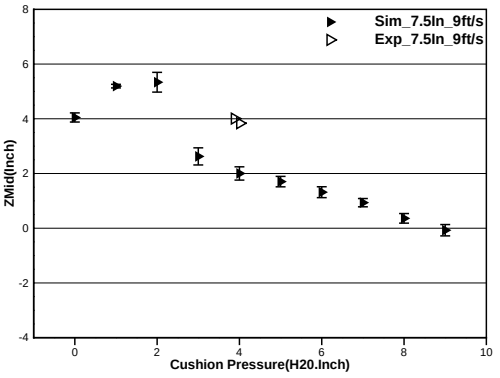

5.7.5

Figure 5.7: Comparison between experiment and SPH-FEM specified-pressure model for Z displacement at the middle position of the bow seal for 7.5-inch depth. Error bars denote standard deviation from the mean value.

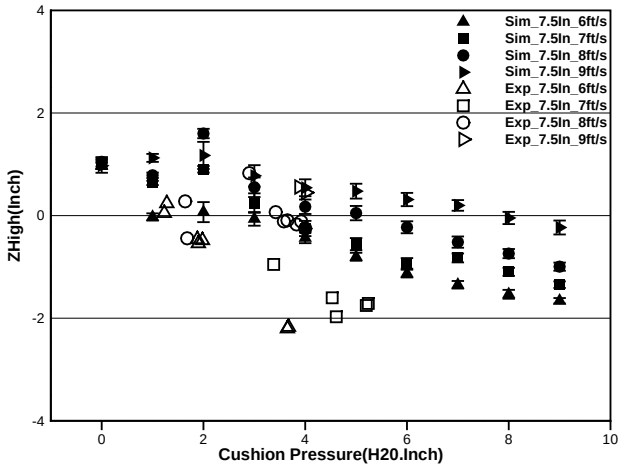

5.8.1

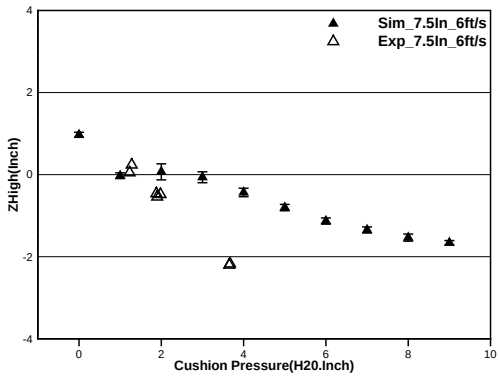

5.8.2

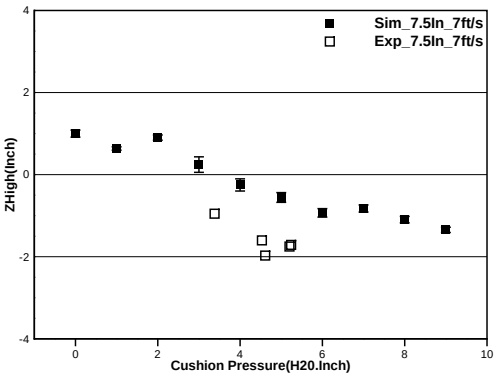

5.8.3

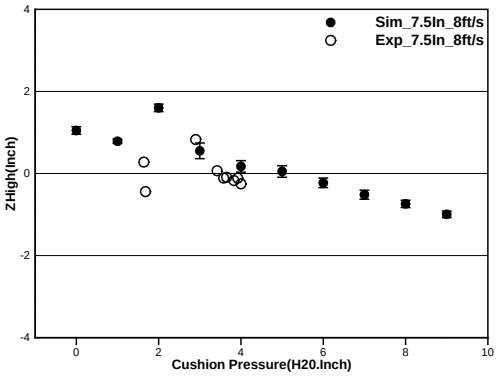

5.8.4

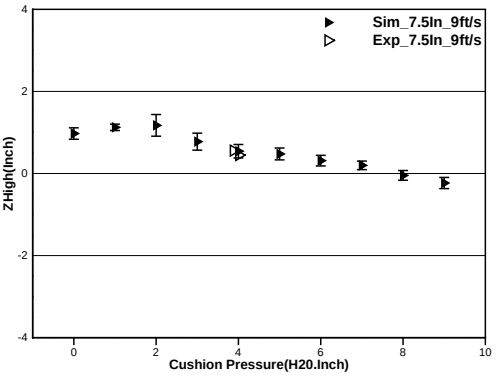

5.8.5

Figure 5.8: Comparison between experiment and SPH-FEM specified-pressure model for Z displacement at the high position of the bow seal for 7.5-inch depth. Error bars denote standard deviation from the mean value.

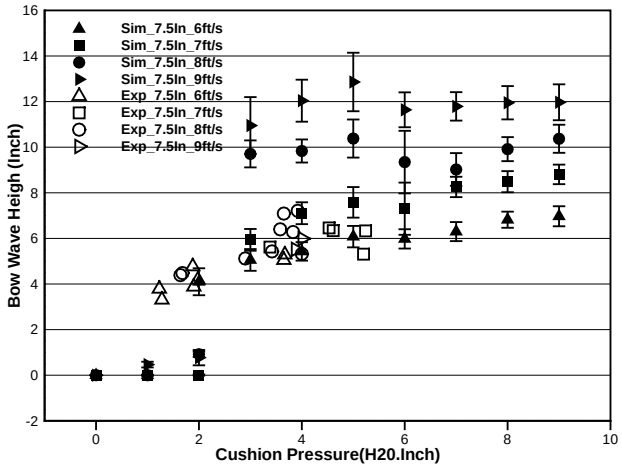

5.9.1

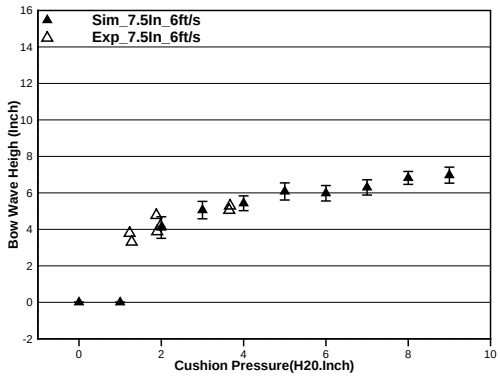

5.9.2

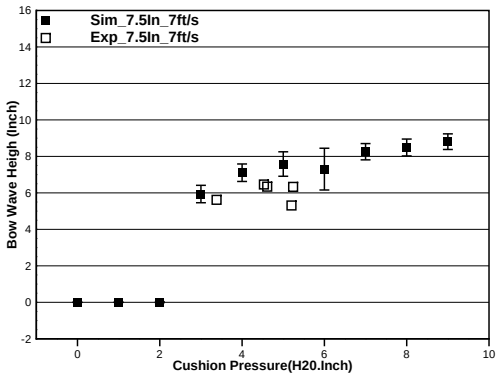

5.9.3

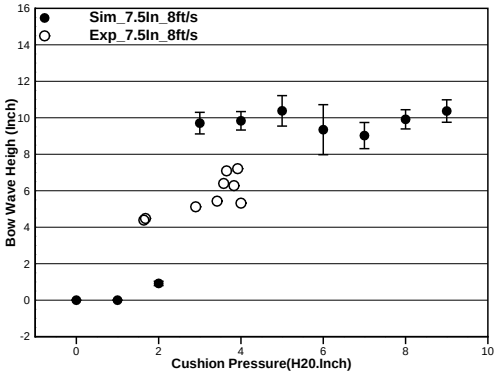

5.9.4

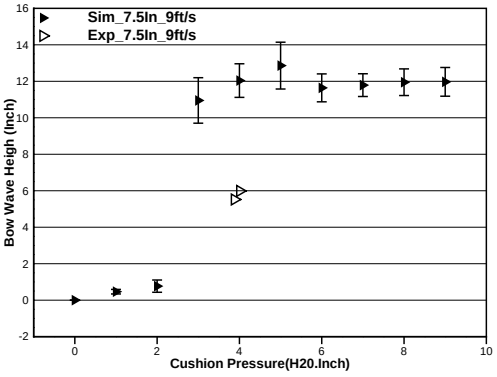

5.9.5

Figure 5.9: Comparison between experiment and SPH-FEM specified-pressure model for wave rise before the bow seal for 7.5-inch depth. Error bars denote standard deviation from the mean value.

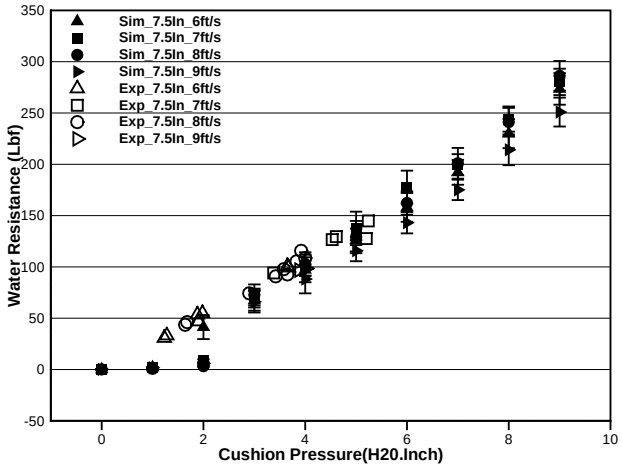

5.10.1

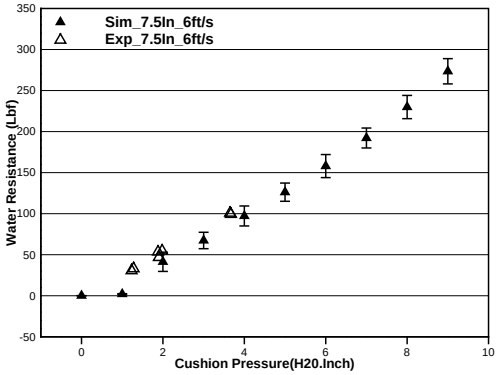

5.10.2

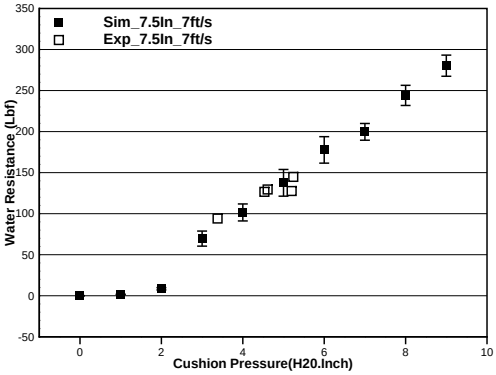

5.10.3

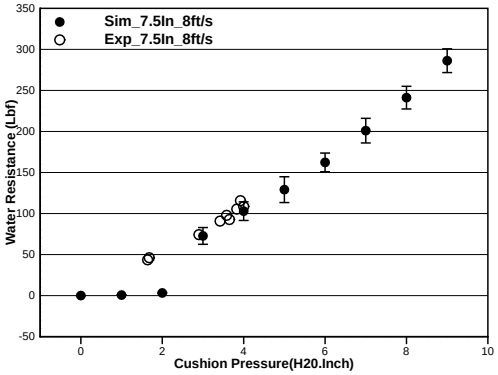

5.10.4

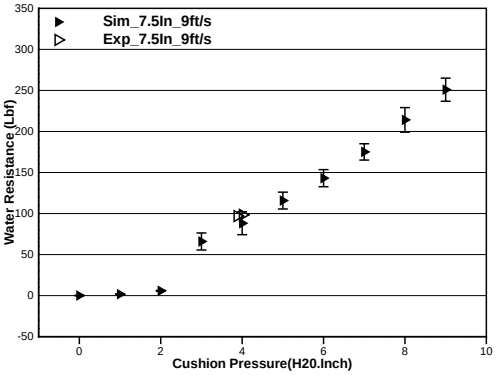

5.10.5

Figure 5.10: Comparison between experiment and SPH-FEM specified-pressure model for water resistance on the bow seal for 7.5-inch depth. Error bars denote standard deviation from the mean value.

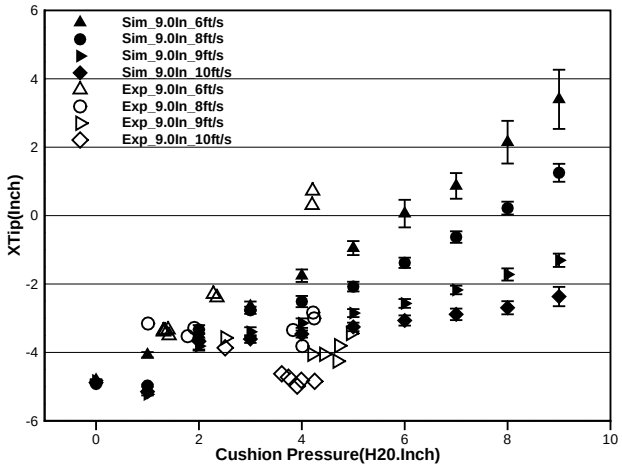

5.11.1

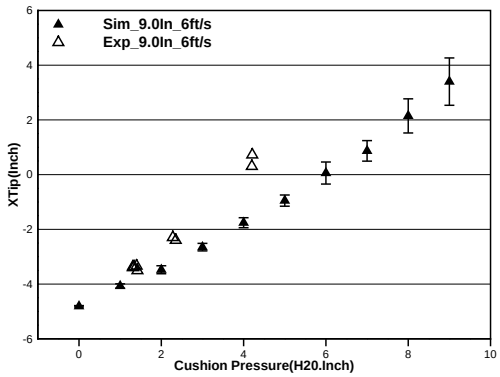

5.11.2

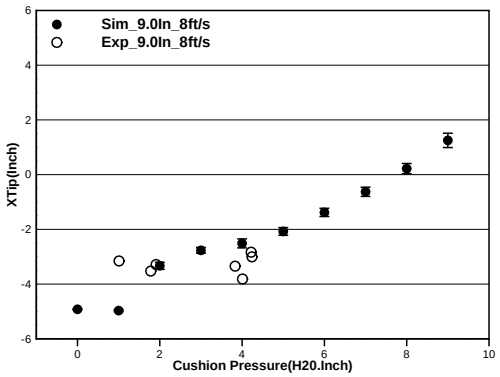

5.11.3

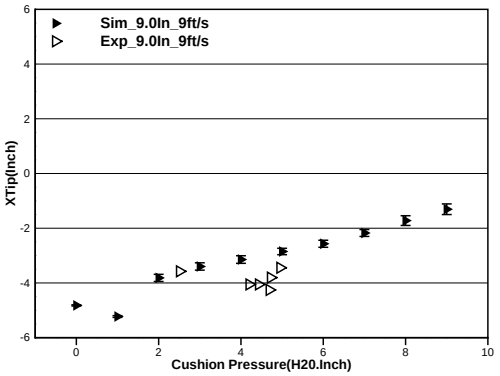

5.11.4

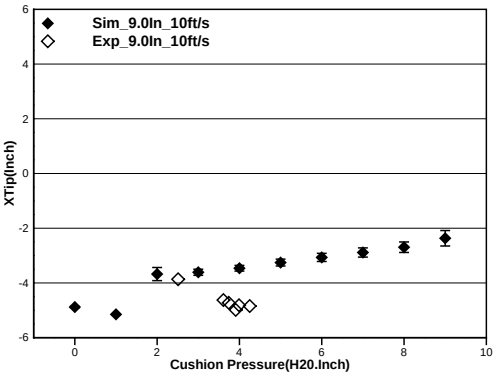

5.11.5

Figure 5.11: Comparison between experiment and SPH-FEM specified-pressure model for X displacement at the tip position of the bow seal for 9-inch depth. Error bars denote standard deviation from the mean value.

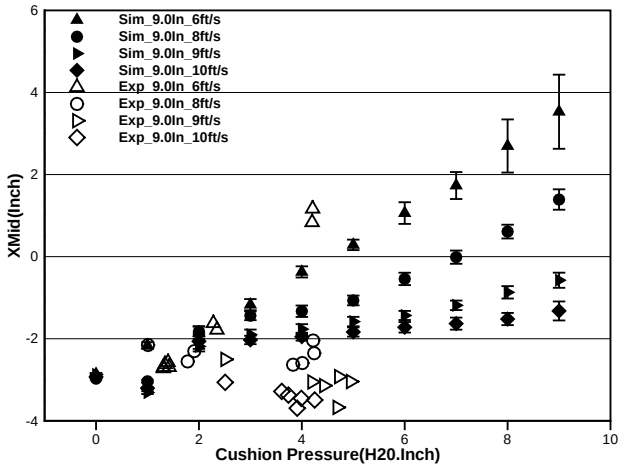

5.12.1

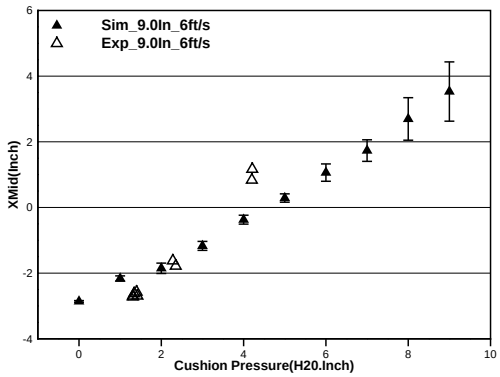

5.12.2

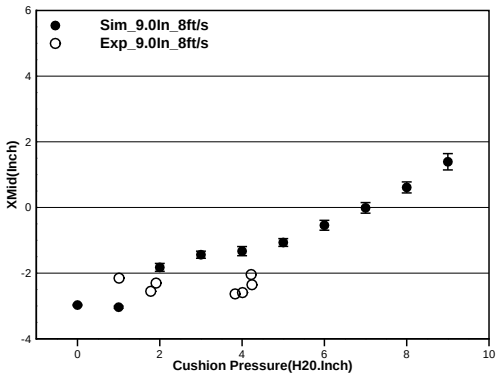

5.12.3

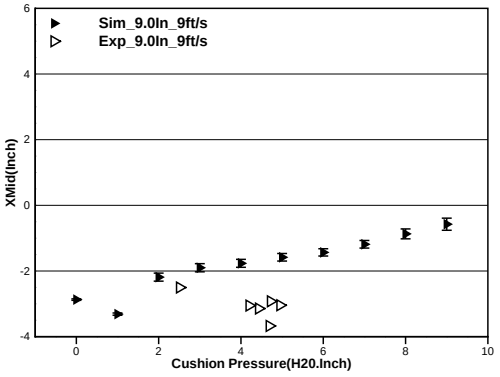

5.12.4

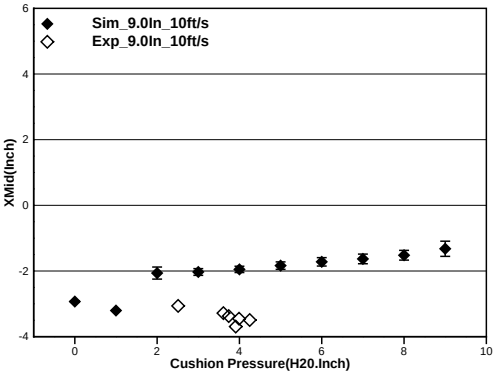

5.12.5

Figure 5.12: Comparison between experiment and SPH-FEM specified-pressure model for X displacement at the middle position of the bow seal for 9-inch depth. Error bars denote standard deviation from the mean value.

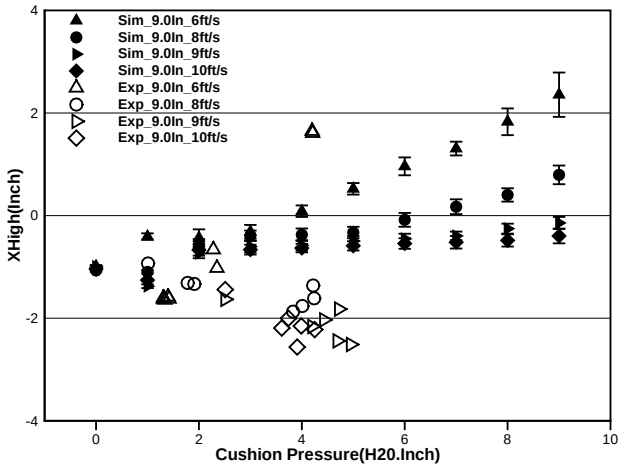

5.13.1

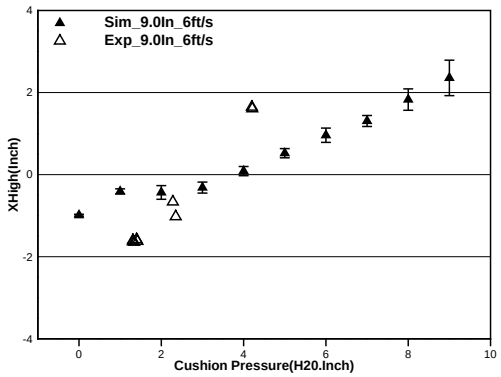

5.13.2

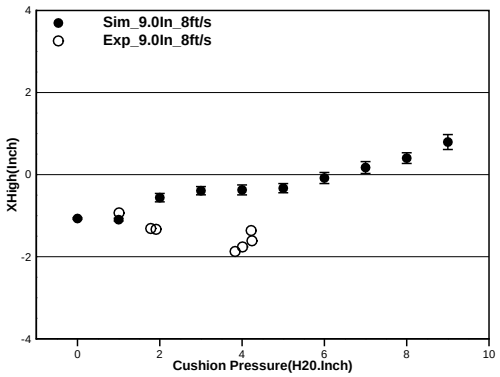

5.13.3

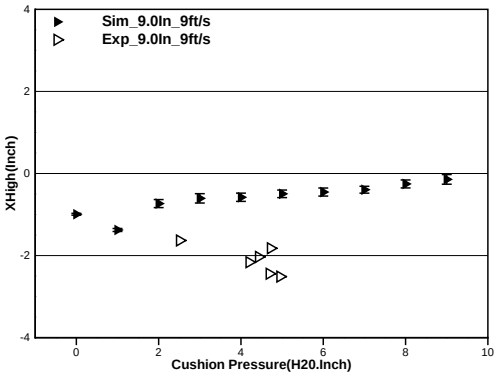

5.13.4

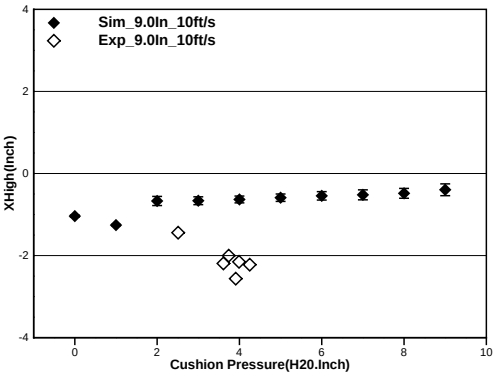

5.13.5

Figure 5.13: Comparison between experiment and SPH-FEM specified-pressure model for X displacement at the high position of the bow seal for 9-inch depth. Error bars denote standard deviation from the mean value.

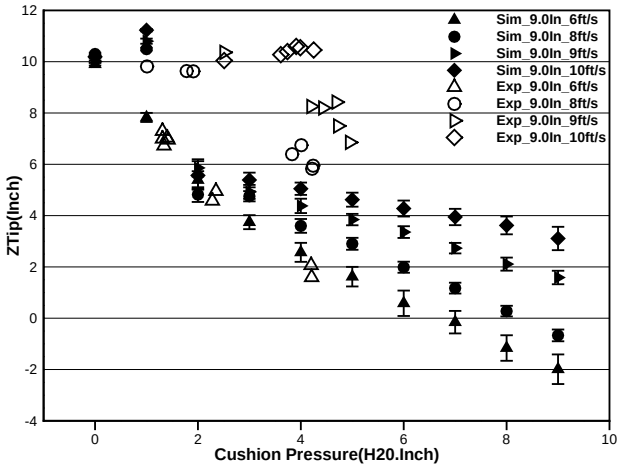

5.14.1

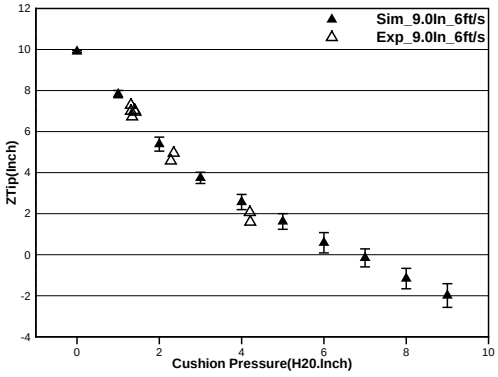

5.14.2

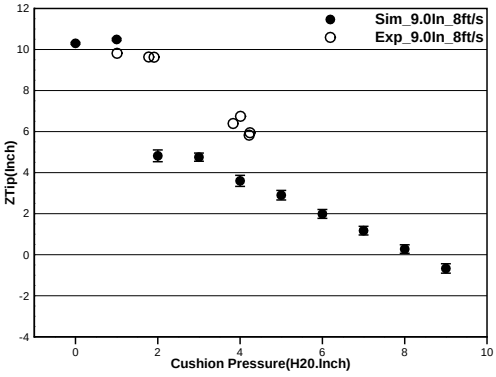

5.14.3

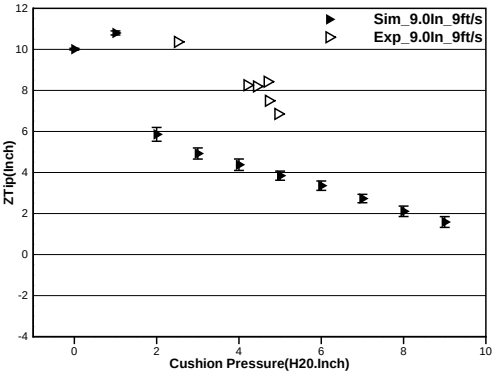

5.14.4

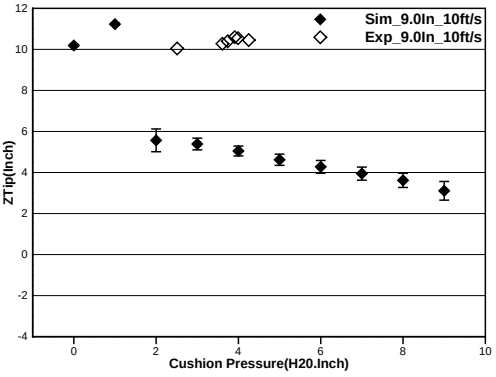

5.14.5

Figure 5.14: Comparison between experiment and SPH-FEM specified-pressure model for Z displacement at the tip position of the bow seal for 9-inch depth. Error bars denote standard deviation from the mean value.

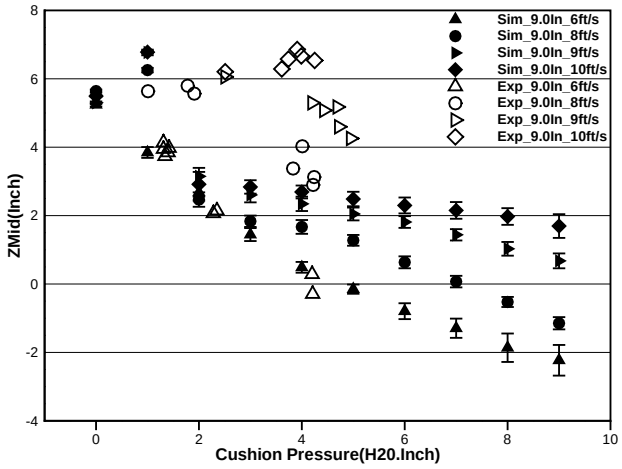

5.15.1

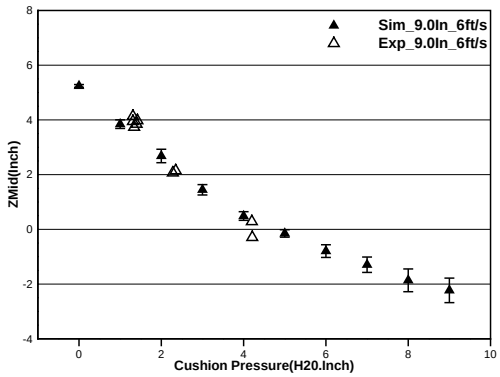

5.15.2

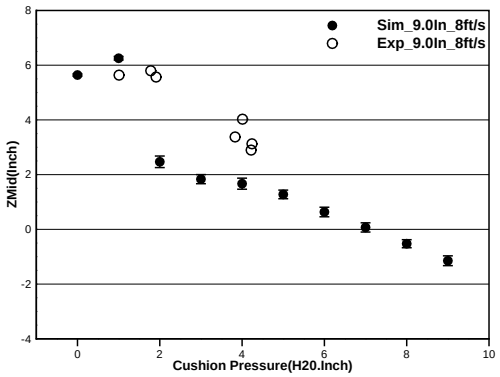

5.15.3

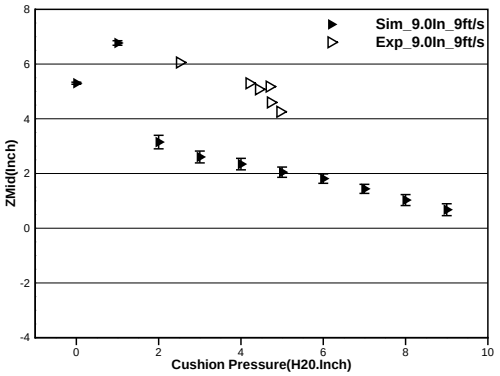

5.15.4

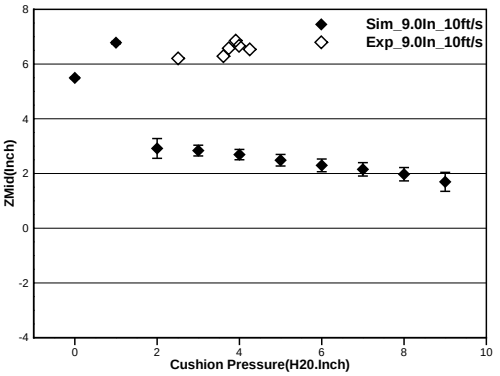

5.15.5

Figure 5.15: Comparison between experiment and SPH-FEM specified-pressure model for Z displacement at the middle position of the bow seal for 9-inch depth. Error bars denote standard deviation from the mean value.

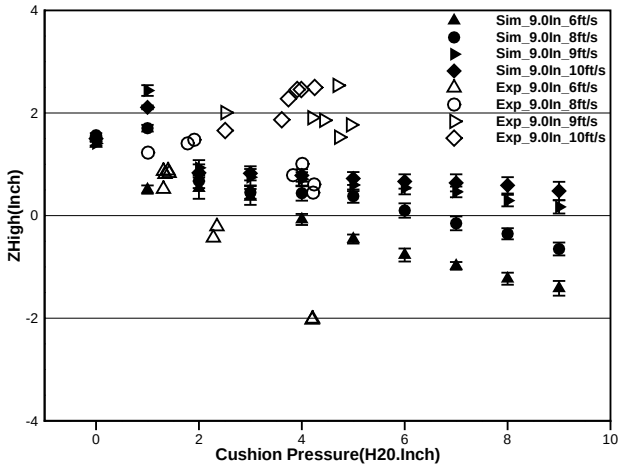

5.16.1

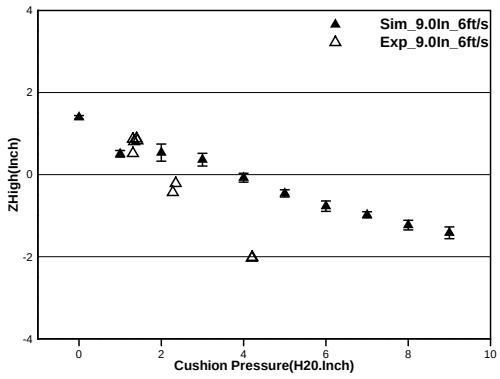

5.16.2

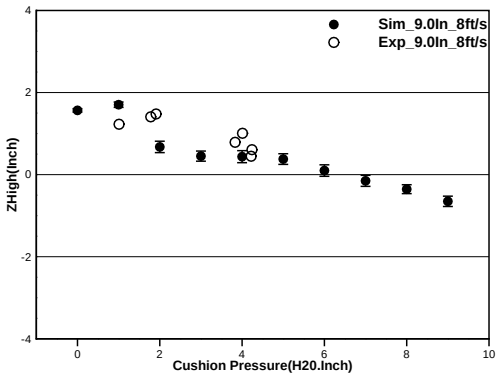

5.16.3

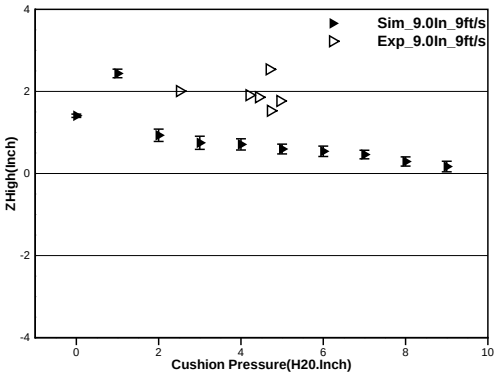

5.16.4

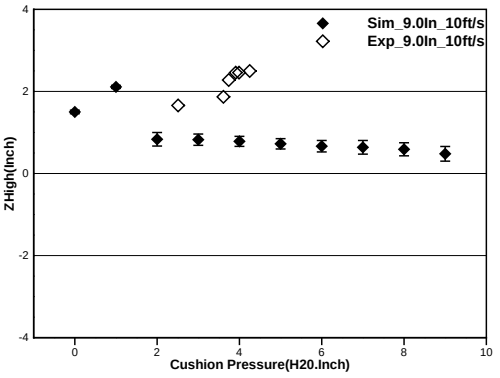

5.16.5

Figure 5.16: Comparison between experiment and SPH-FEM specified-pressure model for Z displacement at the high position of the bow seal for 9-inch depth. Error bars denote standard deviation from the mean value.

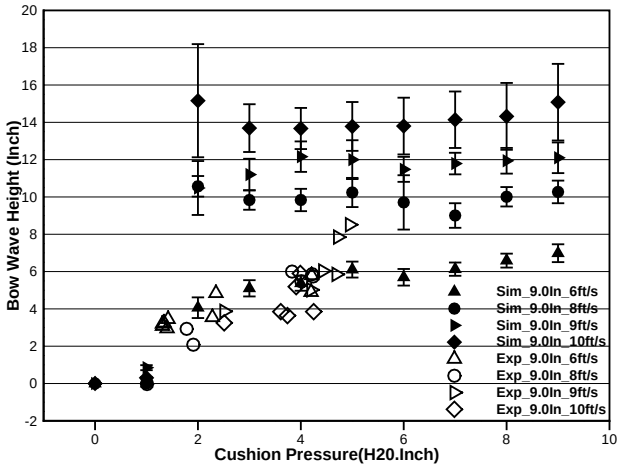

5.17.1

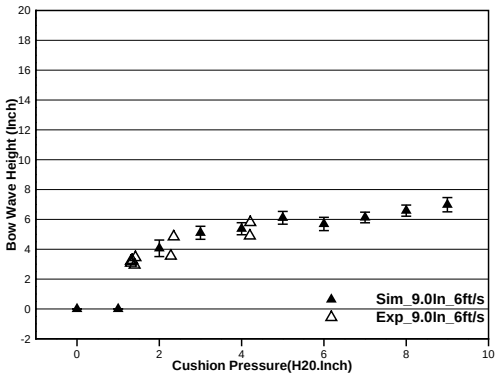

5.17.2

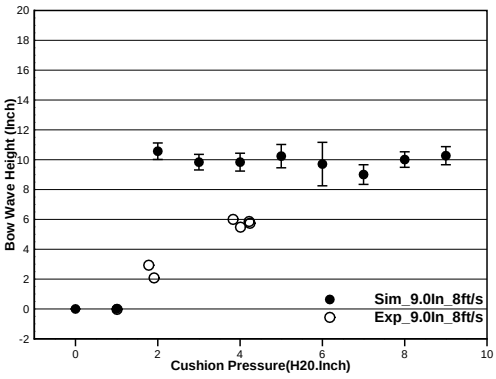

5.17.3

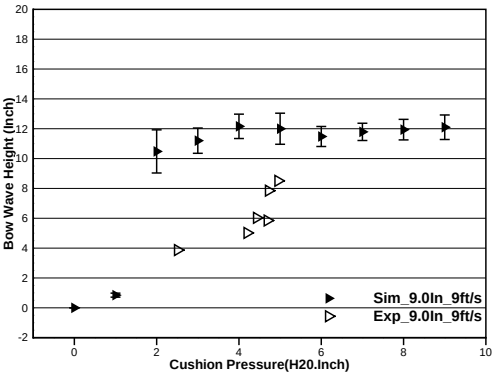

5.17.4

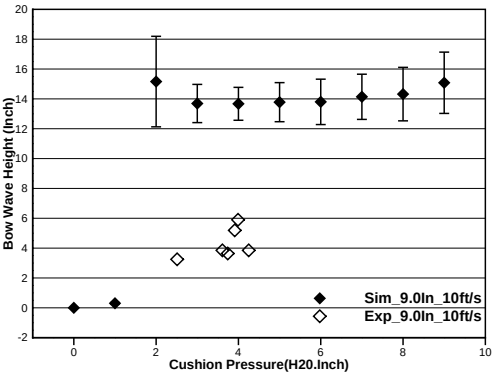

5.17.5

Figure 5.17: Comparison between experiment and SPH-FEM specified-pressure model for wave rise before the bow seal for 9-inch depth. Error bars denote standard deviation from the mean value.

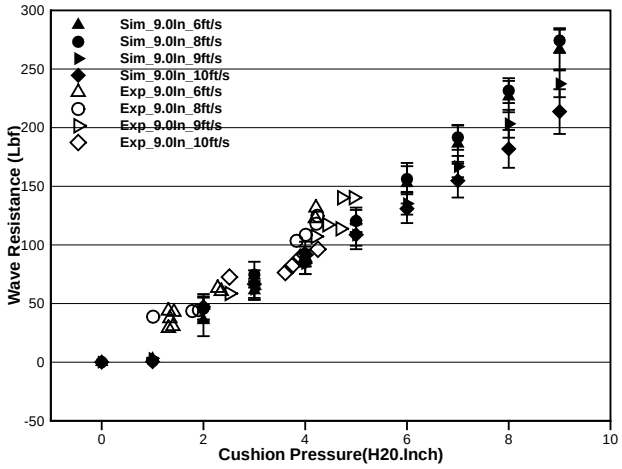

5.18.1

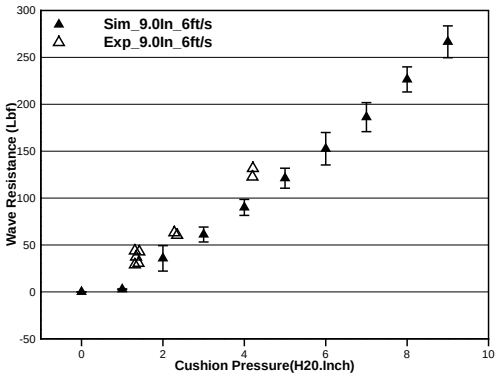

5.18.2

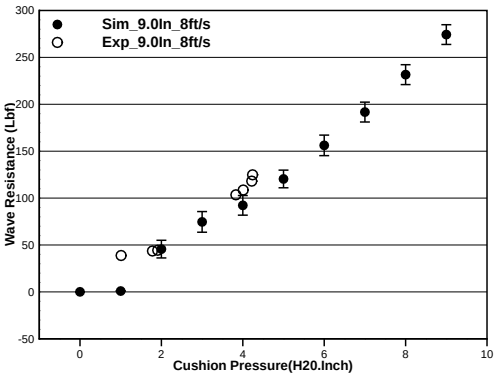

5.18.3

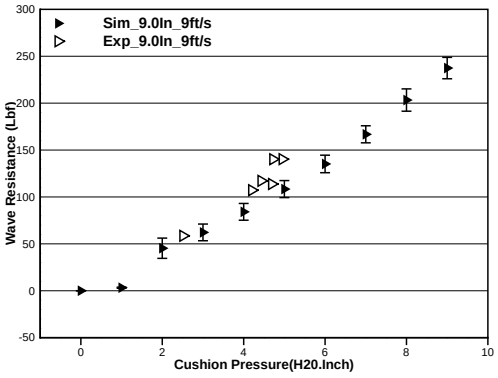

5.18.4

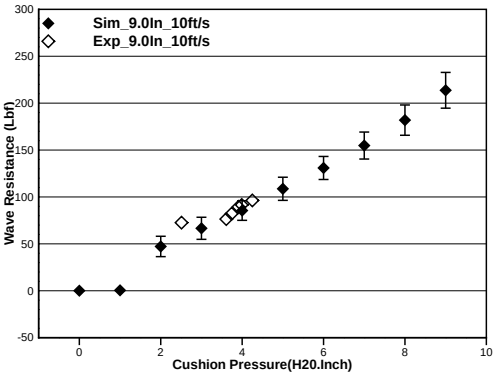

5.18.5

Figure 5.18: Comparison between experiment and SPH-FEM specified-pressure model for water resistance on the bow seal for 9-inch depth. Error bars denote standard deviation from the mean value.

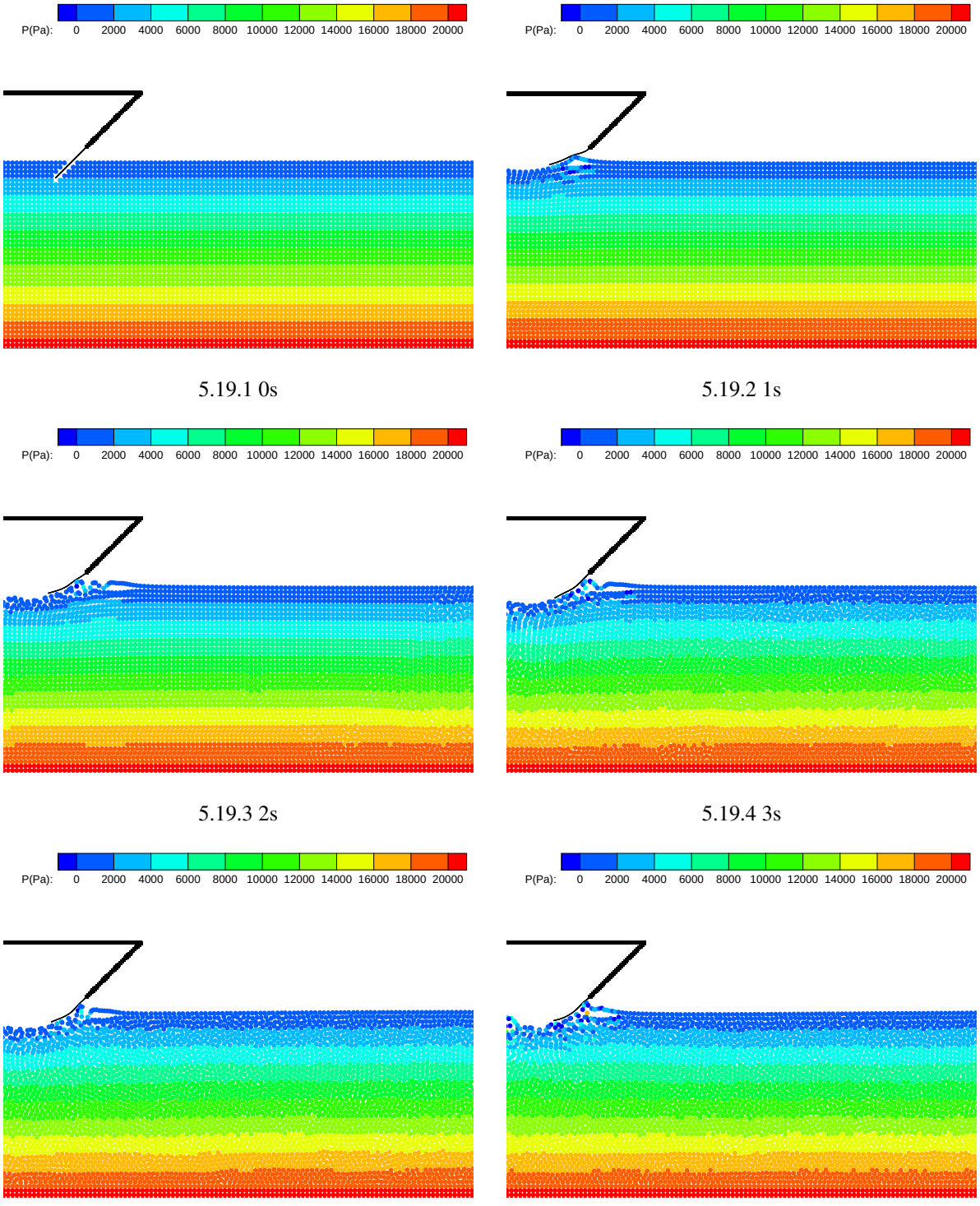

Figure 5.19: Whole simulation with initial immersion depth = 7.5 inches, flow speed = 6 ft/s, cushion pressure = 2 inches-H_20

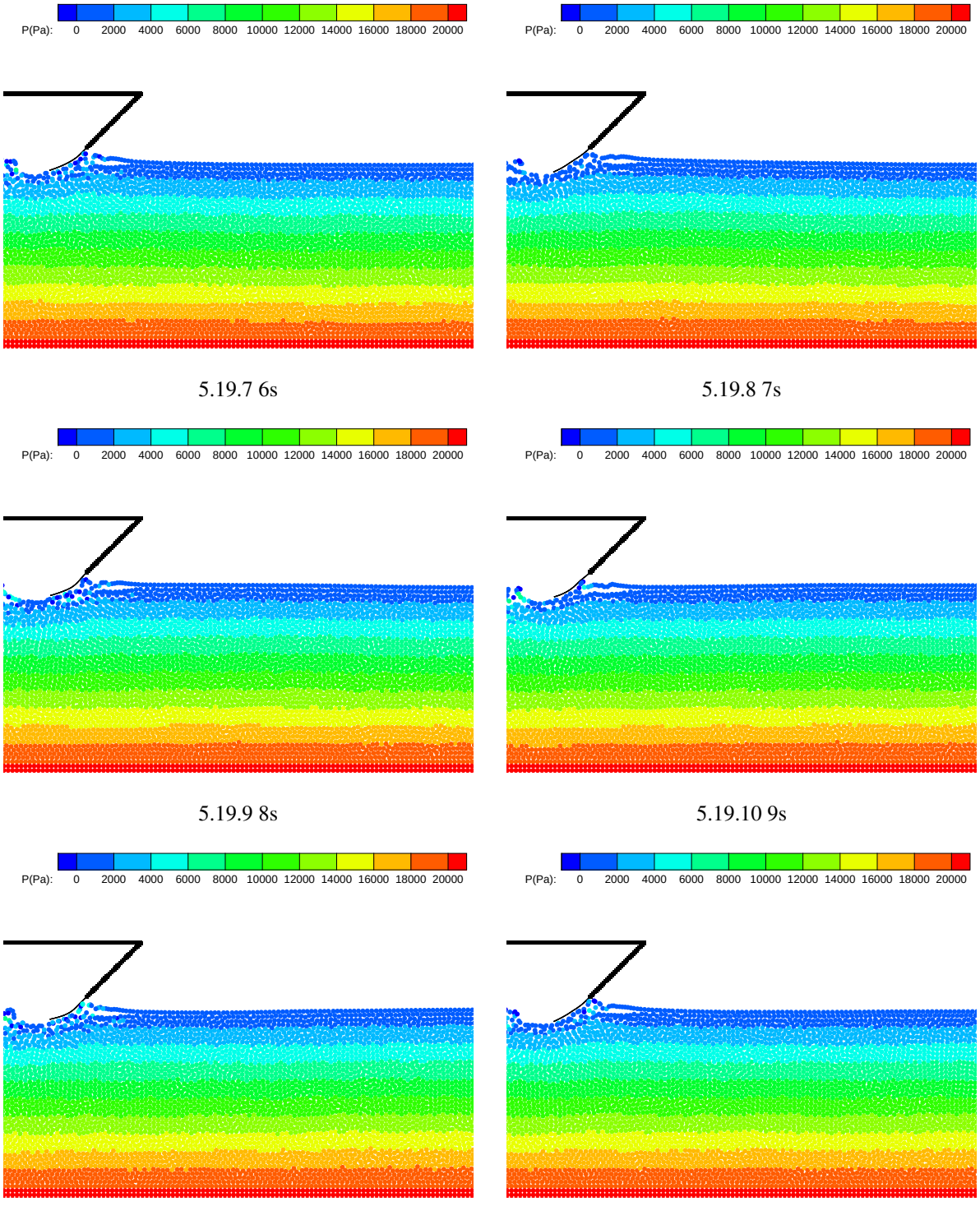

Figure 5.19: Whole simulation with initial immersion depth = 7.5 inches, flow speed = 6 ft/s, cushion pressure = 2 inches-H_20 (Continued)

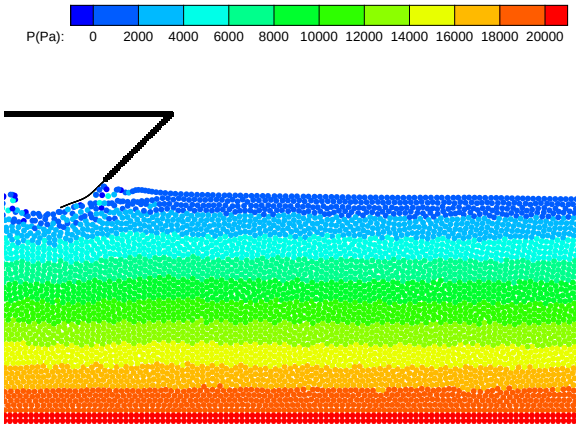

5.19.13 12s

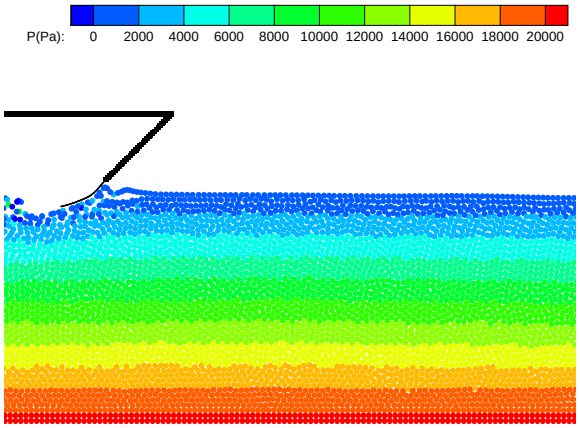

5.19.14 13s

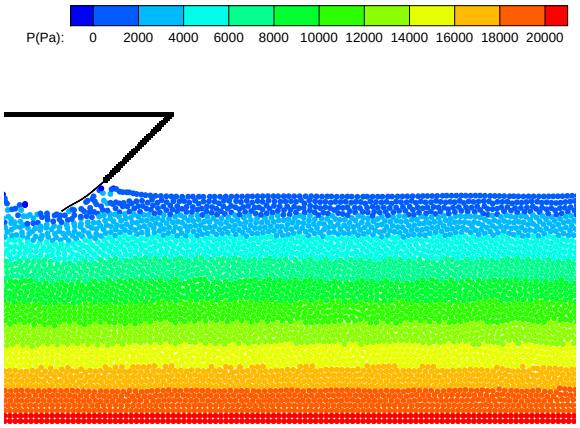

5.19.15 14s

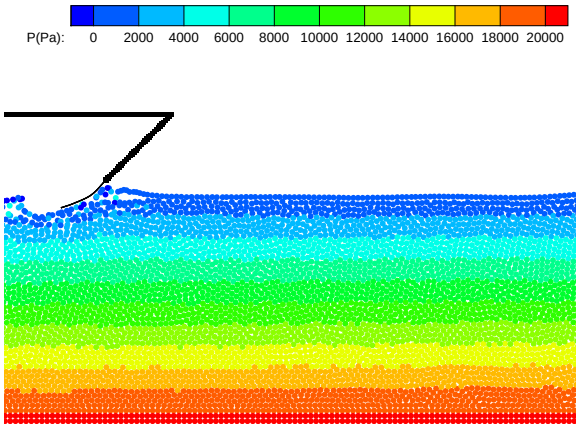

5.19.16 15s

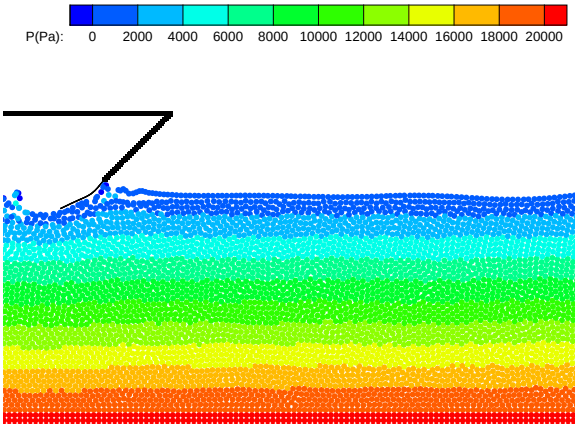

5.19.17 16s

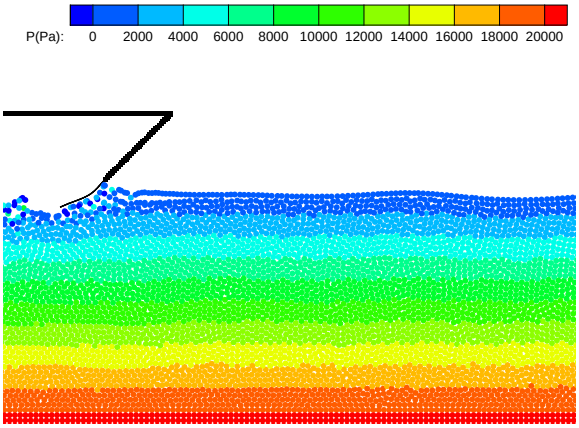

5.19.18 17s

Figure 5.19: Whole simulation with initial immersion depth = 7.5 inches, flow speed = 6 ft/s, cushion pressure = 2 inches-H_20 (Continued)

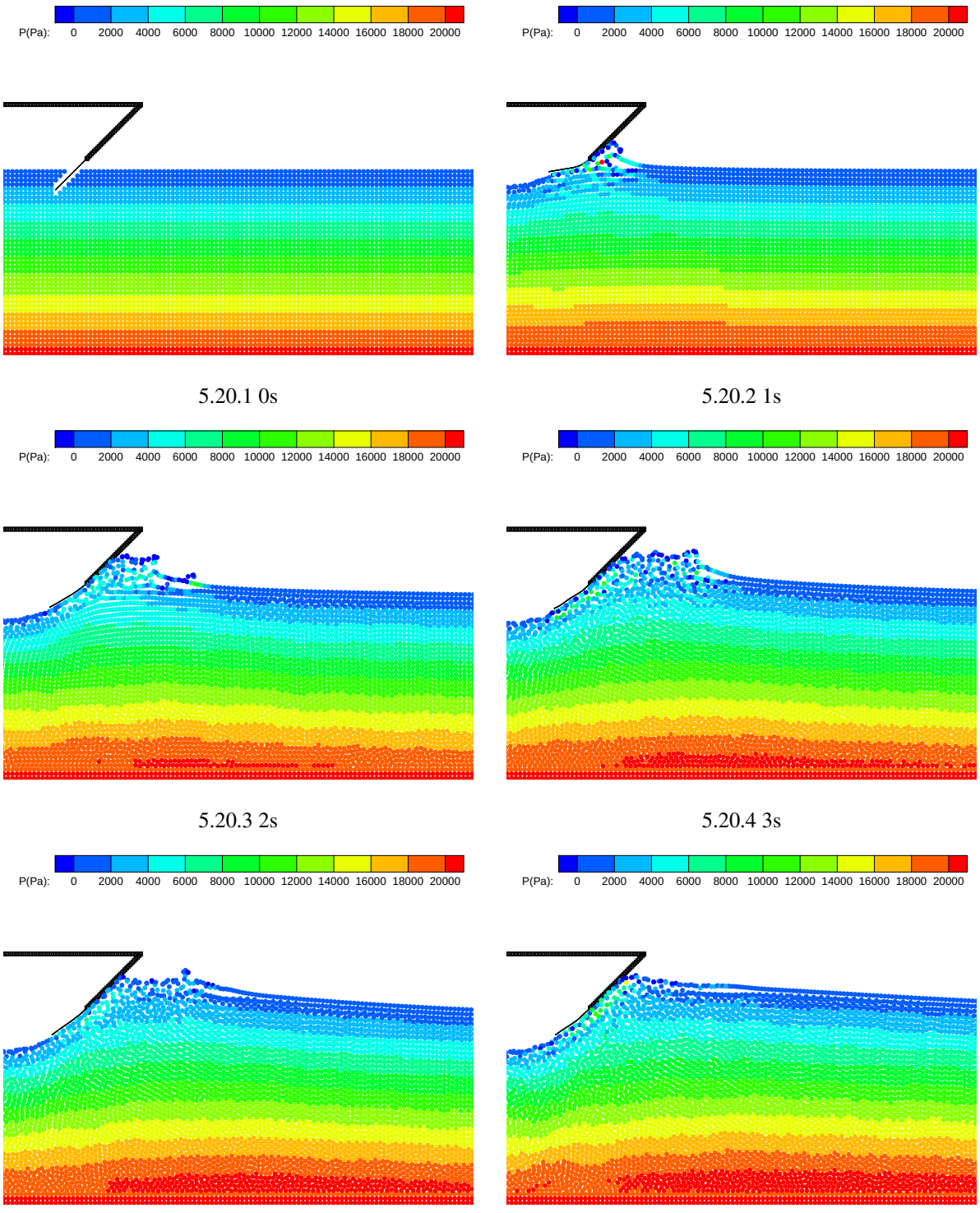

Figure 5.20: Whole simulation with initial immersion depth = 9 inches, flow speed = 10 ft/s, cushion pressure = 9 inches-H_20

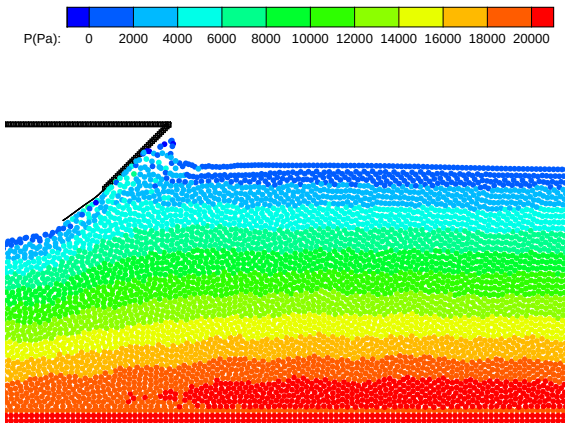

5.20.7 6s

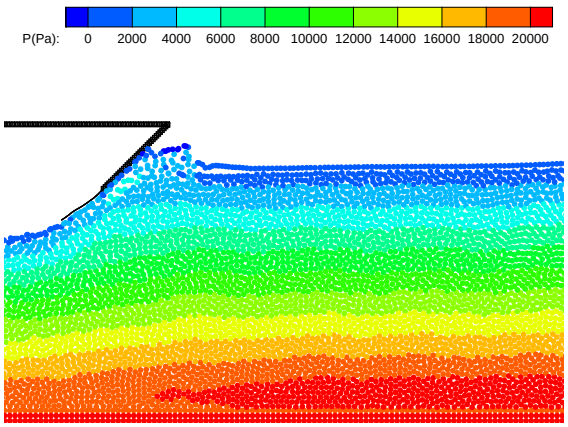

5.20.8 7s

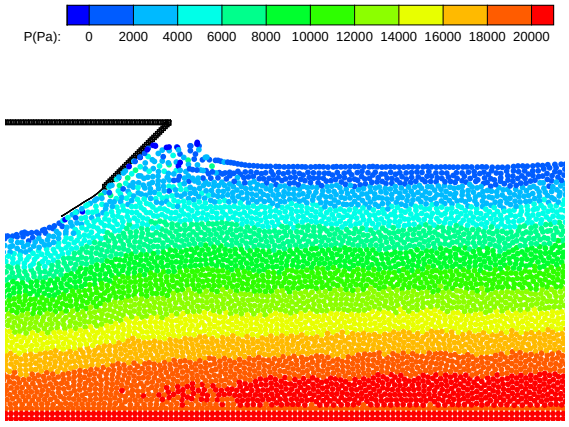

5.20.9 8s

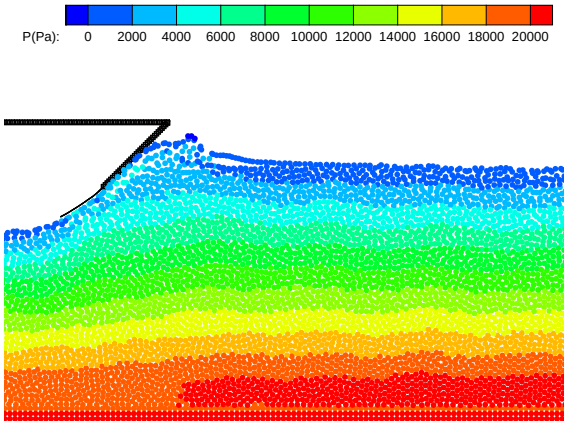

5.20.10 9s

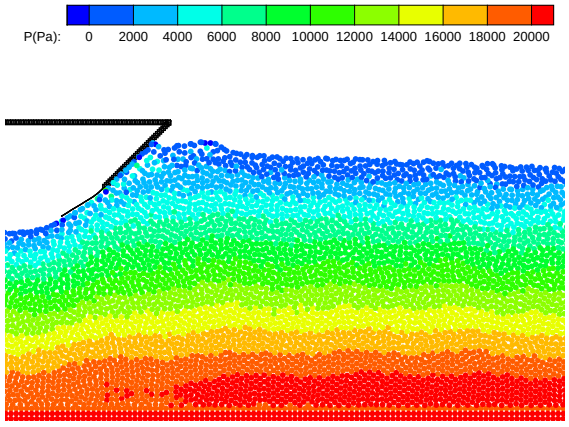

5.20.11 10s

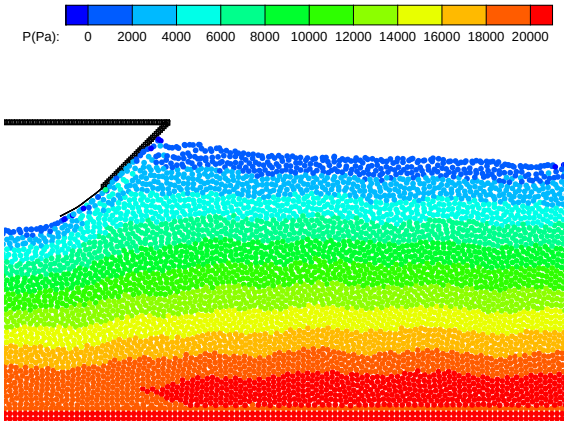

5.20.12 11s

Figure 5.20: Whole simulation with initial immersion depth = 9 inches, flow speed = 10 ft/s, cushion pressure = 9 inches-H_20 (Continued)

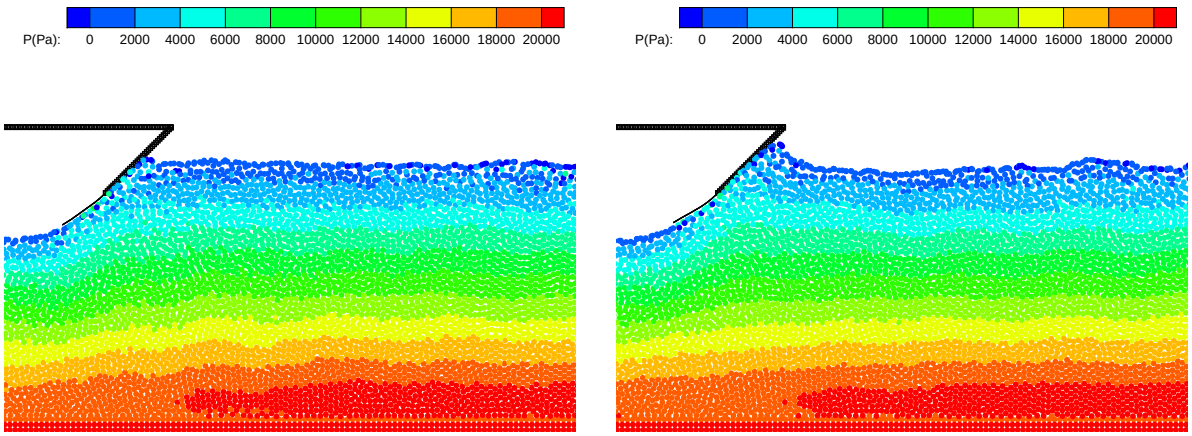

5.20.13 12s

5.20.14 13s

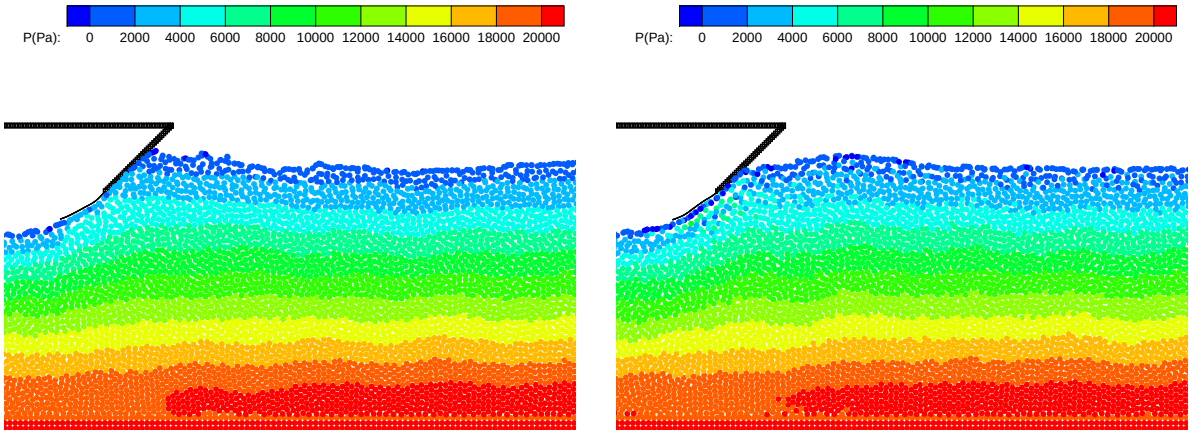

5.20.15 14s

5.20.16 15s

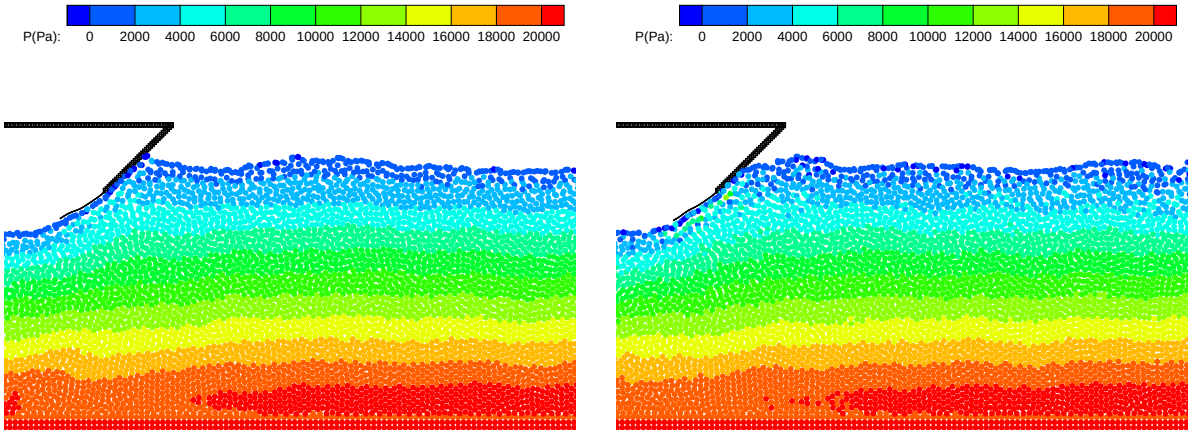

5.20.17 16s

5.20.18 17s

Figure 5.20: Whole simulation with initial immersion depth = 9 inches, flow speed = 10 ft/s, cushion pressure = 9 inches-H_20 (Continued)

The time history of the deflections of the bow seal at the three position are shown in Fig. 5.1.2

as well as bow wave height and water resistance (drag) upon the seal are recorded. As stated in Zalek and Doctors (2010), "For a given test run, the data is statistically averaged over the interval when the data indicates the system conditions are quasi-steady (that is, constant forward speed and constant cushion pressure.)" The mean values of the time history of the output data from the simulation are also calculated to be compared with experimental results. The coordinate system is established and illustrated in Figure 5.2. Under this coordinate system with a constant flow moving from right to left, the flexible seal will fold back and up (negative in X but positive in Z) in the absence of the air cushion. Increasing the cushion pressure tends to push the seal forward (positive in X) and downward (negative in Z). So the X displacement should increase and Z displacement should decrease with the rise of cushion pressure in the current numerical setup. The displacement history in Figures 5.3.1 and 5.3.2 show the correct trend for initial immersion depth = 7.5 inches and flow speed = 6 ft/s. After taking the average, Figures 5.4-5.9 show both displacements in X and Z directions along the three positions on the bow seal have a good agreement with the experimental data with the initial immersion depth = 7.5 inches except for two points in the case of flow speed of 8ft/s. Figure 5.10 shows the increase of the bow wave height with the increase of cushion pressure which is also observed in the experiment. The agreement of the water resistance on the flexible bow seal indicates good force transmission mechanism of the SPH-FEM model as already validated in the sloshing tank case in Chapter 1 and validation cases in Chapter 4. For the simulations with initial immersion depth = 9.0 inches, less agreement is observed for higher speed at 9 and 10 ft/s. Overall displacements, bow wave rise and water resistance in Figure 5.12 through 5.19 still show a reasonably agreement with the experimental data (Zalek and Doctors, 2010). In Fig. 5.19 and Fig. 5.20, a bow wave is clearly developed and the bow seal then reaches a quasi-steady state. Another case with hull moving 2 m to the right and the water width extending 2 m to the right is performed. Almost exact results are obtained which indicates the outflow has few effects on the results. A convergence study is performed to investigate the variation of results with respect to the number of particles and time step. Figure 5.21 shows the results of three configurations, as defined in Table 5.2 on Page 90 with the same time step. Figure 5.21 shows four time steps corresponding to four

CFL number (time steps at 1.32E-4, 6.62E-5, 3.31E-5 and 1.66E-5s.) with Configuration 1 . It is concluded from Figures 5.21 and 5.22 that the results are more sensitive to the spatial refinement than the width of the time step. In Figure 5.21, it is shown that spatial refinement can reduce the magnitude of the fluctuations about the mean value (eg. a smaller standard deviation). The results of configuration 1 are closer to Configuration 2 than Configuration 0. In Figure 5.22, there is no obvious variation with reducing time step size. The results for all CFL numbers other than 0.5 are very close to each other which indicates convergence.

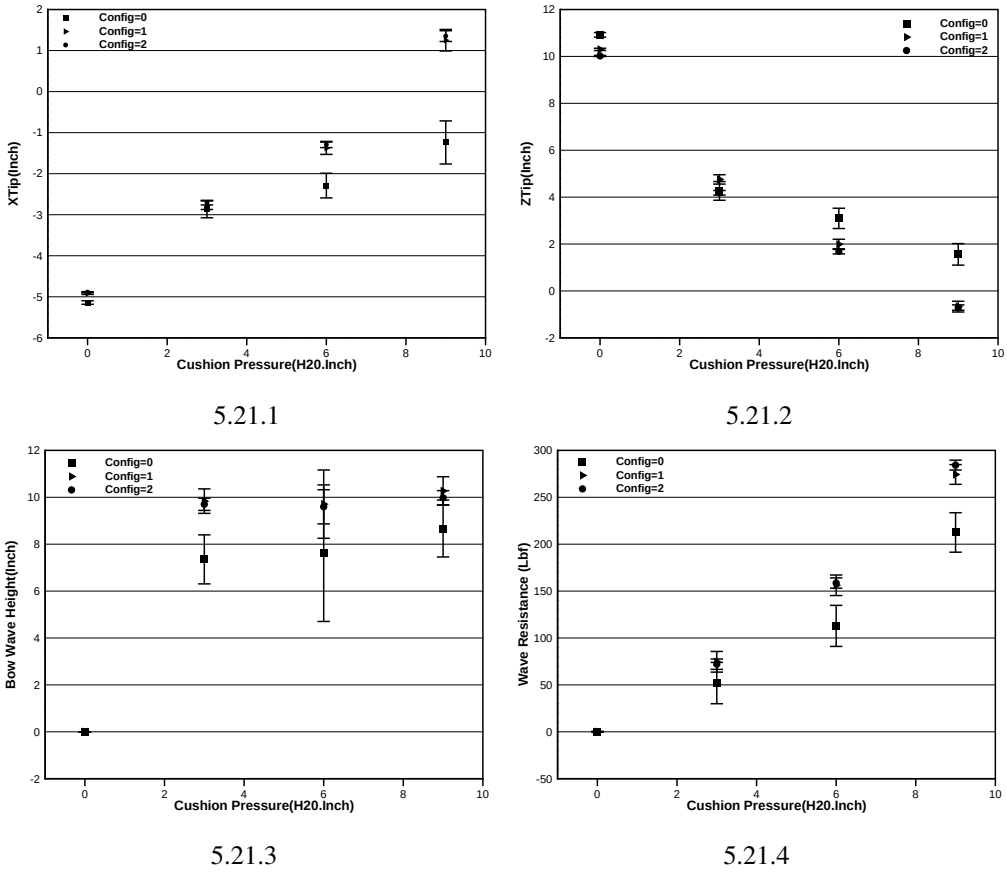

Figure 5.21: Comparison of three configurations for specified-pressure approaches.

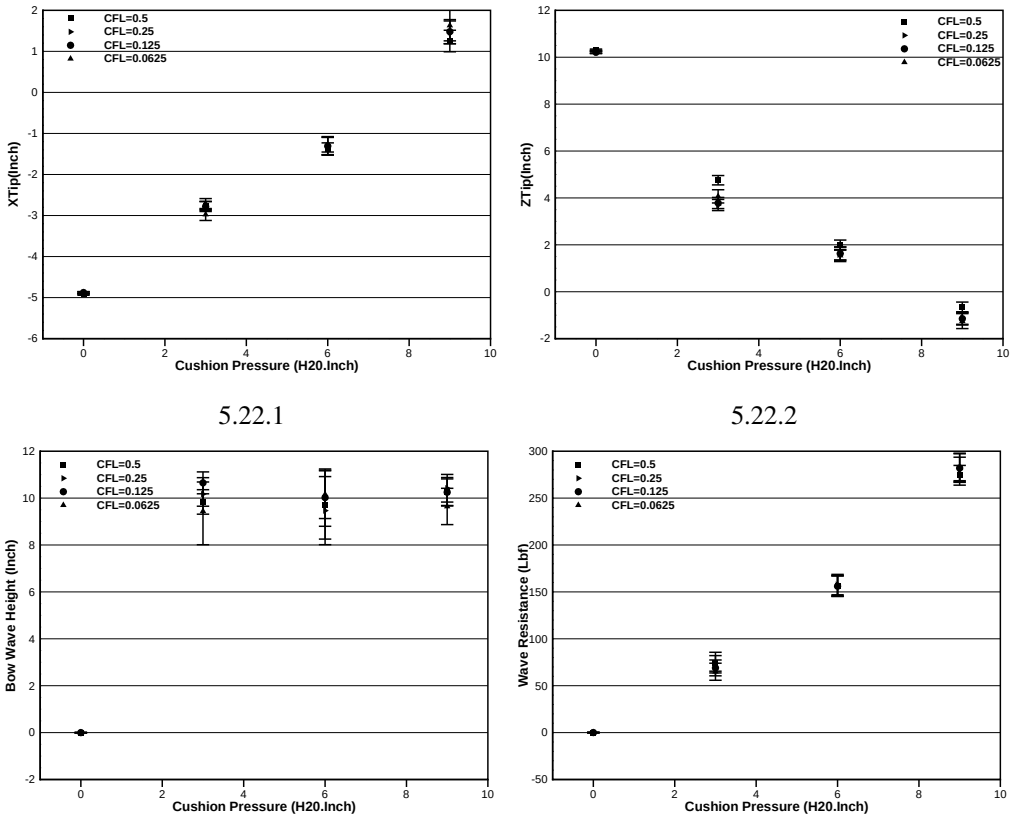

5.22.1 5.22.2

5.22.3 5.22.4

Figure 5.22: Comparison of four time steps for specified-pressure approaches.

5.1.3 Validation Results Using Air Particles Approach

The SPH-FEM model adopting a specified-pressure approach as described in Section 5.1.2 represents a simplified model of the cushion. As demonstrated in Chapter 2, the SPH formulation can also simulate multiphase air-water interaction with the air domain discretized by SPH particles. In this Section, the SPH-FEM model incorporates SPH air particles to simulate the air cushion. The initial configuration is shown in Fig. 5.23. As before, the water domain is simulated with SPH particles and the flexible seal is modeled with a FEM mesh. The differences lie in the chamber and the stern. Air particles are distributed inside the SES to simulate the air cushion. They are initialized with the cushion pressure instead of atmosphere pressure. A rigid stern seal is added

using Monaghan-type repulsive particles to keep the air particles inside the chamber. The stern of an SES is typically more complicated Faltinsen (2005) and in the experiment by Zalek and Doctors (2010) it consists of loops of lobes. But since the major object of interest in this analysis is the bow seal, for computational efficiency, the stern is simplified as an inclined rigid plane. The inclined plane allows us to reduce the length of the main deck to save computational time. No reflecting wave is observed in this configuration from the stern and the air particles inside the chamber are maintained. A full stern seal is left for future work. The simulations using the air-particles approach largely used the same parameters corresponding to Configuration 1 as in Table 5.2, with the additions listed in Table 5.3. For computational stability, due to the presence of the air particles, the time step must be reduced by a factor of 30; therefore, less cases have been computed. The cases simulated are with flow speeds 6-9 ft/s with increments of 1, cushion pressures of 0, 3, 6, 9 Inches-H_20 under initial immersion depth = 7.5 inches. Again, after recording the time histories of displacements, bow wave height and water resistance, mean values and standard deviations are obtained after a quasi-steady state is reached. Figures 5.24 through Fig. 5.31 show a full comparison between the numerical result from both the specified-pressure approach and the air particle approach of the SPH-FEM model and the experimental data. The results using the air particles approach are denoted with solid red symbols. To get a clear picture of the comparison, the results are plotted using the same layout as in Figure 5.3 through Figure 5.10 and replotted in Figures 5.24 through Fig. 5.31.

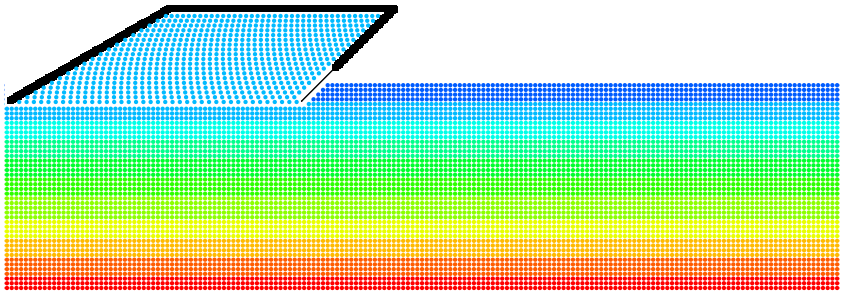

Figure 5.23: Initial configuration of SPH-FEM model simulating bow seal dynamics under high-speed flow using air-particle approach.

Table 5.3: Additional simulation parameters using air-particles approach. (Geometry is per Zalek and Doctors (2010).)

No. of Air Particles	723 (Config. 1)
dt	3.02E-6 s (Config. 1)
Simulation time	40 s
Total No. of time step	≈ 13.23 Million (Config. 1)
CPU Frequency	3.33 GHz
Computation time	≈ 8 days (Config. 1)

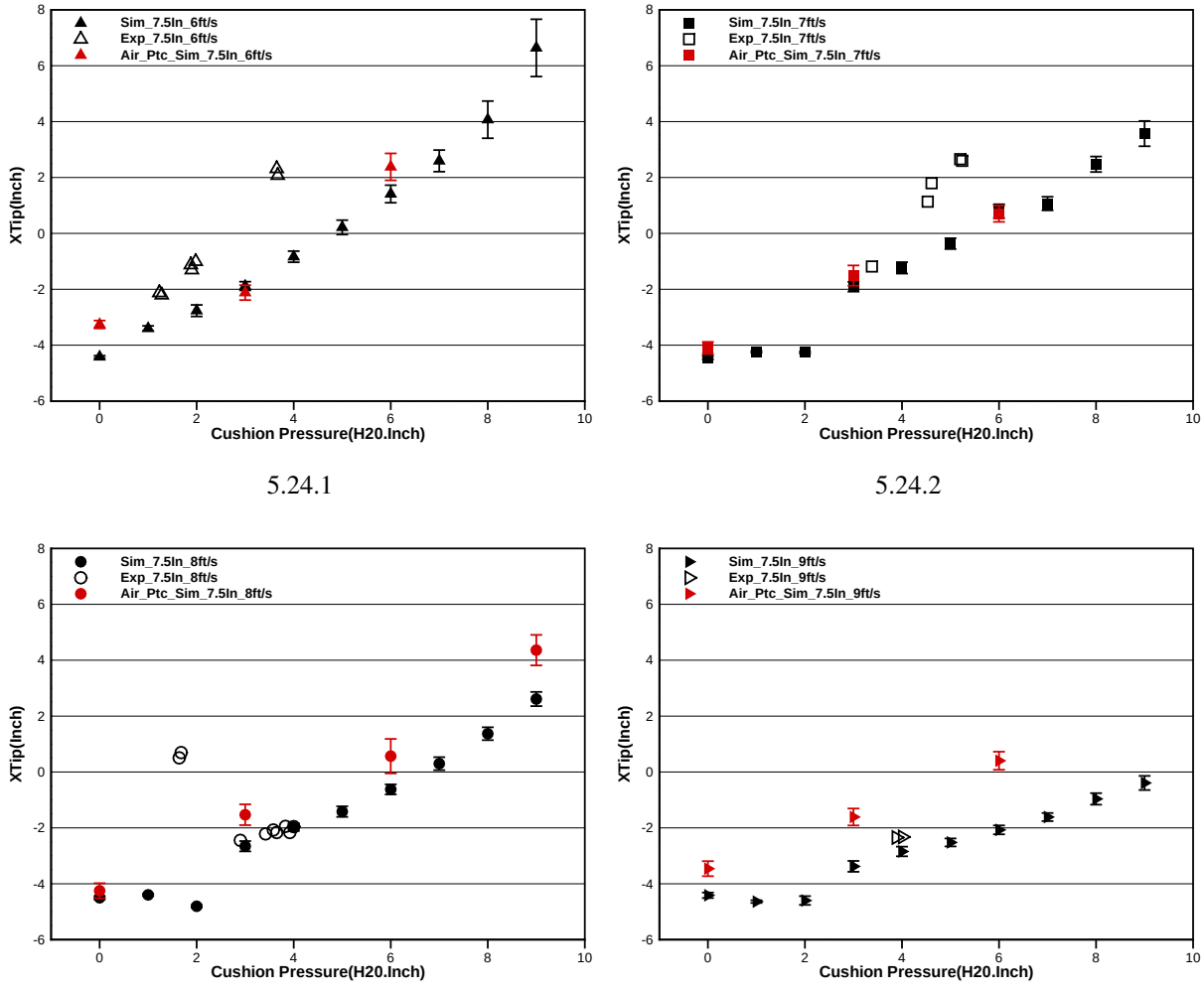

5.24.1 5.24.2

5.24.3 5.24.4

Figure 5.24: Comparison between SPH-FEM specified-pressure model, air-particles model and experiment for X displacement at the tip position of the bow seal for 7.5-inch depth.

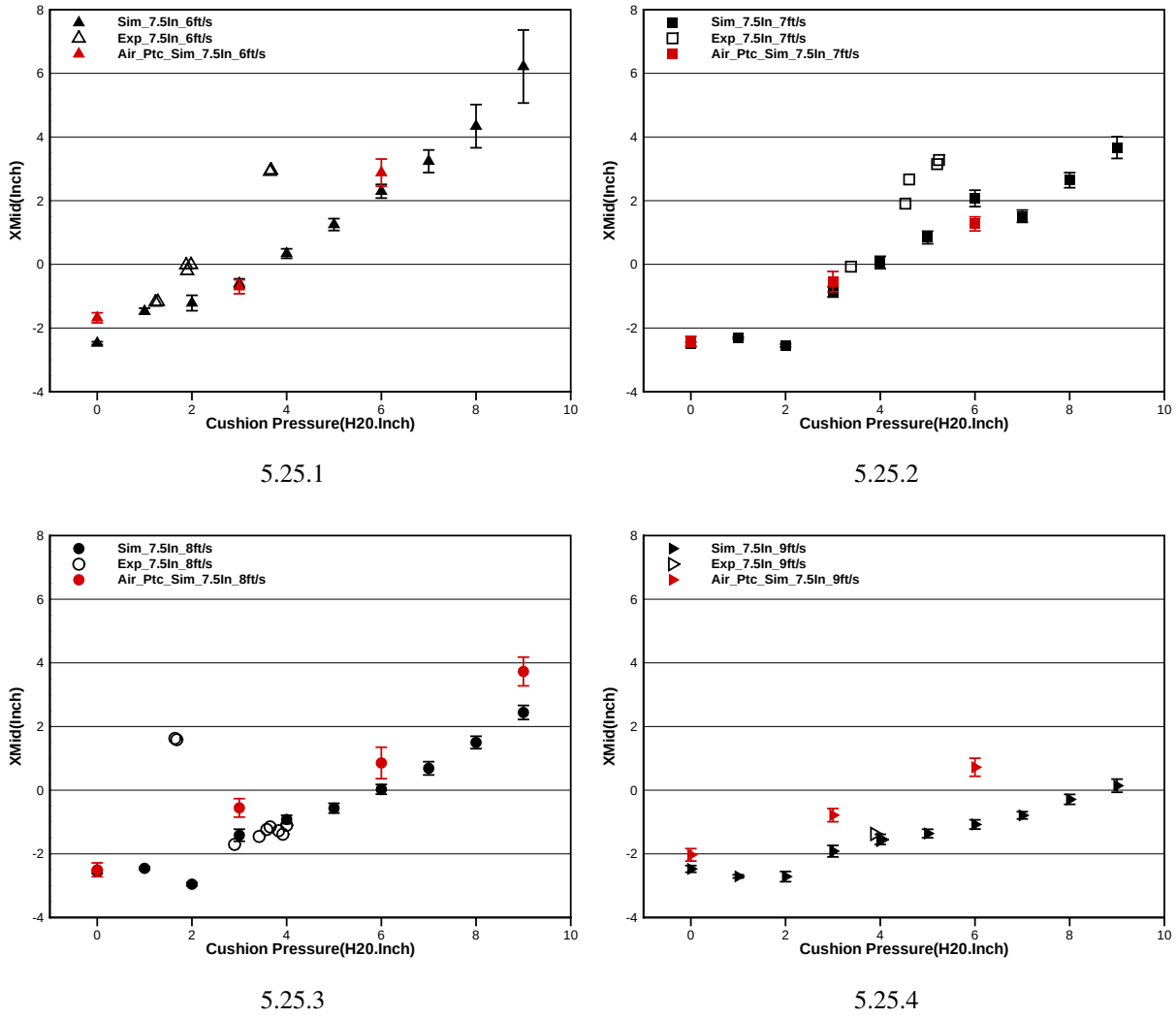

Figure 5.25: Comparison between SPH-FEM specified-pressure model, air-particles model and experiment for X displacement at the middle position of the bow seal for 7.5-inch depth.

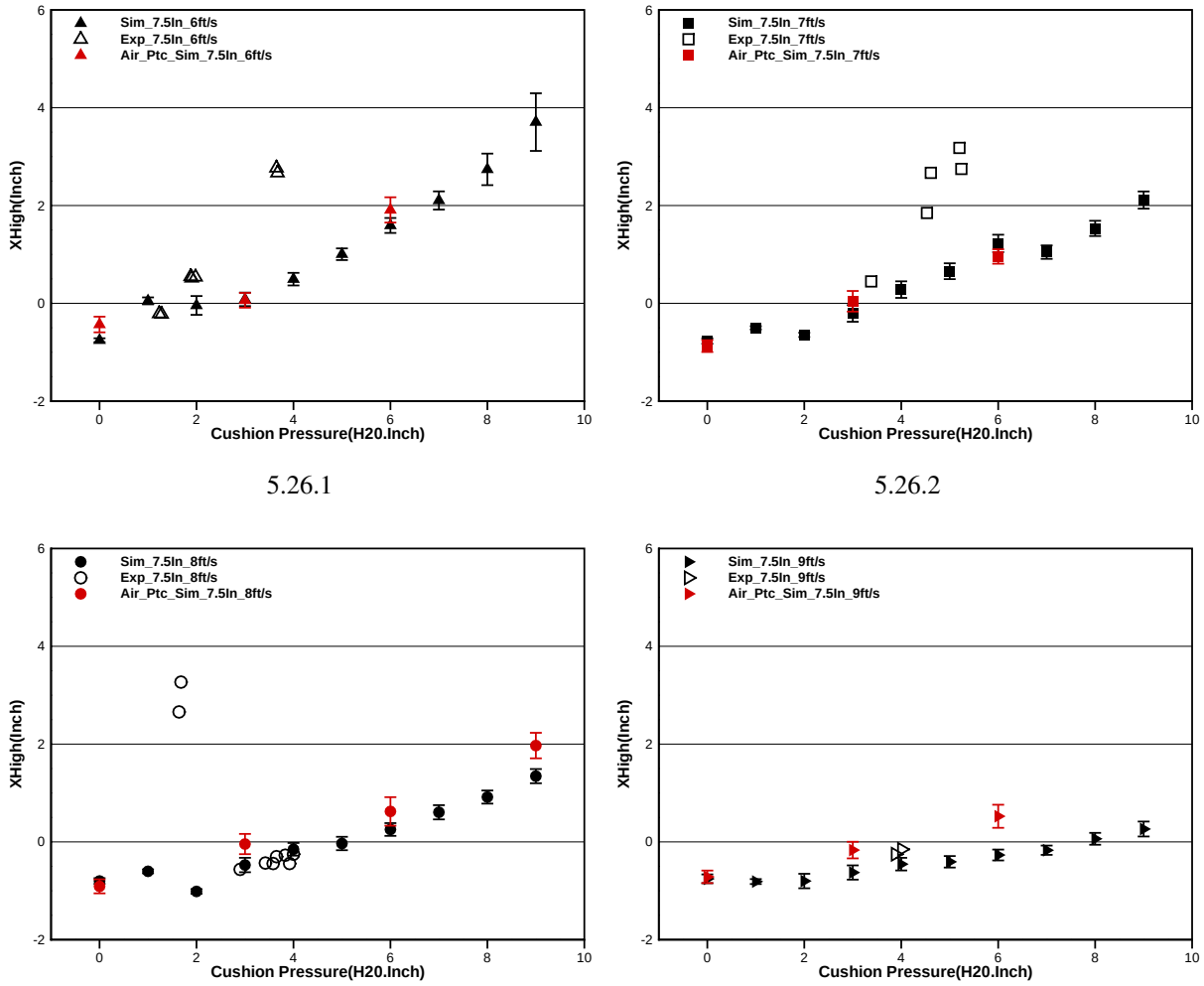

Figure 5.26: Comparison between SPH-FEM specified-pressure model, air-particles model and experiment for X displacement at the high position of the bow seal for 7.5-inch depth.

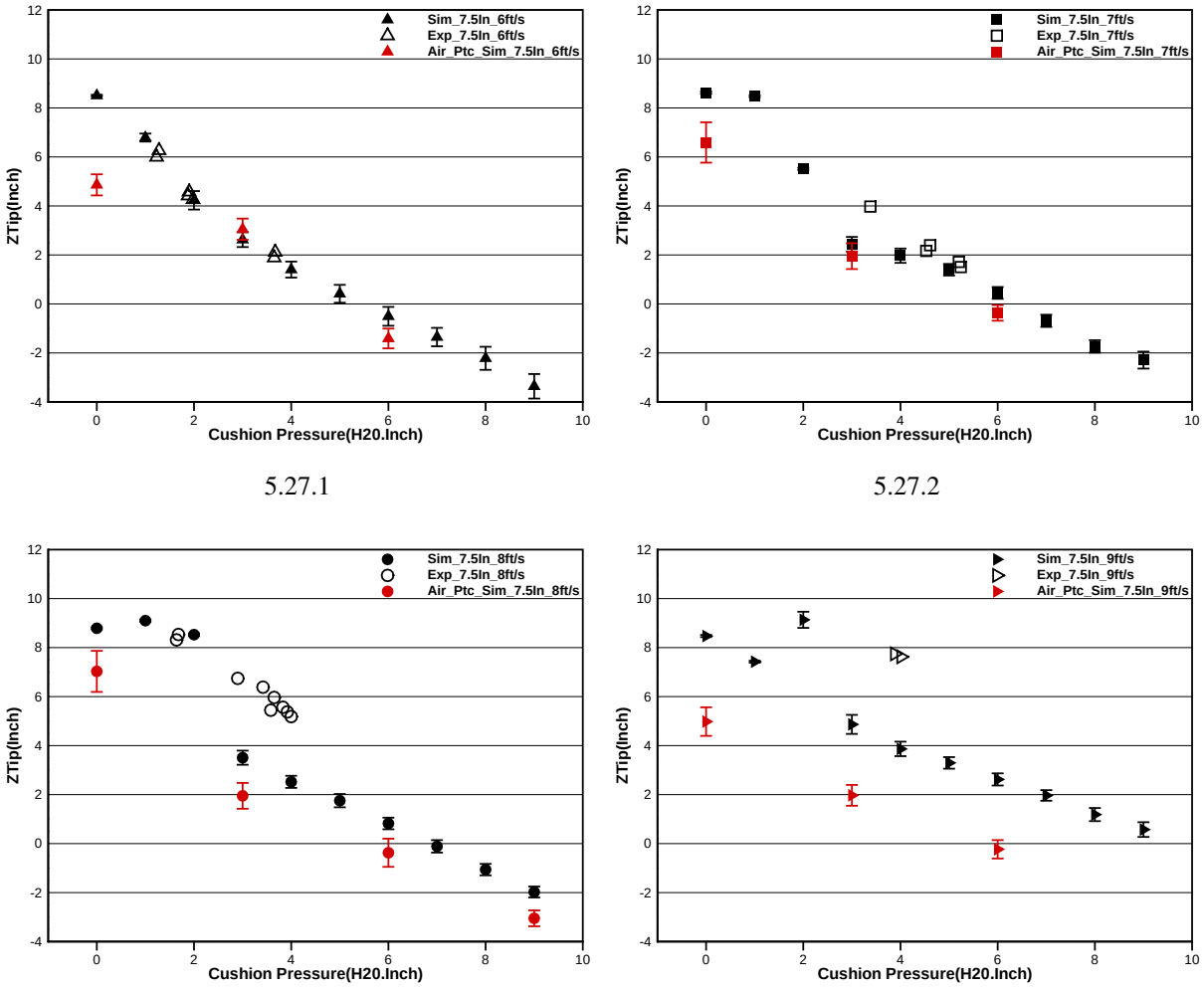

5.27.1 5.27.2

5.27.3 5.27.4

Figure 5.27: Comparison between SPH-FEM specified-pressure model, air-particles model and experiment for Z displacement at the tip position of the bow seal for 7.5-inch depth.

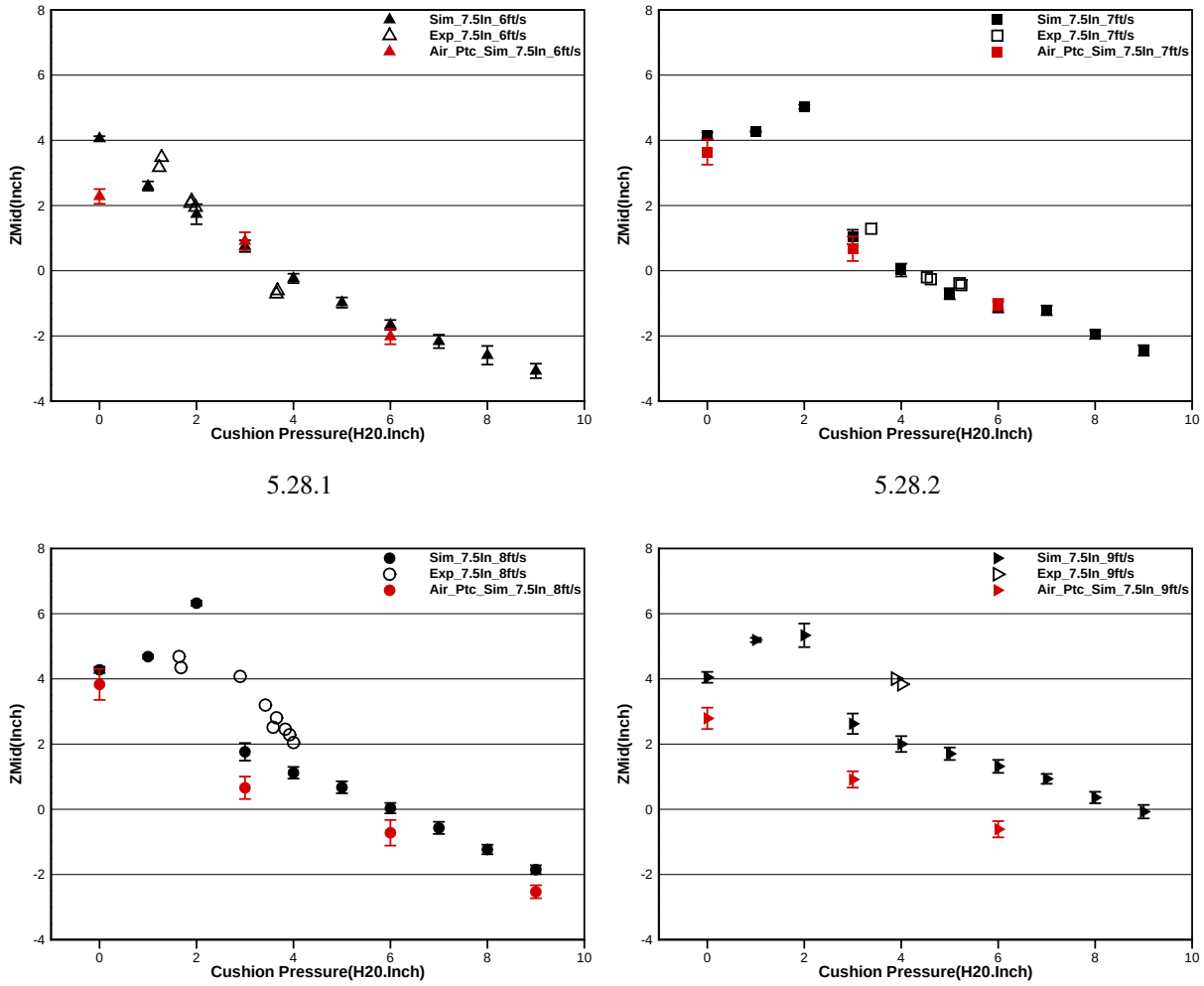

Figure 5.28: Comparison between SPH-FEM specified-pressure model, air-particles model and experiment for Z displacement at the middle position of the bow seal for 7.5-inch depth.

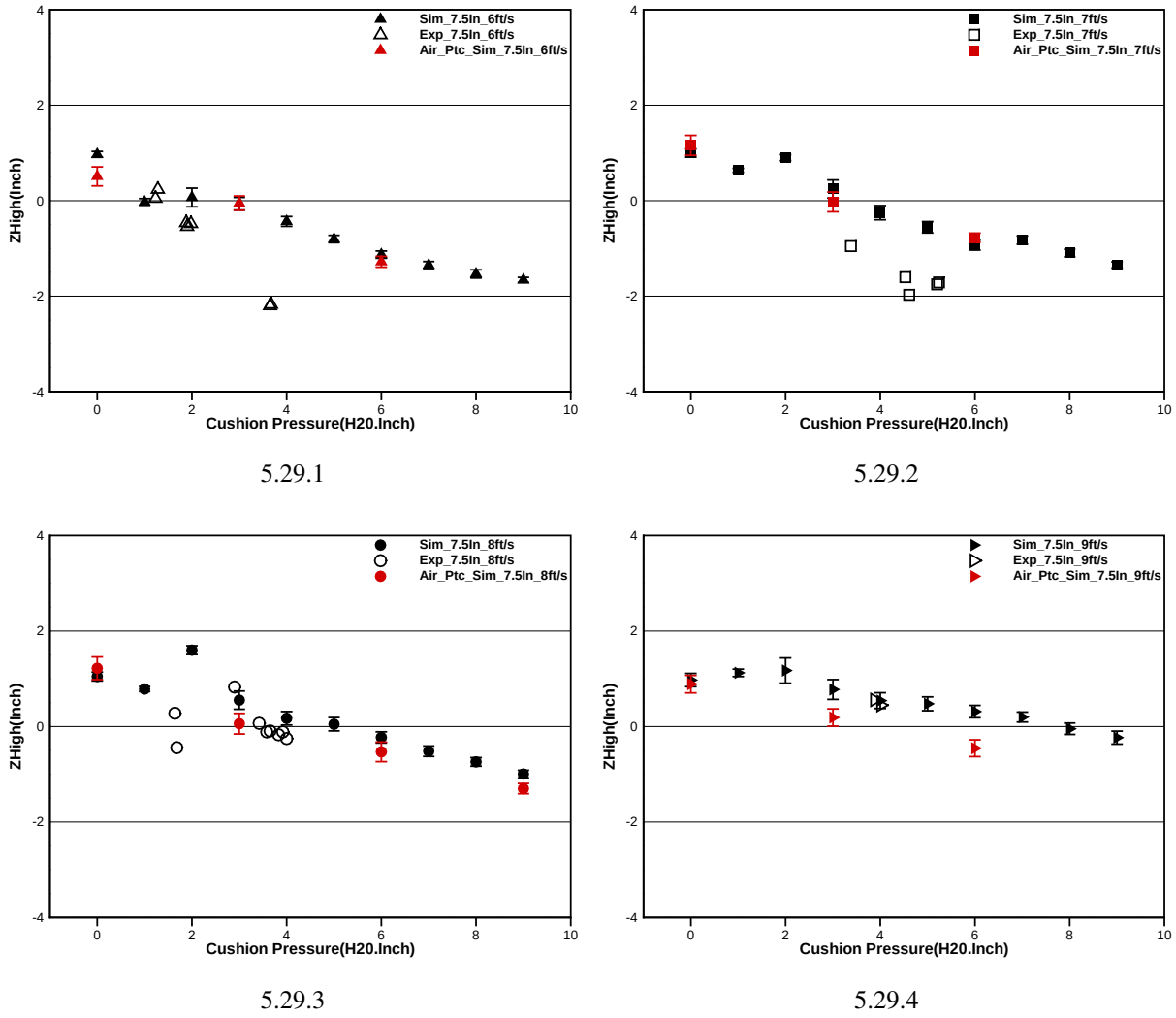

Figure 5.29: Comparison between SPH-FEM specified-pressure model, air-particles model and experiment for Z displacement at the high position of the bow seal for 7.5-inch depth.

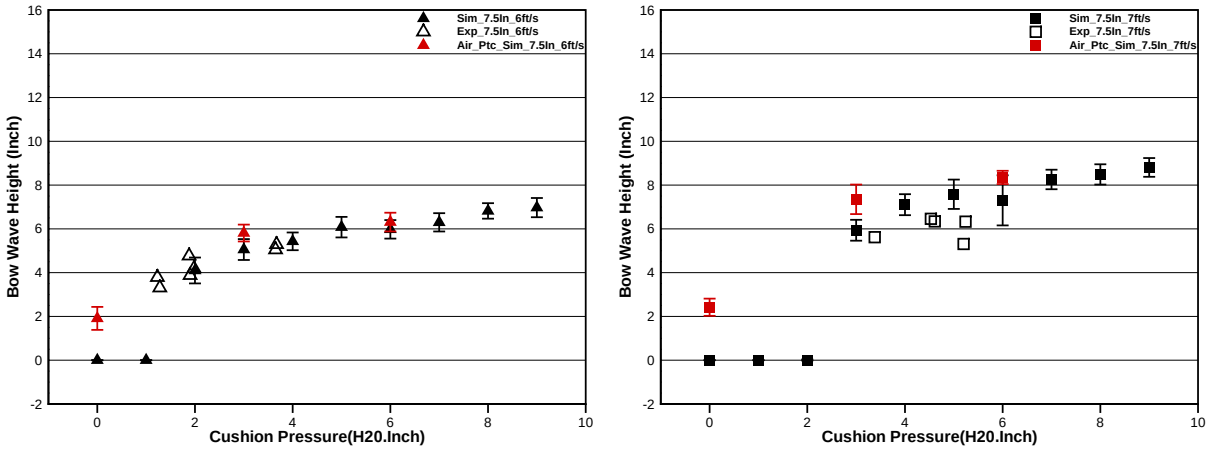

5.30.1

5.30.2

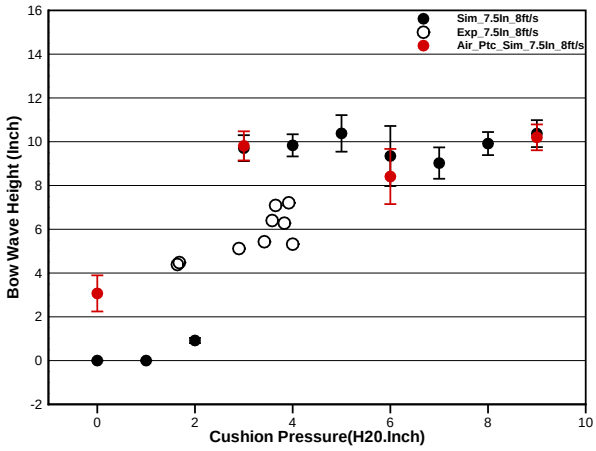

5.30.3

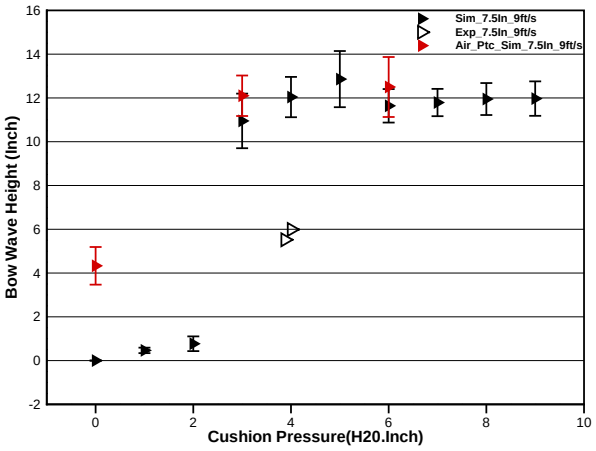

5.30.4

Figure 5.30: Comparison between SPH-FEM specified-pressure model, air-particles model and experiment for bow wave height for 7.5-inch depth.

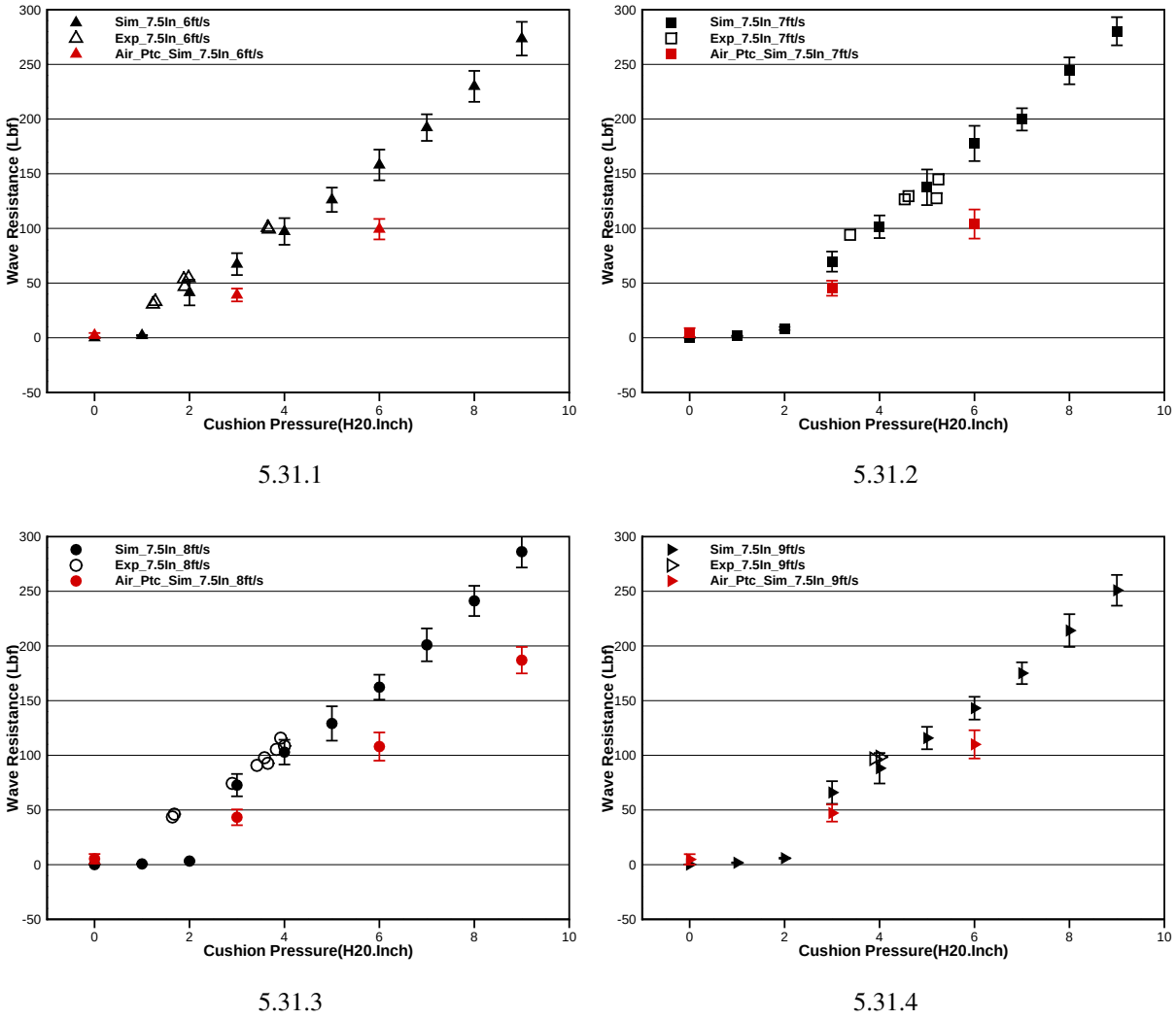

Figure 5.31: Comparison between SPH-FEM specified-pressure model, air-particles model and experiment for water resistance for 7.5-inch depth.

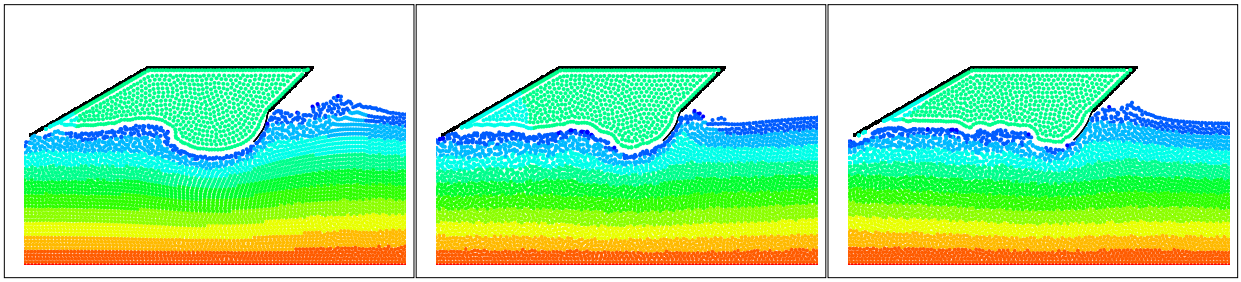

5.32.1 2s 5.32.2 4s 5.32.3 6s

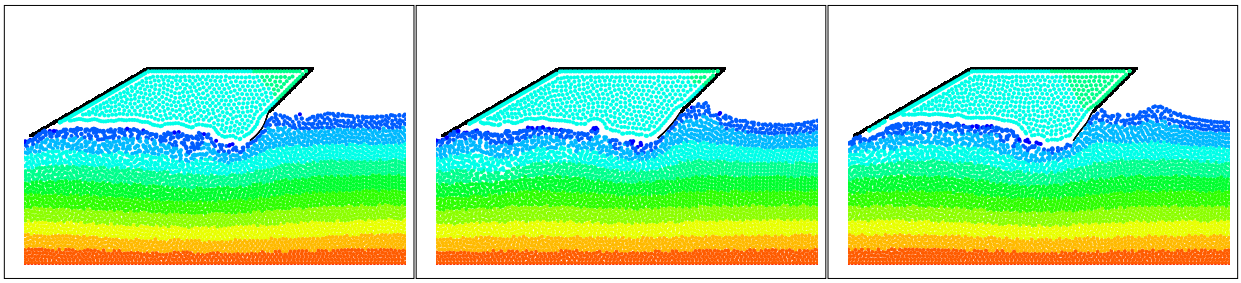

5.32.4 8s 5.32.5 10s 5.32.6 12s

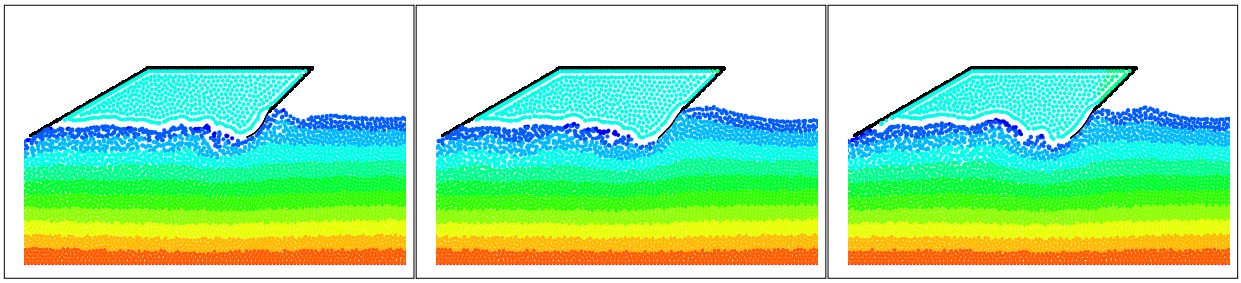

5.32.7 14s 5.32.8 16s 5.32.9 18s

Figure 5.32: Whole simulation using the air-particles approach with initial immersion depth = 7.5 inches, flow speed = 7 ft/s, cushion pressure = 0 inch-H_20

Despite the strict time step and stability condition posed after including the air particles, Figure 5.24 through 5.31 show acceptable agreement with specified-pressure model and experimental data. Better agreement is observed under lower speed for 6 and 7 ft/s. For 8 and 9 ft/s, the results with air particles approach diverted from experimental results and specified-pressure model. The simulated water resistance is under-predicted by the air particles approach. Figure 5.32 presents the snapshots of the simulation showing the successful coupling within air, water and structures.

By comparison, the advantage of using the specified-pressure approach is obvious: one can tol-

erate a larger time step while maintaining accuracy. However, since the specified-pressure model ignores the air-water interaction behind the bow seal, this model may be less accurate than the air particles model after incorporating the stern model. The air-water interaction will determine the wave shape below the chamber and thus the force acting on the stern. The wave shape also determines if air is leaking and as such impacts the end result. By evaluating the performance and the computational resources consumed between air particles and specified-pressure approaches, it may be concluded that the specified-pressure approach results in fast accurate results when solely the bow seal dynamics are of concern. The air particles approach is likely better suited for a full configuration of the ACV/SES including air fans and stern seals, etc. Indeed, immediate future work is to include these effects for a more thorough assessment. Stability issues at the air-water interface and the computational time are where substantial computational improvements can be made. Overall the validation results show great promise for SPH-FEM as a model for design tools to predict seal displacement, bow wave, and resistance for ACVs/SESs. Further study is warranted to incorporate more realistic geometry and three-dimensional effects.

Chapter 6

Conclusions

A CFD model solving fluid-structure interaction problems has been developed. The fluid domain is based on Smoothed Particle Hydrodynamics (SPH) and the structural domain employs large-deformation Finite Element Method (FEM). Chapter 2 presents the theory of SPH and successful assessment of SPH on the viscosity model, boundary force transmission mechanism and multi-phase flow simulation. Chapter 3 shows the finite-deformation FEM model used in this analysis to simulate structural dynamics under large non-linear deformation. The results compared with commercial software Abaqus show a good agreement under large structural deformation. In Chapter 4, two complicated elastic structures interacting with violent free-surface flows are investigated and simulation results show good agreement with the published experimental results. The validation results in Chapter 5 suggest that the SPH-FEM model can be readily applied to skirt/seal dynamics of ACV/SES interacting with free-surface flow. This CFD tool can be used to study the deflection and internal stress of a skirt/seal system given a set of free-stream flow and cushion/seal parameters.

The validation results lend credence to the use of this 2D SPH-FEM tool, and emphasis toward future development of a 3D tool, for ACV/SES skirt/seal dynamics. Because SPH-FEM is a loosely-coupled model, the components of the model act independently and can therefore be developed

separately. Also this could allow independent SPH and FEM solvers to couple through simple data transmission. By applying both SPH and FEM models, the advantages of using FEM for structural dynamics as well as the inherent strength of SPH when simulating fluids are obtained.

Further study is warranted into:

- An optimized structural solver to get a balanced computational time between fluid and structure.
- Incorporation of surface tension and turbulence models in SPH formulations.
- Alternative boundary conditions such as ghost particles to alleviate the boundary deficiency problems. Possible utilization of OPENFoam's optimized data structure to obtain an efficient ghost-particle mirroring procedure.
- A complete configuration for the ACV/SES. This will include the simulation of the stern part of the ACV/SES and the air fan model. And the ACV/SES made free to heave/pitch.
- 3D SPH-FEM model should be investigated and developed so that 3D effects can be included.

Bibliography

Antoci, C. (2006). *Simulazione numerica dell' interazione fluido-struttura con la tecnica SPH*. PhD thesis, Università di Pavia.

Antoci, C., Gallati, M., and Sibilla, S. (2007). Numerical simulation of fluid-structure interaction by SPH. *Computers and Structures*, pages 879–890.

Attaway, S., M.W., H., and Swegle, J. (1994). Coupling of Smooth Particle Hydrodynamics with the Finite Element Method. *Nuclear Engineering and Design*, 150(2-3):199–205.

Batchelor, G. K. (1967). *An introduction to fluid dynamics*. Cambridge University Press, Cambridge.

Bathe, K.-J. (1996). *Finite Element Procedures*. Prentice Hall Inc.

Bathe, K.-J., Ramm, E., and Wilson, E. L. (1975). Finite element formulations for large deformation dynamic analysis. *International Journal for Numerical Methods in Engineering*, 9(2):353–386.

Belytschko, T., Krongauz, Y., Dolbow, J., and Gerlach, C. (1998). On the completeness of meshfree particle methods. *International Journal for Numerical Methods in Engineering*, 43(5):785–819.

Botia-Vera, E., Souto Iglesias, A., Bulian, G., and Lobovsky, L. (2010). Three SPH novel benchmark test cases for free surface flows. In *SPHEERIC 5th International Workshop*.

Cleary, P. W. (1998). Modeling confined multi-material heat and mass flows using SPH. *Applied Mathematical Modelling*, 2:981–993.

Colagrossi, A. and Landrini, M. (2003). Numerical simulation of interfacial flows by Smoothed Particle Hydrodynamics. *Journal of Computational Physics*, 191:448–475.

Cole, R. H. (1948). *Underwater Explosions*. Princeton University Press.

Cook, R. D. (1974). *Concepts and Applications of Finite Element Analysis*. John Wiley & Sons.

Cummins, S. J. and Rudman, M. (1999). An SPH projection method. *Journal of Computational Physics*, 152:584–607.

Delorme, L., Colagrossi, A., Souto-Iglesias, A., Zamora Rodriguez, R., and Botia-Vera, E. (2009). A set of canonical problems in sloshing, Part I: Pressure field in forced roll–comparison between experimental results and SPH. *Ocean Engineering*, 36:168–178.

Dilts, G. A. (1999). Moving-Least-Squares-particle hydrodynamics - I. Consistency and stability. *International Journal for Numerical Methods in Engineering*, 44(8):1115–1155.

Doctors, L. J. (1975). Nonlinear motion of an air-cushion vehicle over waves. *Journal of Hydronautics*, 9(2):44–57.

Donea, J., Huerta, A., Ponthot, J.-P., and Rodríguez-Ferran, A. (2004). Arbitrary Lagrangian-Eulerian methods. In *Encyclopedia of Computational Mechanics*. John Wiley & Sons, Ltd.

Faltinsen, O. (2005). *Hydrodynamics of high-speed marine vehicles*. Cambridge University Press.

Fourey, G., Oger, G., Touzé, D. L., and Alessandrini, B. (2010). Violent fluid-structure interaction simulations using a coupled SPH/FEM method. In *WCCM/APCOM 2010*.

Fourey, G., Touzé, D. L., and Alessandrini, B. (2011). Development of a sph-fem coupling methodology for modeling strong fluid-structure interactions. In *International Conference on Particle-based Methods: Fundamentals and Applications*, Barcelona, Spain.

Gingold, R. A. and Monaghan, J. J. (1977). Smoothed Particle Hydrodynamics: Theory and application to non-spherical stars. *Monthly Notices of the Royal Astronomical Society*, 181:375–389.

Gómez-Gesteira, M., Rogers, B., Dalrymple, R., Crespo, A., and Narayanaswamy, M. (2010). User guide for the SPHysics code v2.0.

Gray, J. P., Monaghan, J. J., and Swift, R. P. (2001). SPH elastic dynamics. *Comput. Methods Appl. Mech. Engrg.*, 190:6641–6662.

Groenenboom, P. H. L. and Cartwright, B. K. (2010). Hydrodynamics and fluid-structure interaction by coupled SPH-FE method. *Journal of Hydraulic Research*, 48:61–73.

Hirt, C. W., Amsden, A. A., and Cook, J. L. (1997). An Arbitrary Lagrangian-Eulerian computing method for all flow speeds. *J. Comput. Phys.*, 135(2):203–216.

Hughes, T. J. R., Liu, W. K., and Zimmermann, T. K. (1981). Lagrangian-Eulerian Finite Element formulation for incompressible viscous flows. *Computer Methods in Applied Mechanics and Engineering*, 29(3):329–349.

Le Touz, D., Oger, G., and Alessandrini, B. (2008). Smoothed Particle Hydrodynamics simulation of fast ship flows. In *27th Symposium on Naval Hydrodynamics*, Seoul, Korea.

Lee, E.-S. (2007). *Truly incompressible approach for computing incompressible flow in SPH and comparisons with the traditional weakly compressible approach*. PhD thesis, The University of Manchester.

Lee, E.-S., Moulinec, C., Xu, R., Violeau, D., Laurence, D., and Stansby, P. (2008). Comparisons of weakly compressible and truly incompressible algorithms for the SPH mesh free particle method. *Journal of Computational Physics*, pages 8417–8436.

Libersky, L. D., Petschek, A. G., Carney, T. C., Hipp, J. R., and Allahdadi, F. A. (1993). High strain Lagrangian hydrodynamics. *J. Comput. Phys.*, pages 67–75.

Liu, G. and Liu, M. (2003). *Smoothed Particle Hydrodynamics: a meshfree particle method*. World Scientific Publishing Co.

Liu, M. and Liu, G. (2010). Smoothed Particle Hydrodynamics (SPH): an overview and recent developments. *Arch Comput Methods Eng*, 17:25–76.

Lucy, L. B. (1977). A numerical approach to the testing of the fission hypothesis. *Astronomical Journal*, 82:1013–1024.

Mantle, P. J. (1975). *A technical summary of air cushion craft development*. Bethesda, Md: U.S. Dept. of Defense, Dept. of the Navy, David W. Taylor Naval Ship Research and Development Center, Systems Development Dept.

Milewski, B., Connell, B., Wilson, J., and Kring, D. (2007). Dynamics of air cushion vehicles operating in a seaway. *9th International Conference on Numerical Ship Hydrodynamics*.

Milewski, W., Connell, B., Peterson, B., and Kring, D. (2008). Initial validation of the acvsim model for dynamics of air cushion vehicles. In *27th Symposium on Naval Hydrodynamics*.

Monaghan, J. J. (1992). Smoothed particle hydrodynamics. *Annual review of astronomy and astrophysics*, 30:543–574.

Monaghan, J. J. (1994). Simulating free surface flows with SPH. *J. Comput. Phys.*, 110:399–406.

Monaghan, J. J. (2005). Smoothed Particle Hydrodynamics. *Reports on Progress in Physics*, 68:1703–1759.

Monaghan, J. J. and Kajtar, J. B. (2009). SPH particle boundary forces for arbitrary boundaries. *Computer Physics Communications*, 180:1811–1820.

Monaghan, J. J. and Kos, A. (1999). Solitary waves on a cretan beach. *Journal of Waterway, Port, Coastal, and Ocean Engineering*, 145:145–154.

Morris, J. P., Fox, P. J., and Zhu, Y. (1997). Modeling low reynolds number incompressible flows using SPH. *Journal of Computational Physics*, 136:214–226.

Newmark, N. (1959). A method of computation for structural dynamics. *Journal of Engineering Mechnamics Division, ASCE*, 85:67–94.

Oberkampf, W. L. and Roy, C. J. (2010). *Verification and Validation in Scientific Computing*. Cambridge University Press.

Oden, J. T. (1972). Finite elements of nonlinear continua. *Advanced Engineering Series McGrawHill*.

Oger, G., Doring, M., Alessandrini, B., and Ferrant, P. (2006). Two-dimensional SPH simulations of wedge water entries. *Journal of Computational Physics*, 213:803–822.

Peskin, C. S. (1977). Numerical analysis of blood flow in the heart. *Journal of Computational Physics*, 25(3):220 – 252.

Rogers, B. D. and Dalrymple, R. A. (2008). SPH modeling of tsunami waves. In Liu, P. L.-F., Yeh, H., and Synolakis, C., editors, *Advanced Numerical Models for Simulating Tsunami Waves and Runup*, pages 75–100. World Scientific Press.

Sirovich, L. (1968). Initial and boundary value problems in dissipative gas dynamics. *Phys. Fluids*, 11:1424–1439.

Souto-Iglesias, A., Delorme, L., Perez-Rojas, L., and Abril-Perez, S. (2006). Liquid moment amplitude assessment in sloshing type problems with Smooth Particle Hydrodynamics. *Ocean Engineering*, pages 1462–1484.

Souto-Iglesias, A., Idelsohn, S., Marti, J., Zamora-Rodriguez, R., and Onate, E. (2008). Modeling of free surface flows with elastic bodies interactions. In *27th Symposium on Naval Hydrodynamics*, Korea.

Sullivan, P. A., Charest, P. A., and Ma, T. (1994). Heave stiffness of an air cushion vehicle bag and finger skirt. *Journal of Ship Research*, 38(4):302–307.

Sussman, T. and Bathe, K.-J. (1987). A finite element formulation for nonlinear incompressible elastic and inelastic analysis. *Computers and Structures*, 26:357–409.

Thiagarajan, K. P. and Morris-Thomas, M. T. (2006). Wave-induced motions of an air cushion structure in shallow water. *Ocean Engineering*, 33(8-9):1143 – 1160.

Timoshenko, S. and Goodier, J. (1970). *Theory of Elasticity*. McGraw Hill Higher Education.

Turner, M. J., Clough, R. W., Martin, H. C., and Topp, L. P. (1956). Stiffness and deflection analysis of complex structures. *J. Aeronautical Society*, 23.

Vuyst, T. D., Vignjevic, R., and Campbell, J. C. (2005). Coupling between meshless and Finite Element Methods. *International Journal of Impact Engineering*, 31(8):1054–1064.

Wendland, H. (1995). Piecewise polynomial, positive definite and compactly supported radial functions of minimal degree. *Advances in Computational Mathematics*, 4:389–396.

Yang, Q., Jones, V., and McCue, L. (2010). Numerical study on fluid-structure interaction using Smoothed Particle Hydrodynamics and Finite Element Methods. In *SPHERIC 5th International Workshop*, Manchester,UK.

Yang, Q., Jones, V., and McCue, L. (2011a). Free-surface flow interactions with deformable structures using a SPH-FEM model. (Accepted with minor revision by Ocean Engineering).

Yang, Q., Jones, V., and McCue, L. (2011b). Investigation of skirt dynamics of air cushion vehicles under non-linear wave impact using a SPH-FEM model. In *11th International Conference on Fast Sea Transportation*, Hawaii.

Yun, L. and Bliault, A. (2000). *Theory and Design of Air Cushion Craft*. Butterworth-Heinemann.

Zalek, S. Z. and Doctors, L. J. (2010). Experimental study of the resistance of surface-effect-ship seals. In *Twenty-Eighth Symposium on Naval Hydrodynamics*, Pasadena, California.

Zienkiewics, O. C. and Taylor, R. L. (2005). *The Finite Element Method for Solid and Structural Mechanmics*. Elsevier Butterworth-Heinemann, sixth edition.

Zienkiewics, O. C., Taylor, R. L., and Zhu, J. Z. (2005). *The Finite Element Method: Its Basis and Fundamentals*. Elsevier Butterworth-Heinemann, sixth edition.